

MASS TRANSFER IN POROUS
TISSUE ENGINEERING
SCAFFOLDS

By

BENJAMIN J. LAWRENCE

Bachelor of Science in Chemical Engineering
Oklahoma State University
Stillwater, OK
2004

Master of Science in Chemical Engineering
Oklahoma State University
Stillwater, OK
2006

Submitted to the Faculty of the
Graduate College of the
Oklahoma State University
in partial fulfillment of
the requirements for
the Degree of
DOCTOR OF PHILOSOPHY
July, 2008

MASS TRANSFER IN POROUS
TISSUE ENGINEERING
SCAFFOLDS

Dissertation Approved:

Dr. Sundar Madihally

Dissertation Adviser

Dr. A.J. Johannes

Dr. Gary Foutch

Dr Warren Ford

Dr. H-K Lin

Dr. A. Gordon Emslie

Dean of the Graduate College

ACKNOWLEDGEMENTS

No one gets through a PhD program without a lot of help. So I would like to take this opportunity to thank everyone who helped make this possible. First, I want to thank my advisor Dr. Sundar Madhally who proves time and time again that you don't need a "top ten" school to provide a world class education, and I want to thank my committee members, Dr. A.J., Dr. Foutch, Dr. Ford, and Dr. H-K Lin for their support, guidance, and use of equipment. During my tenure at OSU I've had the opportunity to work with an amazing set of graduate students. Special thanks go to Fadee Mondalek, from the OU Health Sciences Center, for his help and collaboration with the particle and permeability work, to Mamatha Devarapalli for help with the reactor and simulation work, Rangarani Karnati from the OSU Chemistry Department for help with the GPC, Aparna Sarasam for showing me the ropes around the lab, and everyone else in the group over the years. I also need to thank both the Oklahoma Center for Advancement of Science and Technology (HR05-075), and National Institutes of Health (1R21DK074858-01A2) for providing research funding, as well as The OSU Graduate College and the Nancy Randolph Davis Fellowship for helping finance my graduate education. I want to thank my friends and family for keeping me smiling throughout the PhD experience, and I need to thank my wife, Mrs. Barbara Lawrence, for her love, affection, and ability to integrate complicated mathematical equations in 20 minutes or less.

TABLE OF CONTENTS

Chapter	Page
ACKNOWLEDGEMENTS.....	iii
TABLE OF CONTENTS.....	iv
LIST OF TABLES.....	vii
LIST OF FIGURES	viii
1. Introduction.....	1
Specific Aim 1: Understand the use of nanoparticles for local delivery of growth factors within porous structures.	5
Specific Aim 2: Modeling fluid flow through porous scaffolds	6
Specific Aim 3: Modeling transport and consumption of oxygen through cell seeded scaffolds.	7
2.1 Tissue Engineering Basics	8
2.2 State of the Art: Natural Matrices	10
2.3. Formation of Three Dimensional Polymer Scaffolds	12
2.4 2D vs. 3D Cell Culture.....	14
2.5 Importance of 3D Spatial Architecture	16
2.5.1 Porosity	17
2.5.2 Pore Size.	19
2.5.3 Fiber Thickness.	21
2.5.4 Topography.....	22
2.6. Cellular Interaction	23
2.6.1. Changes in Cell-Adhesion.	23
2.6.2. Mechanotransduction.	25
2.7. Matrix Turnover.....	28
2.8 Summary	30
3.1 Polymers for Tissue Engineering.....	31
3.1.1. Natural Polymers	31
3.1.2. Synthetic Polyesters	35
3.2 Combining Natural and Synthetic Polymers.....	37
3.2.2. Coatings	39
3.2.3. Copolymerization.....	39
3.2.4. Blending.....	40
3.2.5. Composites.....	42
3.3. Materials and Methods.....	43
3.3.1. Sources for Material.....	43
3.3.2. Composite Layered Scaffold Fabrication.	44
3.3.3. Thickness Characterization.	46
3.3.4. Uniaxial Tensile Testing.....	47

3.3.5. Microarchitecture Analysis.	47
3.3.6. Permeability Measurement.	47
3.3.7. Degradation Characterization.	48
3.3.8. Cell Culture.	49
3.3.9. Cell Colonization.	50
3.3.10. Cellular Activity.	51
3.3.11. Statistical Analysis.	51
3.4. Results.	52
3.4.1. Composite Scaffold Physical Properties.	52
3.4.2. Tensile Properties.	54
3.4.3. Permeability to Urea.	55
3.4.4. Scaffold Degradation Characteristics.	57
3.4.5. Support for Cellular Activity.	60
3.5. Discussion.	65
3.6. Summary	68
4.1 Nanoparticles in Tissue Engineering	70
4.2. Materials and Methods.	74
4.2.1. Sources of Material	74
4.2.2. Synthesis of PLGA NPs	75
4.2.3. Forming Chitosan Nanoparticles	76
4.2.4. Characterization of Nanoparticles.	76
4.2.5. Microarchitecture analysis of nanoparticle modified structures	76
4.2.6. Particles integrated into composite structure	77
4.2.7. Characterization of properties of PLGA NP modified SIS	77
4.2.8. Urea permeability studies of NP modified SIS	78
4.2. Statistical analysis	79
4.3. Results.	79
4.3.1. Characteristics of synthesized NPs	79
4.3.2. Surface structure of NP modified SIS	80
4.3.3. Particles integrated into composite structure	83
4.3.4. The effect of NPs on SIS permeability	85
4.3.5. The effect of NPs on SIS mechanical properties	87
4.4. Discussion	88
4.5. Conclusion	92
5.1. Bioreactor Overview.	93
5.2. Materials and Methods.	97
5.2.1. Sources of Materials	97
5.2.2. Obtaining RTD function using CFD:	98
5.2.3. Obtaining RTD using experimental setup.	102
5.2.4. Analytical Model Derivation.	104
5.2.5. Preparation of porous structure.	105
5.2.6. Simulation including the porous structure.	106
5.3. Results and Discussion.	109
5.3.1. Steady state profile in unpacked reactors.	109
5.3.2. Residence time distributions without porous structure	111
5.3.3. Effect of porous structure on flow distribution.	115

5.3.4. Effect of changing pore sizes.	117
5.3.5. Effect of changing porosity.	119
5.4. DISCUSSION.	119
6.1. Introduction.	122
6.2 Materials and Methods.	124
6.2.1. Sources of Materials	124
6.2.2. Simulation nutrient distributions.	125
6.2.4 Cell culture.	126
6.2.3. Constructing an optical profiler	128
6.3 Results.	131
6.3.1. Simulating oxygen profile.	131
6.3.2. Effect of reaction on pressure drop and shear stress.	133
6.3.3. Effect of changing pore size on reaction.	134
6.3.4. Effect of changing the number of cells.	135
6.3.5. Experimental visualization of the oxygen profile.	136
6.5 Acknowledgements.	140
7.1. Summary.	141
Specific Aim 1.	142
Specific Aim 2:	143
Specific Aim 3.	143
7.2. Future Work.	144
7.2.1. Nanoparticle delivery of heterogeneous cellular signals	144
7.2.2. Complex scaffold architecture mimicking anatomical structures.	145
7.2.3. Mechanotransduction in bioreactor engineering.	146
7.2.4. Improving reactor simulations and the optical profiler system.	146
A.1: Mathematical Derivations.	148
A.2. CFX Walkthrough.	151
Building and running a CFX model.	151
CAD2Mesh	151
CFX-Pre	153
Making the Tracer.	153
Import the Mesh.	153
Setting up the simulation	153
Solver Manager.	156
Modifying the Simulation for Transient Flow	156
Solver Manager.	157
CFX-Post.	157
References.	159

LIST OF TABLES

Table	Page
Table 1. Summary of polymer properties	38
Table 2. Summary of composite structure properties.	69
Table 3. Effect of pore size and pore number on pressure drop and shear stress.	108
Table 4. Effect of reduced pore size with constant pore number on pressure drop and shear stress.	108
Table 5. V_{Max} and K_m valuse for different cell types.	125
Table 6. Pressure drop and shear stress within the reaction simulations at a variety of different flowrates.	134
Table 7. Effect on pressure drop and shear stress in reacting systems as pore size is decreased.	134
Table 8. Outlet oxygen concentration decreases as the number of cells increases.	135

LIST OF FIGURES

Figure	Page
Figure 1. Concept of Tissue Engineering	8
Figure 2. Layers within the Small Intestine	10
Figure 3. 2D and 3D Cell Culture	15
Figure 4. Factors influencing colonization in 3D	16
Figure 5. Types of Pores within the scaffold matrix.....	18
Figure 6. Types of porous polymer structures.	20
Figure 7. Micromechanical forces acting on a single cell in a porous structure.....	26
Figure 8. Schematic showing the steps involved in forming the composite scaffold.....	45
Figure 9. Construction of the Composite Scaffold	46
Figure 10. Diagram of the Chamber used in Permeability Experiments	48
Figure 11. Composite Scaffold Structure during Fabrication.	53
Figure 12. Stress Strain Characteristics.	55
Figure 13. Diffusion of Urea across Composite Membrane.	56
Figure 14. Composite Membranes Retain their 3D Structure during Degradation.	57
Figure 15. Degradation Characteristics of the Composite.	59
Figure 16. Composite Matrices Guide the Spreading, Adhesion, and Proliferation of MEFs.....	61
Figure 17. Composite matrices support fibroblast colonization and activity.	63
Figure 18. Composite matrices guide the spreading and adhesion of SMCs.....	64
Figure 19. SEM images of latex spheres modified SIS.	81
Figure 20. SEM images of PLGA NP modified SIS.	82
Figure 21. Particles integrated into the composite structure.....	84
Figure 22. Alteration of SIS permeability to urea by NPs.....	86
Figure 23. Stress–strain curves of SIS with and without PLGA NPs.	88
Figure 24. Schematic of reactor designs utilized in this study showing major dimensions	99
Figure 25. Reactor set-up used in experimentation.	102
Figure 26. Flow system used in reactor experiments.....	104
Figure 27. Steady state stream line profiles in different reactors simulated with a flow rate of 20mL/min.	110
Figure 28. Steady state stream line profiles in different reactors simulated with a flow rate of 156 mL/min	110
Figure 29. Concentration profiles at the reactor outlet for different times at the 20 mL/min flowrate.	112
Figure 30. of reactor shape on the residence time distribution of the tracer at 20 mL/min.	114
Figure 31. Effect of flow rate and porous structure on the residence time of the tracer.	116

Figure 32. Shear stresses within the porous structure for the case with 85 μm pore size and 120 pores/ mm^2 . Arrows indicate the flow direction.....	118
Figure 33. Cell culture technique used with the optical profiler.....	128
Figure 34. Coated glass slide inserted into reactor.	129
Figure 35. Diagram and photograph of the optics system.	131
Figure 36. Simulated oxygen profiles for the rectangular reactor	132
Figure 37. Simulated glucose profiles for the rectangular reactor.....	133
Figure 38. Effect of increasing the number of cells present in the simulation.	135
Figure 39. Fluorescent images from bioreactor in the optical system.	137
Figure 40. Surface Meshes and Velocity fields for Chapter 5 and Chapter 6, 85 μm pores, 120 pores/ mm^2 , 5 mL/min	140

Chapter 1

Overall Goal and Specific Aims

1. Introduction

A critical need exists to find alternatives to human organ transplantation. Due to a scarcity of available transplant organs 17 people die every day in the United States alone¹. Tissue engineering is a field that seeks to alleviate the transplant crisis using biodegradable matrices. The matrices support and guide the ingrowth of cells while the tissue regenerates, and then degrade away leaving only normal healthy tissue.

Currently a variety of materials are used for tissue engineering including natural, animal derived, matrices and synthetic polymer matrices. One example of a natural matrix used in clinical practice is small intestinal submucosa (SIS). SIS is a dense connective tissue harvested from the mammalian small intestine that has shown promise in clinical settings². However, natural matrices are inherently heterogeneous which creates problems with consistency and mass production³. The problem of heterogeneity inherent in natural matrices can be solved by building scaffolds using polymeric materials. Current research is searching for a polymer system that has both appropriate biological and mechanical properties.

By using polymers the mechanical properties and degradation time of the scaffold can be controlled. Additionally, standard polymer fabrication techniques can be used to generate porous scaffolds with a variety of structures. There are two major classes of

polymers: natural polymers and synthetic polymers. Natural polymers are derived from a variety of sources including fish scales, rat tails, and crab shells. Natural polymers have superior biological properties. However, they lack mechanical strength. One natural polymer is chitosan, a polysaccharide derived from N-deacetylation of chitin, a polymer present in the outer shells of crustaceans. Chitosan has been widely investigated in wound dressing and drug delivery systems⁴, and will support biological activity in diverse cell types⁵. Synthetic polymers such as poly (lactic acid) (PLA), poly (glycolic acid) (PGA), and their copolymers (PLGA, PLLA, etc)⁶⁻¹² have generated immense interest as tissue engineering materials owing to their widespread use in a variety of biological applications for more than three decades and their strong FDA approval history¹³.

Recent developments in tissue engineering have shown that the 3D porous architecture plays an important role by guiding colonization of cells and subsequent regeneration¹⁴. Both structural properties such as pore size, porosity, and topography and biochemical properties such as surface charge, chemical composition, and cellular binding domains affect tissue regeneration. Mechanical stimulation and cellular signaling also direct the colonization, proliferation, and differentiation of cells in the porous matrix during regeneration¹⁵. Various technologies have been developed to generate porous matrices from a variety of polymers. For example, one method for combining the two polymer systems involves fabricating a composite structure using both natural and synthetic polymers, one to provide mechanical strength and another to provide biological activity¹⁶. While a fundamental understanding of the various factors that go into the design of the porous materials have been studied, it is important to

determine the major processes that occur during tissue regeneration. The transient changes in the porous material are not well understood, especially in regenerating large sections of tissue required for applications such as skin, bladder, and cartilage.

An important aspect of scaffold design is oxygen and nutrient transport through the porous structure. Before new microvasculature has formed, cells within the scaffold are dependant upon the transport of oxygen for survival. Therefore it is important to study the oxygen transport across the scaffold. There are several possible ways to grow cells within the scaffold. Standard cell culture practice calls for cell to be grown in batch culture on flat, stationary plates. While this method has been successfully used for years, the cells will only form a monolayer making it difficult to propagate large numbers of cells. Batch culture systems also introduce a transient element to the system. The concentration of nutrients and waste products changes over time. The transient aspects can be removed by using a continuous flow system. Perfusion reactors provide a constant flow of media to the scaffold. Because they are continuous flow reactors, the concentration of nutrients, signaling molecules, and waste products can be more effectively controlled. Bioreactors have been designed to encourage 3D cell growth and colonization. Several bioreactor types have been designed to grow functional 3D tissue engineering scaffolds¹⁷. However, most of the previous work uses very small samples that are not suitable for regenerating large sections of tissue required for applications such as skin, bladder, and cartilage. Hence, a better fundamental understanding of tissue regeneration in such high aspect ratio (large size to very small thickness) systems is required.

Natural matrices contain growth factors and other signaling molecules important for tissue regeneration. However, synthetic polymers lack cellular signaling molecules important to tissue regeneration. Another method to improve tissue regeneration is to incorporate a controlled release particle system into the polymer scaffold in order to regulate cellular signals. The controlled release system will also create local scale transport barriers in the matrix. Therefore, the particles embedded in the porous matrix could be used to tailor the properties of for specific applications.

Another key development in bioreactor design is the use of mechanical forces to aid tissue development. Some native tissues regenerate better under the influence of mechanical forces. Therefore, tissue regeneration can be encouraged by including changes in the mechanical force experienced by the scaffold. One easy way to vary the mechanical loading in a reactor is to change the pressure.

The mechanical reinforcement utilized in composite scaffolds creates transport barriers within the system. On a macro level these barriers could lead to a disruption in the flow distribution and cause dead spots (areas with low flowrates) that are not desirable in tissue engineering bioreactors. Additionally, changes within the porous structure during fabrication or tissue regeneration can affect both the pressure drop across the matrix and the shear stresses within the matrix. Therefore, a better understanding and control of the flow phenomena within the porous matrix should enable improved scaffold designs and consequently improved tissue regeneration.

The purpose of this study was to understand the transport properties within high aspect ratio polymer matrices for the purposes of improving the design of synthetic tissue engineering scaffolds. The underlying hypothesis being that incorporation of a

nanoparticle controlled release system into composite polymer scaffolds will enable the cellular microenvironment to be modified for specific applications in tissue regeneration. Further, studying oxygen transport within the scaffold in order to better control flow distribution, shear stresses, and pressure drop within the material is important to improve the quality of the regenerated tissue. This work helps in defining basic engineering principles in mass transport processes during tissue regeneration, and enabling the design of improved bioreactors, giving hope to the patients on the waiting list and their families.

Specific Aim 1: Understand the use of nanoparticles for local delivery of signaling molecules within porous structures.

This portion of the study aimed to examine the influence of localizing nanoparticles on the mass transport of nutrients through porous scaffolds. Nanoparticles can be used to deliver proteins important in cell signaling. The end goal is to develop a delivery system for signaling molecules in order to improve the regenerative effects of synthetic scaffolds while retaining their controllable physical properties. Nanoparticles from both synthetic (PLGA) and natural polymers (chitosan) were synthesized. These particles were incorporated at various densities into the composite scaffold and small intestinal submucosa, a natural matrix. Then, the effect of the particles on the scaffold's mass transfer properties was measured based on the permeability of the matrix to urea both before and after modification. In addition, changes in biophysical properties and microstructure were assessed.

Specific Aim 2: Modeling fluid flow through porous scaffolds

Flow within bioreactors containing large porous structures with high aspect ratios has not been studied. Non-uniform flow patterns lead to i) poor distribution of nutrients and ii) non-uniform shear stress distribution. These factors affect cellular colonization and the assembly of extracellular matrix elements which affect the quality of regenerated tissues. Further, porous characteristics change during tissue regeneration affecting mass transport. There are two basic ways to change the scaffold's porous structure, during fabrication (where the number of pores for a given area is tied to the pore diameter) and during regeneration (where the cells grow in reducing the pore diameter but leaving the number of pores per area constant). Hence, one has to understand the fluid distribution and the effect of shape of the reactor.

The non-ideal fluid distribution is characterized using the residence time distribution (RTD). The RTD measures the amount of time different molecules present in the fluid spend within the reactor. In other words, the RTD is a measure of dispersal of a molecule in a flowing medium owing to the combined action of a velocity profile and molecular diffusion. Understanding these characteristics is important in designing the reactor shape and optimizing the location of the inlets and outlets. This study utilized a well understood parallel plate reactor and evaluated the effect of porous structure in the flow domain. A parallel plate reactor with three different inlet and outlet conditions was simulated using CFD packages CFX 11 (ANSYS Inc, Canonsburg, PA.) and/or Comsol Multiphysics 3.4 (COMSOL, Inc., Burlington, MA). Additionally, the effect of the scaffold's porous structure on both shear stress and pressure drop within the scaffold were investigated using the COMSOL software. Simulations were performed to

investigate the effect of changing the porous structure on shear stress and pressure drop within the matrix. Further experiments were performed to validate the simulation results.

Specific Aim 3: Modeling transport and consumption of oxygen through cell seeded scaffolds.

One cause of poor quality of regenerated tissue is hypoxia, a lack of oxygen in the center of the scaffold. Modeling oxygen transport in a cell seeded tissue engineering construct requires that the effects of cellular respiration be included. In order to combat this problem a computer model was developed to visualize the transport of oxygen through the porous scaffold. Cellular oxygen consumption was calculated using rate data available in the literature. The consumption of oxygen was included into the simulations using the chemical reaction capabilities of the COMSOL Multiphysics software. Simulation data for both chondrocytes and smooth muscle cells was used to determine a range of flowrates where the oxygen profile may be visualized using a coated glass slide where the coating's fluorescence is quenched by oxygen.

Further, attempts were made to validate the model using bioreactor experiments similar to Specific Aim 2. A benchtop optical system containing the same geometry of bioreactor as the computational model was constructed. Oxygen concentration was measured using oxygen to quench the fluorescence of a ruthenium compound. The top of the reactor was a glass slide coated with ruthenium, and the oxygen profile was visualized. Using this technique data from the CFD model can be verified, but future research is needed visualize the oxygen profile experimentally.

Chapter 2:

Porous Materials and Material Properties

2.1 Tissue Engineering Basics

The basic approach of tissue engineering uses biodegradable scaffolds to support and guide the in-growth of cells. Cells are seeded on a degradable porous structure. The cells colonize the material and proliferate, filling the scaffold structure as it degrades away. Eventually, the scaffold material degrades away leaving only normal healthy tissue¹⁸⁻²⁰ (**Figure 1**).

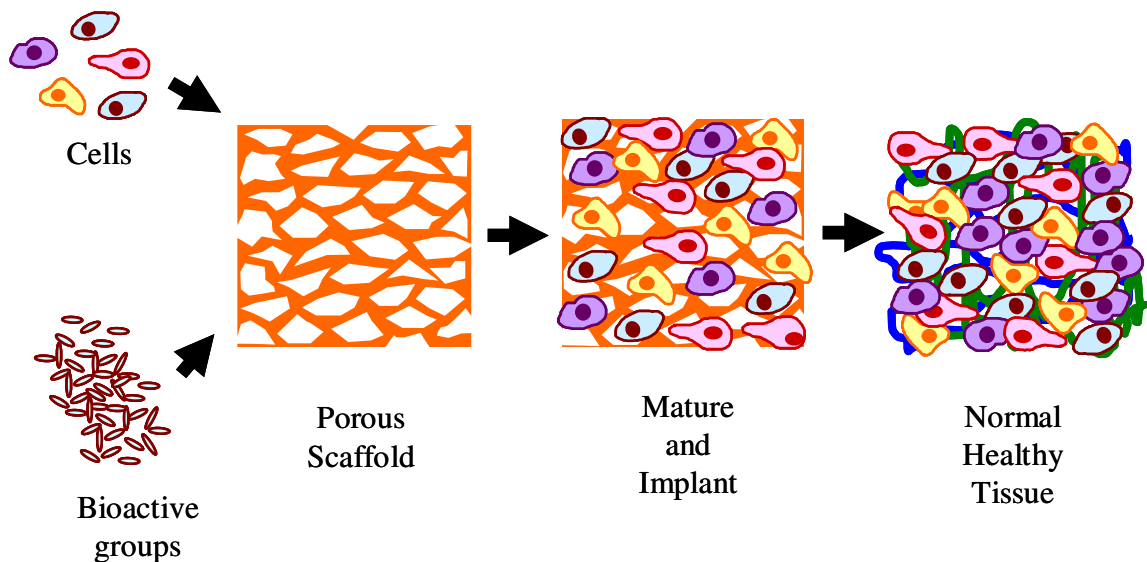


Figure 1. Concept of Tissue Engineering

The scaffold must provide enough mechanical strength to withstand physiological stresses, must provide an environment suitable for cellular growth, and should contain suitable biological properties to support cellular attachment, proliferation, and differentiation. Porous structures being used as degradable scaffolds should have the following basic properties. The scaffolds should be:

- (1) biocompatible, bioresorbable, and biodegradable during tissue regeneration process.
- (2) porous with an interconnected network to enable rapid tissue ingrowth through pores, and to allow unimpaired diffusion of nutrients, oxygen and wastes.
- (3) able to support cell attachment, proliferation, and differentiation, as well as have suitable surface properties (wettability, stiffness, and compliance).
- (4) mechanically strong, able to withstand stresses at the site of implantation.
- (5) biodegradable with biocompatible, non-toxic, and removable degradation products.

Scaffolds generated from natural polymers²¹, synthetic polymers²², or by removing the cellular components from xenogeneic tissues²³ have been used with and without prior cell-seeding to support and guide the in-growth of cells. The unseeded techniques involve the direct *in vivo* implantation of a biodegradable scaffold into the body, allowing the natural process of regeneration to occur. In contrast, seeded techniques utilize *in vitro* cell culture on biodegradable scaffolds to establish cell-composite grafts, followed by *in vivo* implantation of the grafts.

2.2 State of the Art: Natural Matrices

One option for creating tissue scaffolds is to use extracellular matrix (ECM) components derived from animal sources. For example porcine acellular dermis has been used for skin regeneration²⁴ and control of hypertrophic scarring²⁵. The human umbilical vein, a portion of the umbilical cord that is typically discarded, has been used for engineering blood vessels and vasculature^{26, 27}. Additionally, decellularized scaffolds derived from porcine heart valves²⁸, human pericardium²⁹, and whole rat hearts³⁰ have been used for cardiac tissue engineering. For more information, a thorough review of natural matrices has been written by Badylak.³¹

One natural matrix of particular interest is small intestinal submucosa (SIS). SIS has shown significant success in various tissue engineering applications³². SIS is a dense connective tissue harvested from the small intestine. SIS is obtained after removing the mucosa, serosa, and muscle layers from the harvested tissue (**Figure 2**).

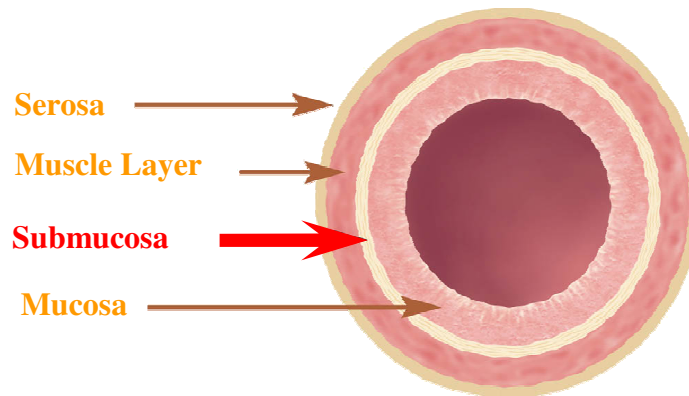


Figure 2. Layers within the Small Intestine

Porcine SIS has generated immense interest in various tissue engineering applications due to its diverse favorable properties^{33, 34}. SIS does not require cell seeding prior to in vivo implantation for bladder regeneration². SIS is rich in type 1 collagen, biocompatible, pliable, and resistant to infection. Additionally, SIS has a resorption rate of 4-16 weeks^{35, 36} and its immune response shows a phenotypic characteristic of tissue remodeling rather than rejection³⁷. SIS promotes cell migration of numerous cell types and has been tested for regeneration of diverse tissues including large vascular grafts³⁸, venous valves and leaflets³⁹⁻⁴¹, skin⁴², tendons⁴³, and wound dressing⁴⁴. For urinary tract reconstruction, SIS has been used for bladder augmentation⁴⁵⁻⁴⁷, for ureter⁴⁸ and urethra^{45, 49} replacement, and to promote regeneration of transitional epithelium, smooth muscle, and peripheral nerves with no evidence of immunological rejection⁵⁰. Long-term studies show that SIS grafts can be remolded and replaced by the host and such regenerated tissues become histologically indistinguishable from native tissues⁴⁶. The remodeled tissue shows complete regeneration of all three layers (mucosa, smooth muscle, and serosa) of the bladder in rat⁵¹ and dog^{52, 53} models with only problem being low quality and disorganized smooth muscle fibers.

However, large-scale preparation of SIS is hindered by various physiochemical properties which affect the quality and reliability of the tissue regeneration in clinical settings. A number of trials have clearly demonstrated that not all SIS materials are the same^{47, 54-56}. Investigations indicate that SIS from older pigs (>3yrs) is superior in regards to bladder regeneration than SIS from younger pigs (<8 months), multi-ply SIS (4 layer) does not produce reliable bladder regeneration compared to single-ply SIS, machine and hand-made SIS have similar outcomes, E-beam sterilization results in

severe contraction and bone formation within the graft in addition to increased graft contraction relative to SIS prepared by ethylene oxide (used in commercial preparations) or peracetic acid, and the physical and mechanical characteristics of the matrix, such as permeability, thickness, tensile properties, fatigue properties, and ultrastructural properties, vary depending on the age of the animal, the sterilization technique, and the location within the small intestine it is harvested from.³ Distal SIS demonstrated the most desirable tissue regeneration. In a canine model study, bladder augmentation with distal SIS showed remarkably enhanced bladder regeneration relative to proximal SIS⁵⁷. Further, SIS obtained from the distal of the intestine enables better cellular ingrowth and tissue remodeling than SIS taken from the proximal region². Thus, forming synthetic matrices with physiochemical properties similar to distal SIS will be useful in bladder and other soft tissue regeneration.

2.3. Formation of Three Dimensional Polymer Scaffolds

One way to overcome the heterogeneity in natural matrices uses polymers to fabricate degradable 3D porous matrices. Several techniques have been developed to fabricate porous scaffolds, including solvent casting/particulate leaching⁵⁸, fiber bonding (unwoven meshes)⁵⁹, gas foaming⁶⁰, and phase separation/emulsification⁶¹. Another method to fabricate porous scaffolds is to introduce a porogen such as salt (NaCl) into the polymer and then remove it with a solvent (particulate leaching)⁶². The leaching of salt from a polymer composite can form pores within scaffolds, the pore sizes are dependent on the size and amount of salt crystals. Pore size and distribution is difficult to control. Gas porogen has been used as alternative to eliminate the use of organic solvents (gas

foaming). But the pores created in this method are non-uniform, limiting cell seeding and migration⁵⁹.

Scaffolds can be formed using 3D printing techniques⁶³. Scaffolds are built layer by layer, and the pore size and spacing are controlled by the pattern used. The advantage to 3D printing is the control of pore size and distribution. The disadvantage is that the fiber diameter limits the pore sizes and configurations possible. Currently, construction is limited to a 150 μm fiber diameter⁶⁴. Direct writing processes are also limited by the ink used. To assure successful printing the ink must be viscous enough to hold its shape after printing but not so viscous that it is too difficult to pump. Additionally the ink must quickly form the polymer fiber after printing, as well as bond to previously printed layers.

3D porous scaffolds can also be created using standard microfabrication techniques⁶⁵ including microembossing⁶⁶ and soft lithography^{67, 68}. Microfabricated scaffolds can be produced that contain both pores and nano-scale surface features, enabling better control of the cellular microenvironment.

Scaffolds with nanofibers can be produced using electrospinning process^{69, 70, 71}. In the process of electrospinning a non-woven matrix is formed by directing a charged polymer solution at an oppositely charged collector. Additionally, changing the orientation of the collector can produce both random and aligned nanofiber arrangements, and multiple nozzles can be used to more carefully control the distribution of fibers.

Three dimensional scaffolds can also be formed using hydrogels, water soluble polymers crosslinked into a 3D matrix⁷². One of the prime advantages to hydrogels is that they can be polymerized *in situ* by thermo-gelling⁷³ or photocrosslinking^{74, 75}.

Another advantage is that cells can be encapsulated directly into the scaffold, providing faster tissue ingrowth. In autoimmune disorders, like diabetes, hydrogels can serve as a protective barrier between the implanted functional cells and the immune system ⁷⁶.

Due to a number of advantages this research utilizes controlled rate freezing and lyophilization to create the porous chitosan structures ⁷⁷. By controlling the rate of freezing, ice crystals form in the solution following the path of heat flow. While the solution freezes the polymer precipitates out of solution and is trapped between the ice crystals. The solvent is then removed by freeze drying, leaving the porous polymer structure intact. The pore size is determined by the size of the ice crystals. Therefore, the size and orientation of pores can be directed by controlling the rate and direction of freezing. By freezing at a constant temperature the pore size becomes a function of freezer temperature; quicker freezing will produce smaller pores. This process also avoids heat denaturation of biological materials because it is performed at low temperature. This allows bioactive molecules to be included in the scaffold without altering their activity, if necessary.

2.4 2D vs. 3D Cell Culture

Many of the cell culture experiments performed in molecular biology are cultivated on two-dimensional (2D) tissue culture treated surfaces. Many *in vitro* experiments have shown that cells have different responses in colonization, proliferation, and differentiation on 3D scaffolds than on traditional 2D-tissue culture. In 2D substrata, cultured cells are restricted to spread and attach to a flat rigid glass or tissue culture plastic surface (**Figure 3**). Hence, biophysical properties of the matrix that provide spatio-temporal effects in the body are not present in 2D culture. However, biophysical

properties significantly influence cell adhesion and functions in three-dimensional (3D) environment ¹⁴. 3D matrices provide physical cues to guide cell colonization as well as chemical cues of cell-binding sites to support cell attachment and spreading. Tissue engineering has given promise for generating functionally replaceable 3D tissue parts, although currently the products obtainable are limited to avascular regions.

Biodegradable scaffolds are used to support and guide the in-growth of cells i.e., they form the template for cell colonization. Scaffolding material eventually disappears leaving only the necessary healthy tissue in a topologically required form ^{18, 20, 78}. The 3D matrix provides more space for cellular colonization and proliferation as well as provides a different set of physiological signals to the developing tissue.

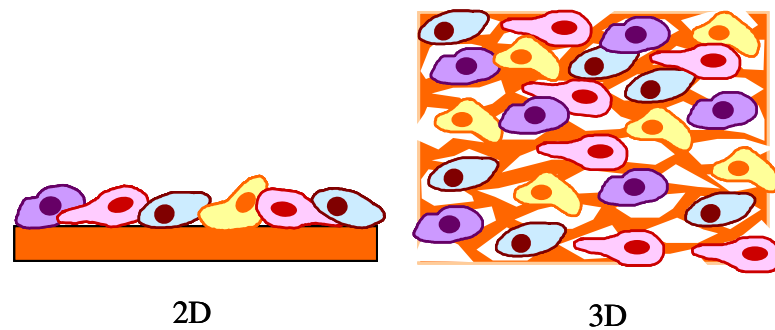


Figure 3. 2D and 3D Cell Culture

2.5 Importance of 3D Spatial Architecture

It is important to learn what scaffold properties most affect cellular colonization and ingrowth because there are a wide variety of methods to fabricate degradable porous structures. As mentioned earlier, cells respond differently in 2D and 3D culture as a result of both the 3D porous structure as well as surface properties. The influence of spatial architecture of the porous matrix has been explored in various experiments. These studies^{18,78} have shown in addition to chemical cues and surface properties, 3D matrix physical properties such as stiffness,⁷⁹ hydrophilicity, porosity,⁸⁰ pore size and void fraction^{81,82} can affect cell morphology, attachment, and function (**Figure 4**). Especially the spatial structures or the topography of scaffolds influence neuron alignment, orientation,⁸³ multicellular organization,⁸¹ endothelial cell spreading⁸⁴ and microvascular epithelial cell attachment.⁸² 2D surface features such as edges, grooves, steps, roughness and pores of substratum significantly influence cell behavior.^{83,85}

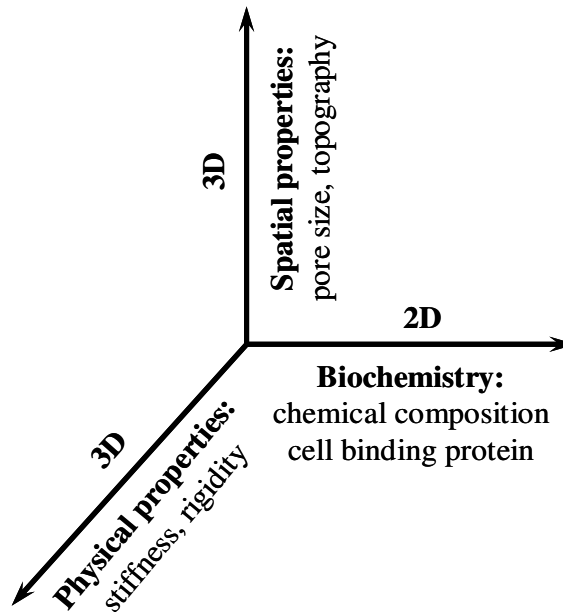


Figure 4. Factors influencing colonization in 3D

Important structural properties include both the mechanical properties inherent in the material, such as break stress, modulus of elasticity, and stiffness, but also the properties of the scaffold's 3D architecture.⁸⁶ Both the microscale properties experienced by the cells and the bulk material properties that provide physical support for both the scaffold and the surrounding tissue become important during tissue regeneration. The major architecture features discussed below include porosity, pore size, fiber orientation, pore interconnectivity, topography, and scaffold stiffness.

2.5.1 Porosity

A highly porous scaffold (>90% porosity) is desirable, since it can support the growth of tissue for the necessary nutrients transport^{87, 88}. Porosity is a measure of the open pore volume within the matrix, often called the void fraction. Mathematically, porosity is defined as follows:

$$\text{Porosity} = \frac{\text{Open Pore Volume}}{\text{Total Volume}} \quad (1)$$

Several pore types are possible within a porous matrix (**Figure 5**). Open pores have cellular access on both sides and allow for liquid flow and transport of nutrients through the porous matrix. Partially open pores are accessible on one side. They allow access for cell colonization, but mass transport of nutrients and waste products is limited to diffusion. Closed pores have no openings and are not accessible by cells. Other issues that complicate porosity are pore tortuosity and heterogeneous pore diameters. Consequently, materials for tissue engineering materials concentrate on creating an open pore architecture.

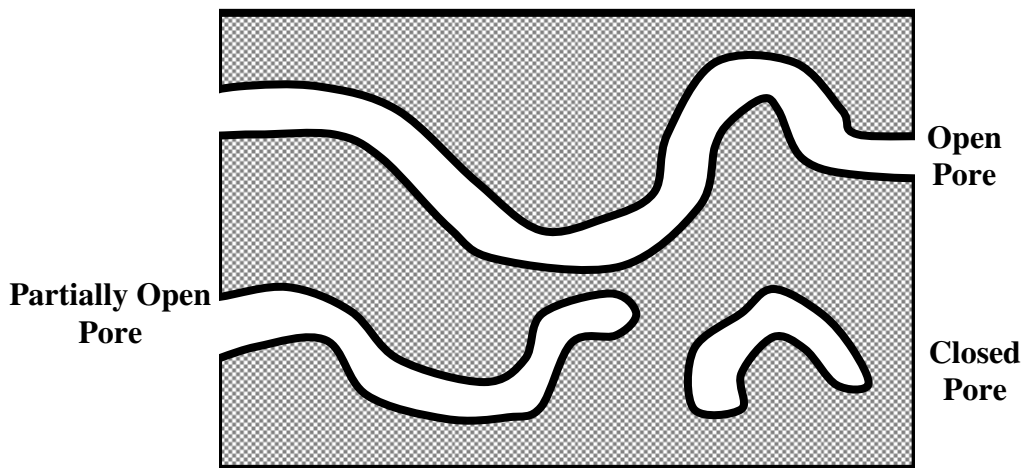


Figure 5. Types of Pores within the scaffold matrix

Porosity also plays an important role in regulating cell adhesion and migration. High porosity provides a high surface area for cell-matrix interactions, sufficient space for ECM regeneration, uniform and efficient cell seeding.⁸⁹ Higher porosity could also lead to increased cell adhesion.⁹⁰ Pore interconnectivity increases the overall surface area for cell attachment and facilitates cell ingrowth in the scaffolds. Increased interconnectivity and porosity also affect the deposition of ECM elements.⁹¹

A functional approach to compare porous structures in a variety of materials is through their mass transport properties, such as permeability. The method of Raghavan *et al.* is one way to determine the permeability of the matrix,³ quasi steady-state transport between two sealed chambers is assumed and the following equation is used:

$$\ln \left[\frac{C_1 - 2C_2}{C_1} \right] = - \left[\frac{A_m}{V} P \right] t \quad (2)$$

where C_1 is the initial concentration of the compound of interest, C_2 is the concentration of the compound of interest at time t . A_m is the area of the matrix normal to the mass flux, V is the volume of the test chamber, , and P is the permeability. Permeability is related to the diffusion coefficient by

$$P = \frac{D_m \phi}{L} \quad (3)$$

where D_m is the diffusion coefficient, ϕ is the partition coefficient, L is the thickness of the membrane.

2.5.2 Pore Size.

There are a variety of ways to fabricate porous materials, but there are three key methods. Porous matrices may be derived from heterogeneous natural matrices, by forming void spaces within a polymer, or by creating a layered bed of polymer fibers (**Figure 6**). One method for generating scaffolds uses a two phase polymer/porogen system where the porogen is subsequently removed, leaving a system of interconnected pores. The pores can be aligned by controlling porogen formation or alignment. Example of this technique are controlled rate freezing and lyophilization (CRFLT)⁷⁷ and salt leaching.⁹² In CRFLT the pore alignment is controlled using the rate and direction of heat transfer.^{77, 93} Creating a uniform pore size and distribution is a common problem when working with porous 3D matrices. Firstly, the porous structure is usually formed in an asymmetric fashion. Non-spherical pores form where one axis is much longer than the other. The spatial arrangement of pores within the material may also be an issue. For

example, in scaffolds frozen at constant temperature pores are formed in the direction of heat transfer. If a sample insulated on one side and placed in a freezer then areas near the surface of the scaffold (exposed to cold air) will freeze faster than areas deeper within the scaffold. The faster rate of freezing near the surface causes small ice crystals (and thus smaller pores) to be formed near the top edge of the scaffold material.

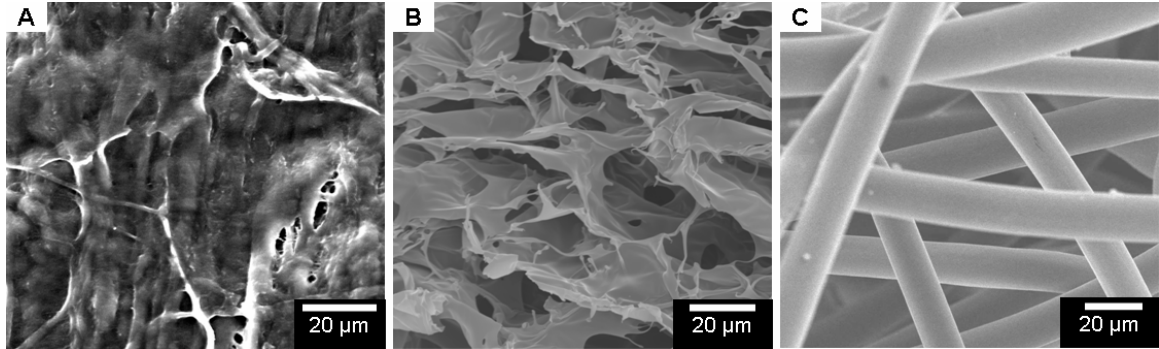


Figure 6. Types of porous polymer structures.

A) Heterogeneous structures, porcine SIS. B) Pore based structures, freeze dried chitosan scaffolds. C) Fiber based structures, poly (glycolic acid) mesh

Pore size refers to the distance between solid sections of the porous matrix. Pore size is typically reported as the diameter of circular pores or the major axis for noncircular pores. Pore size affects cell binding, migration, depth of cellular in-growth, cell morphology and phenotypic expression.⁹⁴ Importantly, appropriate pore size provides structural advantages to allow cells to spread into the pores through “bridges” from adjacent cells. There is an “optimum size range” for supporting cell ingrowth. Outside this range, cells fail to spread and form networks. The optimal pore size range depends on the materials as well as cell types.⁹⁵ Many mature cell types including endothelial cells (ECs) are unable to completely colonize scaffolds with the pore sizes >300 µm due to the difficulty in crossing large bridging distances.⁹⁶⁻¹⁰⁰ An “optimum

pore size range” for supporting cell ingrowth for majority of the mature cell types (except osteoblasts and osteocytes) is in the range of 100 -150 μm .⁹⁶ Recently, it was shown that gelatin-chitosan scaffolds (3:1) with 50-80 μm pore size diminished the viability of fibroblasts and ECs, relative to 100 to 150 μm pore size chitosan scaffolds.⁵ Pore sizes not only affect cell growth, but also affect scaffolds properties. For example, the elasticity of microporous scaffolds increases as the number of pores within the scaffold increases.¹⁰¹

2.5.3 Fiber Thickness.

The matrix may also be characterized based on the microscale thickness of the individual material fibers. In some cases where the material is formed from a bed of stacked fibers fiber thickness is characterized as the diameter of the individual fibers. The fibers may be distributed randomly, as in electrospinning⁶⁹⁻⁷¹ or form a highly organized system with regular repeating pore units, as in solid freeform fabrication.¹⁰² Thus the fiber thickness, length, width and shape (circular rectangular, etc) must be evaluated. However, defining fiber thickness may not be suitable when pores are formed by CRFLT and salt leaching technique. Utilizing freeze dried scaffolds the material forms an interconnected series of planes that connect the pores.

Fiber orientation within a scaffold affects cell colonization. Scaffolds made of oriented polycaprolactone nanofibers (700 nm in diameter) were found to promote phenotypic differentiation of chondrocytes compared with 2D nonporous membranes.⁷⁰ Cells seeded on oriented fibrous structures tended to maintain phenotypic shape and had guided growth according to nanofiber orientation. Another study showed that significantly more collagen was synthesized by fibroblasts on aligned nanofibers than

randomly orientated fibers despite similar proliferation.⁷¹ A hypothesis is that spindle-shaped and oriented fibroblasts in the direction of aligned fibers mimic *in vivo* condition better and thus produce more ECM. Further studies are necessary to understand the mechanisms involved in these cell-matrix and cell-cell interactions.

2.5.4 Topography.

The surface characteristics of scaffold materials can be described by their topography, micro to nano-scale material surface features. Topography of scaffold surface influences spreading characteristics and activity of cells.¹⁰³ The existence of grooves may inhibit cell movement to bend its cytoskeleton¹⁰⁴ or reshape its actin filaments to adjust to the new topography.¹⁰⁵ Curtis proposed a term “topographic reaction” to describe that cells react as a response to substratum in microscale through changes in cell orientation, motility, and adhesion.⁸⁵ Surface roughness can significantly increase cell migration area.¹⁰⁶ Nanometer scale roughness has been shown to improve the adhesion and growth of both smooth muscle cells¹⁰⁷ and chondrocytes¹⁰⁸ on polymer scaffolds. However, the mechanisms for enhanced cell behavior are not completely understood. Additionally, the porous structure may be modified post fabrication by inclusion of nanoparticles¹⁰⁹ or etching the surface of the matrix.¹⁰⁷

Altered surface texture and charge could also affect cell spreading.^{14, 107} In a separate study, antibacterial chitosan was blended with PCL and showed that blending compromises the antibacterial property of the material.^{110, 111} Further, the blend membranes showed better support for fibroblast spreading and proliferation. Surface roughness analysis of blend membranes showed significant increase in roughness relative to chitosan membranes, and observed antibacterial activity could be partially attributed to

changed topography. Nevertheless, decreased antibacterial activity could also be due to altered surface charge distribution. Additionally, colonization and proliferation of mammalian cells may be affected by altering the charge distribution within the porous structure.¹¹²

2.6. Cellular Interaction

2.6.1. Changes in Cell-Adhesion.

An important part of cell colonization is cell signaling. Cellular adhesion, proliferation, and differentiation can be modified using specific signaling molecules, such as growth or differentiation factors. The presence of specific cellular binding sites greatly enhances cell adhesion. The proliferation and differentiation of various cell types may be controlled by incorporating signaling molecules into the tissue engineering matrix.

To incorporate bioregulation of matrix elements, grafting a small peptide Arginine-Glycine-Aspartic acid (RGD) onto polymers is an approach taken by many investigators.¹¹³ The use of RGD is based on the understanding that the majority of communication across the cell wall takes place via integrins, which communicate with many matrix elements through the RGD binding domain. Additionally, materials such as collagens, glycosaminoglycans (GAGs) and their analogues (eg. Dextran sulfate) can be incorporated into the scaffold structure in order to direct cellular growth and provide binding sites.^{113,112} Our group has previously shown that the presence of binding sites improves cellular adhesion. Endothelial cells were grown on films of chitosan, gelatin or a blend of the two and then subjected to shear stresses similar to those present in arteries

or veins for three hours. Cells remained attached to the blends containing gelatin, but no cells were found adhered to the pure chitosan film.¹⁴

Bioregulation of the porous matrix can also be achieved by the incorporation of growth factors. For example growth factors such as vascular endothelial growth factor (VEGF)¹¹⁶ and basic fibroblast growth factor (bFGF)^{114, 115} as well as ECM components such as fibronectin¹¹⁶ are important in angiogenesis. Growth factors are typically proteins with short half-lives. Therefore, a controlled release system is needed in order to protect the growth factors and provide a sustained signal. Cells will also receive signals from other cells within their vicinity. Therefore, various co-culture techniques allow communication between multiple cell types.¹¹⁷

Many cell types such as fibroblasts, mesenchymal stem cells, epithelial cells, and neural crest cells show different adhesions when grown on 3D matrices as opposed to 2D cell culture.¹¹⁸⁻¹²⁰ A possible reason is that the 3D architecture could distribute binding sites in a variety of special locations rather than on only the single plane of rigid substrate as in traditional 2D architecture.^{120, 121} Cells may have cytoskeletal adaptor proteins on 3D matrix in addition to proteins present in 2D focal adhesions.^{120, 122} For example, focal adhesion kinase (FAK) in 3D matrix adhesion is poorly phosphorylated at its major tyrosine phosphorylation site for cell adhesion. Such differences in cell adhesion between 2D and 3D matrices lead to different signal transduction and subsequent alteration in cellular rearrangement.

2.6.2. Mechanotransduction.

The mechanical forces a scaffold is subjected to during tissue regeneration should also be accounted for during cell colonization. Studies have shown that both hydrodynamic stresses^{5, 123} and mechanical stresses¹²⁴ affect cell colonization. For example, endothelial cells⁵ and chondrocytes¹²⁵ grown in a perfusion reactor align cells in the direction of flow. Beyond the structural modifications, shear stress initiates a number of signal transduction cascades leading to altered gene expression profiles and functional changes, particularly in endothelial cells¹²⁶. *In vitro* studies have shown that shear stress activates mitogen-activated protein (MAP) kinases (including extracellular signal regulated kinase and c-Jun N-terminal kinase)¹²⁷⁻¹²⁹, and kinases involved in focal adhesion such as FAKs, Src family kinases, and phosphatidylinositol 3-kinase¹³⁰. Mechanical forces affect cells in a variety of ways including opening or closing ion channels (changing mass transport properties across the cell membrane) and unfolding selected protein domains (providing access to a different set of binding sites.)¹³¹

Flow through the scaffold microarchitecture dictates the local shear stress rates experienced by the cells. Further the scaffold architecture controls the transport of nutrients within the samples. Channeling and other flow irregularities can result in local hypoxia or extracellular matrix washout.¹³¹ The presence of flow within a reactor also affects the production of ECM elements, for example rat bone marrow cells produce greater mineralization in scaffolds under direct perfusion.¹³²

Once the scaffold is placed into a flow system (either implanted *in vivo* or grown *in vitro* in a bioreactor) the effect of loading from both external forces and fluid flow can affect cell colonization. While the scaffold itself will be subjected to the bulk forces

supplied by the tissue and fluid flow, the cells will experience the micromechanical properties of the individual fibers and local shear stresses within the porous structure (**Figure 7**). The cell senses both the porous structure and other cells near where it is attached. An important step in characterizing the porous structure is to examine microenvironment surrounding the cells.

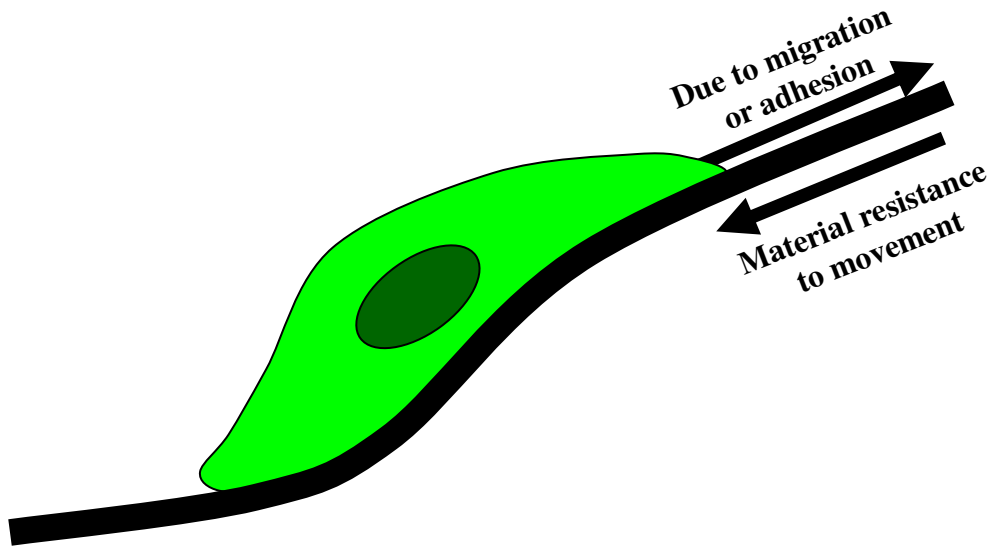


Figure 7. Micromechanical forces acting on a single cell in a porous structure

Cellular activity is influenced by the stiffness of the substrate.¹³³⁻¹³⁵ Stiffness is the resistance of the material to deformation, typically reported in force per distance. It is the slope of the load - extension curve. The dimensionality may be removed from the stiffness calculation by using the modulus of elasticity. The modulus of elasticity is the initial slope of the stress – strain curve. However, the thickness of the material must be measured to calculate the modulus of elasticity, and the thickness measurement becomes a major source of error when measuring very small thicknesses. The bulk stiffness controls the overall deformation of the matrix while each individual cell will encounter the stiffness of the individual fibers during colonization. Cells show reduced spreading

and disassembly of actin even when soluble adhesive ligands are present in weak gels.^{136,}
¹³⁷ This could be via the response of tractional forces between cells and materials;
scaffold should be able to withstand cell contractile forces.¹³⁵ Maximum tractional force
generated by a cell could be as much as 10-15% of substrate modulus.¹³⁶

In an effort to develop anti-scarring therapies in wound healing, understanding the
process of increased collagen packing has been extensively investigated^{138, 139}. A variety
of cell- or matrix- based continuum modeling has also been attempted.^{140, 141} It is very
well established that fibroblasts hug the collagen fiber and induce tractional forces. The
developed tractional forces lead to the generation of contractile forces which are essential
for alignment of collagen fibers and tissue healing. Thus, one of the approaches to
minimize scarring is to increase the tensile strength via wound dressing materials. 3D
collagen sponges have been used alone^{142, 143} or in conjunction with basic fibroblast
growth factor,¹⁴⁴ fibronectin, or hyaluronic acid.¹⁴⁵ Exogenous collagen increased wound
tensile strength and increased degree of reepithelialization i.e., early dermal and
epidermal wound healing. Further, hyaluronic acid and fibronectin may also be involved
in faster wound healing via helping the migration of fibroblasts.¹⁴⁶ However, it is not
clear whether these treatments reduced scarring in the long term. Nevertheless, the
rigidity of the scaffold affect the formation of extracellular matrix which affect cellular
activity.¹¹⁹

2.7. Matrix Turnover.

Cell colonization also involves the deposition of extracellular matrix elements. Cells can synthesize extracellular matrix components in response to different physical and chemical signals from surrounding 3D matrix. Unlike 2D architecture the degradation of a 3D matrix can create more space for cell expansion and migration. Scaffold degradation rate should be synchronized with the cell growth rate to ensure no space restriction due to slow degradation rate or the loss of structural support due to faster degradation. Key factors include the mode of degradation. For example, synthetic polyesters are hydrolytically degraded;²² therefore, they will begin to break down if they are not protected from moisture. Conversely, natural polymers, such as chitosan, are enzymatically degraded and can be stored in hydrated condition.⁷⁷ Dynamic changes during the degradation process must also be accounted for. Some materials (hydrogels) can swell several times their dry weight.¹⁴⁷ It has also been shown that cellular constructs grown *in vitro* will shrink, possibly as a result of cellular attachment and contraction or as a result of hydrodynamic forces compressing the scaffold. The molecular weight of a polymer will also change over the course of degradation. Amorphous 50:50 PLGA shows an 80% drop in molecular weight over the course of eight weeks which reduces the polymer's tensile break stress by 75%.¹⁶ Another positive aspect of degradable polymer systems is that they can also be used for the controlled release of bioactive molecules. Degradable polymers have been used for drug delivery for years. Recently they have been used to deliver growth and differentiation factors within tissue scaffolds.¹⁴⁸

Matrix turnover significantly influences cellular phenotypic characters which in turn alters assembly of *de novo* synthesized matrix elements. Tissue remodeling in a variety of patho/ physiological processes including embryogenesis,¹⁴⁹ normal tissue development, cancer,¹⁵⁰ and wound healing^{151, 152} has been evaluated. These studies implicate an array of molecules regulating the process which are regulated at transcriptional, translational and post-translation levels. Matrix metalloproteinases (MMP) form a degradative enzyme family with at least 20 members. MMPs mediate degradation of essentially all components of the ECM.¹⁵³ Loss of GAGs in arthritic patients has been attributed to the increased production of stromelysin (MMP-3).¹⁵⁴ Gelatin turnover is mediated either by MMP-2 (Gelatinase A), a constitutively produced homeostatic enzyme, or by MMP-9 (gelatinase B),¹⁵⁵ and upregulated in acute and chronic inflammations. MMP expressions are regulated by soluble mediators, presence of substrates, matrix elements,¹⁵⁶ and adhesive interactions.¹⁵⁷ In turn, MMPs influence rate of matrix synthesis. For example, cells exposed to hydrogels containing MMP-specific peptides show an increase in the transcriptional activity of collagen and proteoglycan synthesis.¹⁵⁸ In addition, $\alpha_v\beta_3$ can bind to MMP-2,¹⁵⁷ in an RGD-independent way, thereby localizing MMP-2-mediated matrix degradation to the endothelial cell surface.¹⁵⁹

2.8 Summary

In summary, there are a variety of natural matrices available for tissue engineering. Unfortunately, the heterogeneous nature of natural matrices (such as SIS) leads to inconsistent regeneration. One method to improve the consistency of regeneration is to fabricate a degradable porous matrix from polymers. It is important to factor the structural, biological, and degradation properties into the matrix.

Chapter 3:

Polymers and Polymer Composites

3.1 Polymers for Tissue Engineering

There are two main classes of polymers commonly used to create degradable porous matrices for tissue engineering applications, natural polymers and synthetic polymers. Natural polymers used for tissue regeneration typically have superior biological properties but lack mechanical strength¹⁶⁰, and synthetic polymers used for tissue regeneration typically have high mechanical properties but lack biological activity²².

3.1.1. Natural Polymers

Natural polymers tested as tissue scaffolds are derived from a variety of sources including fish scales, rat tails, and crab shells. Unlike synthetic polymers, natural polymers have superior biological properties. Scaffolds generated from natural polymers such as alginate^{80, 161, 162}, chitosan^{77, 163-168}, collagen²¹, glycosaminoglycans (GAGs) and elastin¹⁶⁹⁻¹⁷², gelatin^{5, 173, 174}, and fibrin¹⁷⁵⁻¹⁷⁷ have also been used as scaffolding materials¹⁷⁸⁻¹⁸⁰. A commonly used system is collagen/ GAGs^{181, 182}; collagen/ GAG based skin equivalents are already in clinical use^{170, 171} and under investigation for other applications such as heart valves, vascular grafts^{133, 183-187} and vascular networks¹⁸⁸. However, weak mechanical strength and inadequate tailorability in altering mechanical and degradation properties limit their usage. Porous scaffolds formed of natural

polymers have a modulus of only 2 kPa, compared to 3 MPa for naturally occurring matrices such as SIS.³

Chitosan is a polysaccharide derived from N-deacetylation of chitin, a polymer present in the outer shells of crustaceans⁷⁷. Chitosan is composed of β (1-4) linked 2-acetamido-2-deoxy-D-glucose and 2-amino-2-deoxy-D-glucose units. It is a semi-crystalline polymer, and the crystallinity is dependent on the degree of deacetylation. Chitosan is structurally analogous to GAGs, extra cellular matrix (ECM) elements present in the human body. Since GAGs have specific interactions with growth factors/proteins, chitosan may share similar activity. Chitosan is insoluble in water or organic solvents but soluble in aqueous acids (pH< 6.3). Due to the protonation of the free amine groups on the chain backbone, chitosan exhibits a high charge density in solution. This cationic nature and high charge density allow favorable interactions with negatively charged cells as well as antibacterial activity. Chitosan has been widely investigated in wound dressing and drug delivery systems⁴. The biocompatibility and biodegradability of chitosan makes it a promising material for tissue engineering¹⁸⁹. Chitosan has shown biological activity towards diverse cell types including stem cells⁵,¹⁹⁰, chondrocytes^{168, 190}, osteoblasts¹⁶⁸, hepatocytes^{191, 192}, and Schwann cells^{193, 194}. In addition, chitosan has minimal immune reaction and its stimulatory effect can induce local cell proliferation⁵. Chitosan can be degraded by lysozyme, a naturally occurring enzyme *in vivo*⁷⁷. The biodegradation time is determined by the amount of residual acetyl content, an easily controlled variable. Due to the active amino groups, chemical modification of chitosan can produce materials with a variety of physical and mechanical properties. Polysaccharide scaffolds were synthesized by crosslinking arabinogalactan,

dextran and amylose with chitosan to create a more cell compatible environment ¹⁹⁵. Chitosan is also blended with collagen, alginate, GAG, and synthetic polymers (i.e. PLGA, PCL) to fabricate suitable scaffolds ¹⁹⁶. The pH dependent solubility, the easy processability under mild conditions, the modification reactivity, the biodegradability, and biocompatibility make chitosan an excellent candidate for use as porous scaffolds in tissue engineering.

Hyaluronic acid (HA), a large linear GAG, is composed of repeating disaccharide of D-N-acetylglucos-amine- β -D-Glucuronic acid ¹⁹⁷. It is negatively charged, acts as a polyelectrolyte in solution, and acts as a lubricant ¹⁹⁸. Although HA is involved in mediating cell adhesion as an ECM component, its degradation rate is difficult to control ¹⁹⁹.

Collagens are a family of structural proteins reinforcing a variety of animal tissues including skin, bone, and tendon. Collagen contains cellular-binding domains and has been extensively used in vascular tissue engineering. Collagen has a triple helical structure of three polypeptide chains glycine, proline and hydroxyproline. Based on the amino acid sequences, collagen is of different types (over 28 different types have been identified) ²⁰⁰. Type I collagen is a major component of most connective tissues, is present in the arterial wall ²⁰¹ and small intestinal submucosa (SIS) ³¹, and is degraded by several matrix metalloproteases (MMPs) ²⁰². It is tough and inextensible, with great tensile strength and controls cell shape and differentiation. Type II collagen is the primary component of hyaline articular cartilage ²⁰³ and is used as a marker for chondrocyte differentiation ²⁰⁴.

Gelatin, a partially denatured derivative of collagen, has also been used to generate scaffolds⁵. Gelatin is widely found in nature, and can be extracted from collagen found in fish, bovine bone, and porcine skin. Gelatin blended with chitosan has been used in artificial skin and cartilage applications due to the ability to form a polyelectrolyte complex^{172, 205}. Gelatin is a thermally denatured form of collagen and is isolated from animal skin and bones. Gelatin is primarily used as a gelling agent as it forms thermoelastic gels upon cooling to below 35°C, which dissolve at low temperature. Gelatin contains Arginine-Glycine-Aspartic acid (RGD)-like amino acid sequence that promotes cell adhesion and migration. The physicochemical properties of gelatin can be suitably modulated due to the existence of both carboxylic acid and amine functional groups²⁰⁶. Both the mechanical and degradation properties of gelatin can be modified by crosslinking. Gelatin can be crosslinked using another molecule to connect the gelatin functional groups, for example glutaraldehyde^{207, 208}. The gelatin functional groups can also be directly linked to each other without adding another molecule to the chemical structure (zero length crosslinking) using carbodiimides²⁰⁹.

Fibrin has been used for cartilage repair²¹⁰. Upon injury, fibrinogen self-assembles to become 3D fibrin hydrogel¹⁹⁹. Fibrin can bind to different integrin receptors to regulate cytokine gene expression as well as regulate inflammation. Since fibrinogen can be obtained from the patient's own blood, use of fibrin minimizes immunogenic concerns. Another advantage of fibrin is that it can be degraded by cell-associated enzymatic system. Despite these advantages, fibrin scaffolds failed to keep their shape integrity. Fibrin gels showed significant reduction in size after *in vitro* incubation and weak compression modulus²¹¹, suggesting a need for further modifications.

3.1.2. Synthetic Polyesters

Synthetic polyesters such as poly (lactic acid) (PLA), poly (glycolic acid) (PGA), their copolymers (PLGA, PLLA, etc)^{6-12, 23, 62, 107}, and poly (caprolactone) (PCL)^{212, 213} have generated immense interest as tissue engineering materials due to their strong FDA approval history and numerous investigations in a variety of biological applications for more than three decades¹³. These polymers degrade by hydrolysis, and their degradation rates and mechanical properties can be altered via co- and graft-polymerization techniques^{192, 214, 215}, and by processing conditions²¹⁶⁻²¹⁹. Synthetic Polymers have been extensively reviewed in the literature^{22, 201, 220}

PGA is a rigid thermoplastic material with high crystallinity and is hydrophilic¹⁹⁹. PLA is more hydrophobic than PGA due to an extra methyl group in the lactide molecule. Because lactic acid is a chiral molecule, PLA has D-PLA, L-PLA, and racemic stereoisomeric forms. Of the two isomers L-PLA is more frequently used in tissue engineering because it possesses high mechanical strength²⁰¹. Poly (lactic-co-glycolic acid) (PLGA) is the copolymer of glycolic acid and lactic acid. Various ratios (75 PLA:25 PGA, 50:50, etc) of PLGA have been investigated. Amorphous 50:50 PLGA (50% lactic acid, 50% glycolic acid) is preferred for various tissue engineering applications because it degrades faster than other co-polymer ratios, which are semi-crystalline. The degradation of PLGA is via random hydrolysis of the ester bonds. In addition, the degradation rate can be modified by changing the copolymer ratio and molecular weight (lower molecular weights degrade faster)²².

Poly (caprolactone) (PCL) is a non-toxic, biocompatible aliphatic polyester²² with a melting point of only 60°C¹¹⁰. PCL can be readily dissolved in acetic acid and

structures can be formed by several techniques²²¹. PCL has a degradation time dependent on its molecular weight²²². High molecular weight degradation times are of the order of two to three years make which it unsuitable for short term implants. PCL is a chemosynthetic polymer poly (ϵ -caprolactone) (PCL), due to its high degradation rate relative to chitosan, better tensile properties, low melting point (60°C) which allows easy processing, and lack of charge contribution to the system¹¹⁰. PCL films formed after dissolving in chloroform have shown elongation up to 1000% before break²²³. PCL has limited bioregulatory activity and hydrophobic, neutral charge contribution, and susceptible to bacteria-mediated degradation. PCL dissolves in chloroform and other organic solvents but not in water but chitosan dissolves in acidic water and not in many organic solvents. Thus, solvent annealing of the formed blends is also possible apart from thermal annealing.

Poly (ethylene glycol) (PEG) is a biocompatible polymer with a high solubility in water. However, PEG is not hydrolytically degraded, unlike other synthetic polymers commonly used in tissue engineering. PEG chains under 50 kDa can be completely eliminated from the body²²⁴. Therefore PEG is typically used in combination with degradable crosslinks such as PLA²²⁵. The highly soluble nature of PEG makes it an ideal material for hydrogels²²⁴ or for increasing the solubility of other molecules. Because it does not degrade hydrolytically it has been used as a barrier material to encapsulate and protect the cells destroyed in a diabetic patient (Islets of Langerhans)²²⁶.

Synthetic polymers show poor regulation of cellular activity²²⁷. Furthermore, their degradation products are relatively strong acids and cause inflammation²²⁸. The scaffolds also show structural instability due to massive swelling during degradation²¹⁸.

Apart from adhesive interactions, a substrate has to mediate a variety of signals such as growth factor activity to regulate the biological response of diverse cell types. Despite significant efforts to improve these limitations via co-polymerization²²⁹ and grafting arginine-glycine-aspartate (RGD) peptides (necessary for cellular attachment)²³⁰, recreating all the biological responses may not be possible without incorporating controlled delivery systems into the porous structure.

3.2 Combining Natural and Synthetic Polymers

Currently there is not a synthetic material that provides all the essential properties present in natural matrices, such as SIS (**Table 1**). While natural polymers have the benefits of facilitating cell adhesion and repopulation by providing critical signals, they lack tailorability of mechanical properties. In contrast, synthetic materials possess advantages of easy control of microstructure, strength and degradation rate, but they lack the attachment domains and cellular signals that direct cell growth, proliferation, and differentiation²⁰¹. Therefore, one current area of research in combinations of natural and synthetic polymers in order to exploit the benefits of each polymer while minimizing the weaknesses. There are two approaches generating synthetic matrices for tissue engineering materials.

- a) Synthesize novel materials with different functional groups
- b) Combine the existing materials in different modes.

Table 1. Summary of polymer properties

	Natural Matrices (SIS) ³	Natural Polymers (Chitosan) ⁷⁷	Synthetic Polymers (PLGA) ¹⁶
Mechanical Strength	3 MPa	2 – 6 kPa	1 – 9 MPa
Degradation Time	4 weeks	6 – 12 months	4 weeks
Cellular Support	Yes	Yes	No

The focus of this work focuses on combining natural and synthetic polymers using SIS as a design basis. Several methods are being examined including coating, copolymerization, blending, and forming composite structures.

3.2.1. Multiphase Polymer Architecture

Several different 3D porous architectures are possible when combining dissimilar polymers. A combined polymer scaffold's properties are influenced by the 3D partitioning of the polymer phases present in the matrix. For example, one reason that freeze dried PLGA-chitosan emulsions have less mechanical strength than scaffolds formed from pure chitosan is that the two polymer phases formed within the emulsified scaffolds do not support each other mechanically as well as the single phase in the chitosan scaffold²³¹. The polymer phases within a 3D porous structure may be distributed in a variety of ways, and as either continuous or dispersed phases.

3.2.2. Coatings

The simplest method for combining separate polymers involves utilizing them to coat other materials. PGA matrices have been coated with PLGA in order to stabilize and increase their mechanical strength²³². Polyurethane has been coated with collagen in order to improve its biological functionality²³³. Additionally, chitosan has been used as a bioactive coating for a variety of materials from PLA²³⁴ to stainless steel²³⁵. Chitosan coatings have even been used on food products because of chitosan's antibacterial properties²³⁶.

3.2.3. Copolymerization

Several techniques used to improve the performance of tissue engineering devices revolve around using copolymerization. A multitude of copolymerization strategies have been used in tissue engineering applications. There are two basic strategies for copolymerization, modifying the surface of a polymer structure or forming multiple block monomers and then polymerizing the whole matrix. For surface modification, the underlying polymer fibers are formed and then a surface layer of the new polymer is created on top of the base polymer material. For example chitosan and collagen have been grafted to PET fibers, and the modified fibers improved fibroblast proliferation²³⁷. Additionally, biologically active compounds (proteins, peptides, DNA, etc) can be grafted onto polymers to improve their bioactivity. A variety of peptides containing cellular binding domains (such as RGD) have been grafted onto polymer structures²³⁸.

For block copolymerization, the copolymer is formed in homogeneous solution and then formed into the final scaffold using standard processing techniques such as film formation²³⁹, photopolymerization²⁴⁰, self assembly into nanoparticles²⁴¹, or

electrospinning²⁴². These blocks can be as simple as grafting chitosan to PCL²⁴¹, and grafting chitosan to sugars and GAGs (such as lactose and heparin) has been shown to increase extracellular matrix production in *in vitro* cartilage tissue engineering²³⁹. The individual copolymer blocks can also be synthesized in complicated nested blocks. For example Bramfeldt et al synthesized P(CL-co-DLLA)-PEG-P(CL-co-DLLA) block copolymers for tissue engineering applications. This polymer contains a copolymer of PCL and PLA with a PEG block linking the copolymer sections²⁴³.

Additionally, copolymerization has been used to synthesize a variety of temperature sensitive polymers or use as drug delivery vehicles. Several examples use chitosan as a backbone and then chemically attach another polymer to provide temperature sensitivity. Both (N,N-dimethylamino)ethyl methacrylate²⁴⁴ and PEG²⁴⁵ have been grafted onto the chitosan backbone in order to create temperature sensitive polymers for drug release. Additionally, comblike structures have been created using chitosan as a backbone and temperature sensitive polymers, such as poly(N-isopropylacrylamide), as the extensions to fabricate temperature sensitive hydrogels²⁴⁶.

3.2.4. Blending

Another common method of combining natural and synthetic polymers is to physically blend them without forming chemical bonds. A key aspect in blending is finding a common solvent for the polymer system. The polymers are dissolved and then processed into porous structure as a homogeneous phase. One common system for blending is chitosan and chitin with PCL²⁴⁷. Chitosan and PCL have been blended using acetic acid and water as a common solvent followed by freeze drying, and then analyzed for increased mechanical properties, adhesion and proliferation of fibroblasts, and anti-

bacterial activity^{111, 248}. PCL and chitosan have also been blended and formed into porous matrices using phase separation²⁴⁹. Chitosan and PGA have been blended using acetic acid and dimethyl sulfoxide (DMSO) as solvents, freezing the blend, and then neutralizing the frozed scaffold with NaOH to precipitate out the 3D porous structure²⁵⁰. PLGA and chitosan have been blended using a novel solvent and wet spun into fibrous mats. These matrices were tested for improved properties including mechanical strength, water uptake, degradation, chondrocyte viability, and GAG production²⁵¹. Melt blending is another technique that can be used to combine chitosan with a number of synthetic polyesters including PLGA. However, the melt blending process forms nonporous blocks which must be further processed into porous structures suitable for tissue engineering²⁵². Additionally, homogeneous blends of chitosan and PLGA can also be fabricated into 3D porous structures by using solvent extraction to create a homogeneously blended gel and then freeze dried to create a porous structure²⁵³.

When a common solvent for cannot be found an emulsification system may be used. The emulsifier effectively binds the heterogeneous phases together as a collection of microscopic droplets which do not revert back into two separate phases. For example one method for combining PLGA and chitosan uses an emulsification system because no simple solvent will dissolve both chitosan and PLGA²³¹. Freeze dried scaffolds have been synthesized from the emulsions of the chitosan and PLGA. The emulsified scaffolds showed minimal smooth muscle cell spreading and proliferation, but their major problem was lack of physical strength²³¹. Recently, it was shown that the observed difference in these emulsions is due to structural weakness in the matrix and minimal electrostatic cell adhesion to chitosan⁵. The lack of mechanical strength is a result of

dispersed polymer phases in the material. The freeze dried product is formed from two separate polymer phases because the emulsion is a two phase mixture. The PLGA phase cannot provide structural reinforcement because it lacks a continuous phase capable of carrying the mechanical load ²³¹.

3.2.5. Composites

Several strategies have been used to combine natural and synthetic polymers including blending, emulsifying, and coating. However, these methods suffer from an inability to separately optimize the physical and biological properties of the scaffold. An alternative to uniformly blending natural and synthetic polymers is to form composite matrices. Several composite systems have been developed. Some examples of how multiple polymers can be combined using a composite structure: filling the pores in a 3D matrix, fabricating interlocked layered structures, or embedding nanoparticles within the porous matrix.

One method for creating multiplier composites is to fill the pore spaces in a 3D matrix with another material. For example collagen microsponges have been fabricated within a porous PLGA backbone ²⁵⁴. Additionally a 3D composite has been by filling the pore spaces with agar or gelatin ²⁵⁵.

Another method uses composites based on a multiple layer structure. For example a composite structure of consisting of chitosan and silicon layers has been used as a dermal equivalent for wound healing and burn injuries ²⁵⁶. This work explored the generation of a composite matrix to mimic the mechanical properties of distal SIS²⁵⁷. A three layered composite structure is employed in order to independently control the mechanical and biological properties of the scaffold. The composite matrix consists of

two 3-D chitosan layers reinforced with a PLGA membrane. The outer layers of porous chitosan provide a 3D natural polymer structure scaffolding for multi-layered cell growth, and the inner PLGA layer provides mechanical strength through a continuous synthetic polymer phase¹⁶.

3.3. Materials and Methods.

3.3.1. Sources for Material.

Chitosan with >310 kDa M_w and 85% degree of deacetylation, urea, Dulbecco's modified Eagle medium (DMEM), lysozyme, glucose, sodium bicarbonate, Medium 199 (M199), HEPES, bacteriologic peptone, sodium chloride, resazurin, and tetrahydrofuran (THF) were obtained from Sigma Aldrich Chemical Co (St. Louis, MO). Nineteen kilo-Dalton 50:50 PLGA was obtained from Alkermes Inc., (Cambridge, MA) while 75kD and 160kD 50:50 PLGA were purchased from Birmingham Polymers (Birmingham, AL). A urea assay kit was obtained from Diagnostic Chemicals Limited (Oxford, CT). Alexa Fluor 488 phalloidin was from Molecular Probes (Eugene, OR). Mouse embryonic fibroblasts (referred to as STO cell line) were purchased from American Tissue Culture Collection (Walkersville, MD). L-glutamine, penicillin-streptomycin, amphotericin, trypsin/EDTA, MEM vitamins, MEM Amino Acids, propidium iodide, and Fetal Bovine Serum (FBS) were purchased from Invitrogen Corp. (Carlsbad, CA). MMP2/MMP9 fluorogenic peptide (DNP-Pro-Leu-Gly-Met-Trp-Ser-Srg-OH) was purchased from CalBiotech (Spring Valley, CA). Bicinchoninic acid (BCA) protein assay kit was purchased from Pierce Protein Research Products (Rockford, IL).

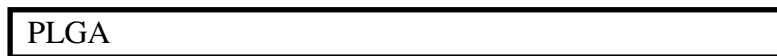
3.3.2. Composite Layered Scaffold Fabrication.

The composite scaffold was fabricated using a custom Teflon/silicon well system developed in house. Procedure used in generating the composite structure is shown in **Figure 8**. First, a 1/32" thick Teflon sheet (United States Plastic Corp, Lima, OH) was affixed to a flat aluminum plate using silicon glue. Teflon was used to provide a nonstick surface for the PLGA and the aluminum provided physical support to keep the Teflon flat. A 6 cm × 8 cm well was formed on the Teflon sheet using silicon glue (Silicone II, GE Sealants and Adhesives, Huntsville, NC) (**Figure 9A**). Five milliliters of 4% (wt/v) PLGA solution, prepared in chloroform, was poured into the well and air dried in a chemical hood overnight. The silicon was trimmed away and the PLGA film was perforated with a custom punching apparatus, developed in house. The puncher consisted of a Teflon grid marked in a 1 cm × 1 cm pattern. The PLGA film was placed on the grid and perforations were made using stainless steel nails (**Figure 9B**). At this point perforation size was analyzed by light microscopy, using the technique described in the thickness characterization section below. The perforated film was placed on a new Teflon sheet and a well was formed using silicon glue. The membrane was layered with 10 mL of 0.5% (wt/v) chitosan solution with 0.7% (v/v) acetic acid, frozen at -80°C, and lyophilized overnight. The silicon was removed, then the sample was flipped, and a new silicon well was formed. The well was filled with ten milliliter of chitosan solution, frozen at -80°C and lyophilized overnight. The silicon was removed and the samples were stored in a vacuum desiccator. Before any subsequent use, the composite membranes were neutralized in ethanol and washed with phosphate buffered saline (PBS). At each step of the process, samples were analyzed with a scanning electron

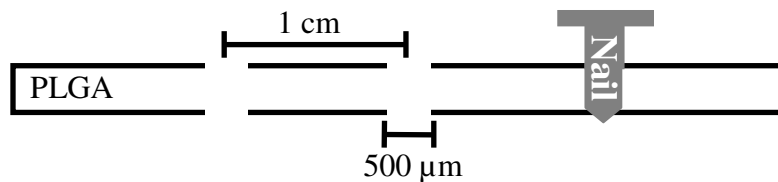
microscope (SEM) to ensure the 3D structural design elements were incorporated into the final scaffold. SEM images were colorized using Paint Shop Pro (Corel Corporation, Minneapolis, MN).

Step 1. Dissolve PLGA in chloroform

Step 2. Form PLGA layer by air drying



Step 3. Perforate PLGA layer with nails



Step 4. Form chitosan matrix on one side



Step 5. Form chitosan matrix on the other side

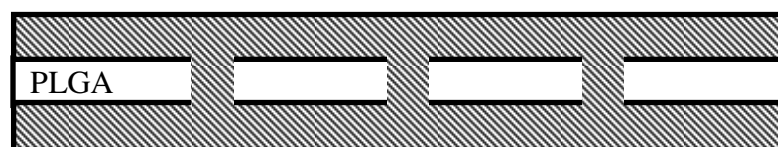


Figure 8. Schematic showing the steps involved in forming the composite scaffold

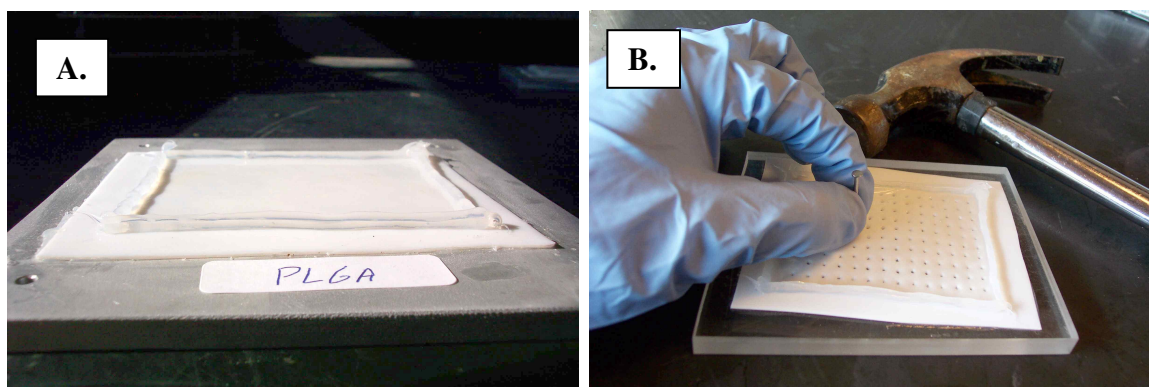


Figure 9. Construction of the Composite Scaffold

Panel A. Silicon glue is used to create a well for solvent casting. Panel B. The custom punching apparatus used to create perforations in the PLGA films

3.3.3. Thickness Characterization.

PLGA films, 75kDa and 160 kDa MW, were cast in Teflon/silicon wells as described above. However, PLGA films with 19 kDa MW were formed in Teflon petri dishes because they leaked out of the silicon wells. The thickness of the polymer membranes was measured optically because the polymers are too soft to be reliably measured with a micrometer caliper. All membranes were cut into small (~2 mm wide) strips, and oriented orthogonal to the plane of view of an inverted microscope so that the cross section could be viewed. Digital micrographs of the cross section were recorded using a CCD camera. The cross sections were measured using Sigma Scan Pro software (Systat Software, Inc., Point Richmond, CA) which was calibrated using an image of a hemacytometer. For each sample, thicknesses were measured at forty or more locations and average values were used in all calculations.

3.3.4. Uniaxial Tensile Testing.

Tensile properties of the matrices were measured by the method described previously^{3, 110}. In brief, 6 cm × 1 cm strips were cut from each sample and analyzed using an INSTRON 5842 (INSTRON Inc., Canton, MA) with a constant crosshead speed of 10 mm/min. Tests were performed at room temperature under hydrated conditions using a custom designed chamber.

3.3.5. Microarchitecture Analysis.

To evaluate the microarchitecture of the matrices, samples were analyzed using a scanning electron microscope (JOEL scanning microscope, Peabody, MA). For this purpose, samples were dehydrated using a series of increasing concentrations of ethanol followed by a brief vacuum drying. Samples were sputter coated with gold at 40 mA prior to observing under SEM.

3.3.6. Permeability Measurement.

Permeability of urea was measured using the method described by Raghavan et al³. The urea assay was used because urea is a small molecule that is biologically important. This method utilizes a custom designed chamber shown in **Figure 10**. In brief, one side of the permeability chamber (chamber 1) was filled with 4 mL of 550 mM urea in PBS. The 550 mM urea concentration is the average concentration found in a human bladder. A 2.5 cm × 2.5 cm section of the composite was placed on top of the solution, and the chamber was assembled. The other side of the sample (chamber 2) was filled with 4mL PBS using a syringe through the sample port. The chamber was maintained at 37°C. At regular intervals, nearly 100 µL samples were taken for 8 hours.

The concentration of urea was determined using a commercially available kit (Diagnostic Chemicals Limited, Oxford, CT) following the vendor's protocols. In brief, 20 μL of sample was added to 2 mL of urease solution and the rate of change in absorption, at 340 nm, was measured for 90 s. The concentration of urea was determined using a calibration curve prepared between 0 to 275 mM urea.

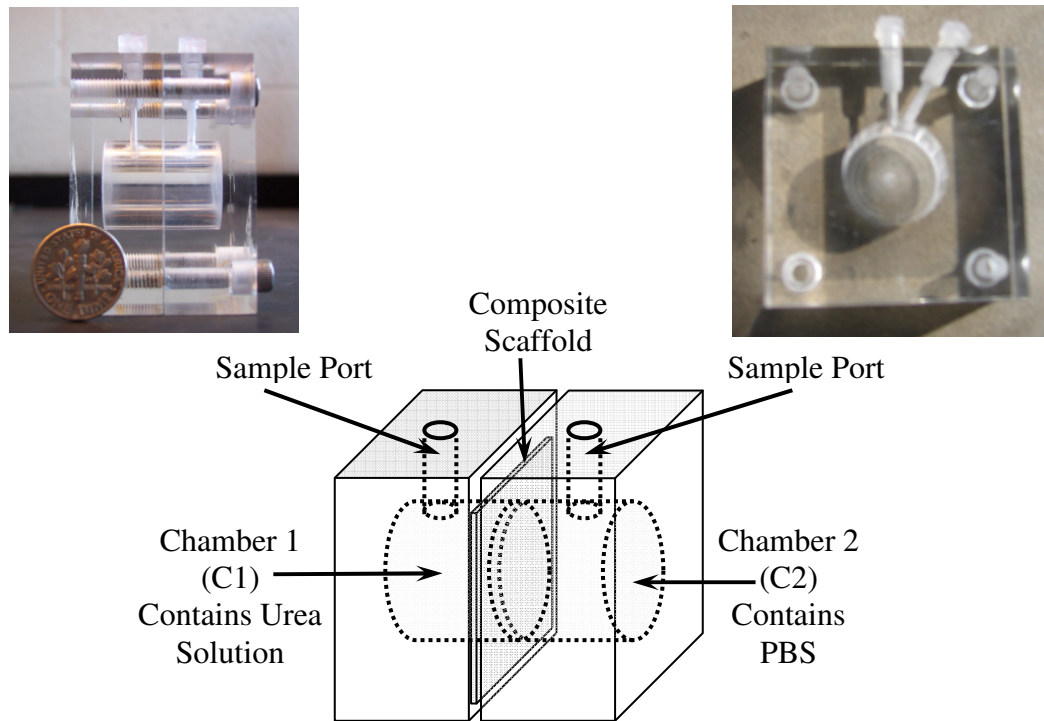


Figure 10. Diagram of the Chamber used in Permeability Experiments

3.3.7. Degradation Characterization.

To understand the influence of composite formation, degradation studies were performed using the method described by Moshfeghian *et al* with minor modification²³¹. In brief, samples were cut into 1 cm \times 1 cm strips, neutralized and sterilized with ethanol, rinsed twice with sterile PBS, placed into sterile individual 20mL scintillation vials, and incubated at 37°C in 10 mL sterile PBS containing 10 mg/L lysozyme. The lysozyme

containing PBS solution was changed every 7 days and the pH of the spent PBS was measured. Four matrices per group were sacrificed at 1, 7, 15, 23, 28, 35, 42, 49, and 56 days and weighed. For weight determination, samples were dehydrated using an increasing concentration of ethanol (0, 25, 50, 80, and 100%) and briefly vacuum dried. Some of the samples were then examined by SEM to evaluate changes in the microarchitecture as described before.

The molecular weight of PLGA present in the samples from 0, 23, 35, and 49 days was measured using gel permeation chromatography (GPC), Agilent 1100 series (Santa Clara, CA), and associated software Chemstation. In brief, samples from degradation study were dissolved in tetrahydrofuran (THF) at a concentration of 5mg/mL. Only PLGA dissolved in THF and not chitosan. This was confirmed by dissolving pure chitosan and pure PLGA in THF and analyzing in GPC. The samples were filtered through a 0.2µm filter to remove any particulates. They were injected into the GPC column (Polymer Laboratories, Amherst, MA), and then eluted at 30 bar and 40°C using a 1 mL/min flowrate. Additionally the column was calibrated using two polystyrene standards, one with 600 kDa, 100 kDa, and 9 kDa molecular weights and another with 390 kDa, 17 kDa, and 0.8 kDa molecular weights.

3.3.8. Cell Culture.

Mouse embryonic fibroblasts (MEFs), from American Tissue Culture Collection (Walkersville, MD), were maintained in Dulbecco's modified Eagle's medium (DMEM) supplemented with 4 mM glutamine, 4.5 g/L glucose, 1.5 g/L sodium bicarbonate, 100 U/mL penicillin-streptomycin, 2.5 mg/mL amphotericin B, and 10% fetal bovine serum (FBS). Cells were maintained at 37°C, in a 5% CO₂/95% air and fed with fresh medium

every 48 h. Cells were dissociated with 0.01% trypsin / 10 mM EDTA, centrifuged, and resuspended in medium prior to cell seeding.

Canine bladder smooth muscle cells (SMC), a kind gift from Dr. Bradley Kropp, Department of Urology, University of Oklahoma Health Science Center (Oklahoma City, OK) were maintained in Medium 199 (M199) supplemented with 1g/L glucose, 2.2 g/L sodium bicarbonate, 3.56 g/L Hepes, 0.5g/L bacteriologic peptone, 100 U/mL penicillin-streptomycin, 2.5 mg/mL amphotericin B, 1% MEM vitamins, 1% MEM amino acids, and 10% FBS. Cells were maintained at 37°C, in a 5% CO₂/95% air and fed with fresh medium every 48 h. Cells were dissociated with 0.01% trypsin / 10 mM EDTA, centrifuged, and resuspended in medium prior to cell seeding.

3.3.9. Cell Colonization.

Cell colonization and activity were evaluated on tissue culture plastic (TCP), 2-D PLGA films, and 3-D composite scaffolds. For both fibroblast and SMC experiments the samples prepared as described above, were cut into circular pieces, sterilized with ethanol, rinsed twice with PBS, and inserted into 24-well cell culture plates. Cell growth media was added to the wells prior to seeding 30,000 cells per sample. After three days, cell spreading and attachment was examined using SEM and actin staining ²⁵⁸. In brief, cell-containing scaffolds were fixed in 3.7% formaldehyde for 15 min at room temperature. Cells were washed with PBS and permeabilized with -20°C ethanol for 30 min at -4°C, and then incubated with Alexa Fluor 488 phalloidin for 1 h at room temperature in the dark. SMCs were also stained for DNA by incubating with 1mg/mL propidium iodide for 30 minutes and washing four to five times. Cell morphologies were examined using an inverted fluorescence microscope (Nikon TE2000, Melville, NY).

Some matrices were dehydrated using a series of increasing concentration of ethanol and analyzed via SEM, similar to microarchitecture analysis described above.

3.3.10. Cellular Activity.

Fibroblast cellular activity was examined using a functional assay for matrix metalloprotease 2 (MMP-2) and matrix metalloprotease 9 (MMP-9)²⁵⁹. In brief, 100µL of cell supernatant was incubated with 100µl of a 100 µM solution of fluorogenic peptide specific for MMP-2/MMP-9 (DNP-Pro-Leu-Gly-Met-Trp-Ser-Srg-OH). After 20min at room temperature fluorescence measurements were taken at 320 nm excitation and 405 nm emission. The amount of fluorescence was then normalized using the total protein content of the samples (measured using a commercially available BCA total protein assay). Cell viability was measured using the method described in Larson *et al*²⁶⁰. In brief cells were incubated in 0.1% resazurin solution for three hours then the absorbance of the supernatant was measured at 540nm. Growth medium incubated without any cells served as control.

3.3.11. Statistical Analysis.

All experiments were repeated three or more times with triplicate samples. Statistical analysis was preformed using analysis of variance (ANOVA) and difference among the means was considered significant when $p < 0.05$.

3.4. Results.

3.4.1. Composite Scaffold Physical Properties.

A major challenge in generating the composite scaffolds was attaching the hydrophobic PLGA layer to the hydrophilic chitosan layer. Therefore a mechanically interlocked composite scaffold was formed in three layers. The interlocking was created by perforating the PLGA layer and having the chitosan compartment run continuously through the perforations. Using this concept, thin PLGA membranes (thickness of $50 (\pm 16)\mu\text{m}$) were generated and perforated using stainless-steel nails. The PLGA perforations were rectangular with sides between $300\mu\text{m}$ and $550\mu\text{m}$ long (**Figure 11A**). The perforation size was determined by the size of the nail used. After the addition of one chitosan layer, the porous chitosan structure was visible through a perforation in the PLGA layer (**Figure 11B**). This shows that there was good contact between the layers. After the addition of second layer of porous chitosan, micrographs showed that the chitosan forms a continuous layer through the perforations (**Figure 11C**). The dry thickness of these composite scaffolds was roughly 2mm and the PLGA membrane contributed only fifty micrometers. Hence, large thickness was a result of the chitosan 3-D structures. No separation of layers occurred when the samples were neutralized with ethanol and hydrated in PBS, suggesting that the composite was firmly anchored at the perforations.

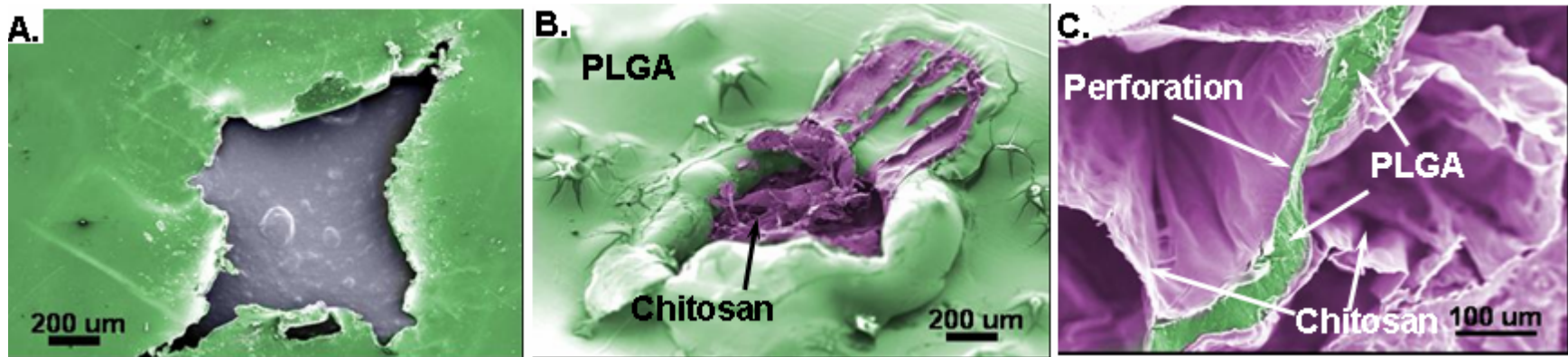


Figure 11. Composite Scaffold Structure during Fabrication.

Scanning electron micrograph of (A) a perforation made in the PLGA film, (B) a perforation in the 2 layer Chitosan-PLGA structure, and (C) the composite structure showing the continuity of the porous chitosan layer through a perforation in the PLGA

3.4.2. Tensile Properties.

First, influence of MW of PLGA on the tensile properties was characterized in hydrated conditions (**Figure 12A**). The Teflon-silicon well system was developed in-house because the standard Teflon Petri dishes have an uneven surface that results in a film with variable thickness. PLGA films with 75 and 160 kDa M_w s were formed in custom silicon wells, however 19 kDa PLGA solution leaked out of the silicon wells and had to be cast in Teflon Petri dishes. As expected, tensile strength increased with increasing M_w . These results showed that 160 kDa membranes to possess tensile strength values greater than SIS. Hence, 160 kDa PLGA membranes were used in all subsequent analyses.

To understand the effect of various fabrication steps on the mechanical properties of PLGA, stress calculations were based only on the thickness of the PLGA films (~ 50 μ m) for all materials. The PLGA membranes retained their mechanical strength within the composite scaffold, and remained mechanically unaltered under tensile loading. Repeated freeze-drying did not affect the tensile properties of PLGA (**Figure 12B**). The stress strain curves were non-linear, and the composite structure stretched more than SIS before failure. The composite structure had a break stress between 3.5 and 5 MPa which is comparable to the tensile stress of distal SIS (3MPa). The modulus of elasticity in the initial linear range ($<15\%$ strain) for the composite structure was 45 ± 11 KPa, and the modulus of elasticity for 160 kDa PLGA films was 250 ± 41 kPa. The chitosan layers broke in a tiled pattern (on both sides of the membrane), and the chitosan tiles remained attached to the PLGA at the site of the perforations (**Figure 12B, Inset**). The stress strain curve for the composite also showed that point where the chitosan layer failed. The small

decrease caused by the chitosan failure (**Figure 12B**) shows that the majority of the composite scaffold's mechanical strength came from the PLGA layer.

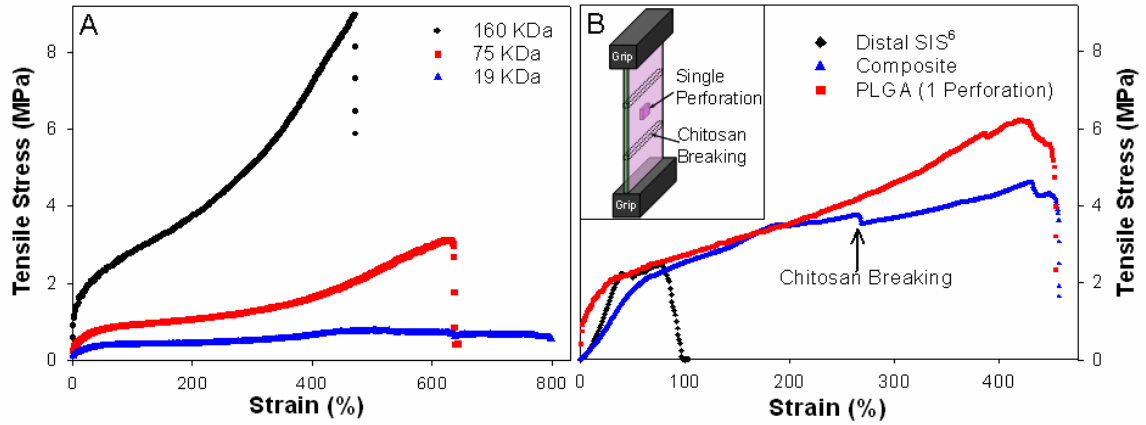


Figure 12. Stress Strain Characteristics.

A) Effect of MW of PLGA. B) Behavior of the Composite. Inset is a schematic showing composite with a single perforation and chitosan break pattern.

3.4.3. Permeability to Urea.

Next, the effect of perforations on the permeability of urea was examined to reaffirm that the perforations were filled with chitosan. If the scaffold is mechanically interlocked through the perforations, then the interlocks should create a barrier to diffusion. This barrier will lower prevent transport of urea and lower the permeability drastically. First, the permeability of unperforated PLGA membranes was tested for 48 hr, showing negligible presence of urea in the opposite compartment. Next the composite's permeability was tested. These results showed that the composite scaffold was much less permeable to urea than SIS (**Figure 13**). After eight hours, the final concentration of urea that had diffused through the composite was 80 mM while urea diffusing SIS reached that concentration less than 30 minutes. Additionally, the 80 mM final concentration was only 30% of the expected equilibrium concentration of 275 mM,

and after 8 hours the concentration of urea in chamber 1 (the initial loading side) was significantly higher. The lack of permeability shows that the chitosan layer was blocking the perforations, preventing urea transport.

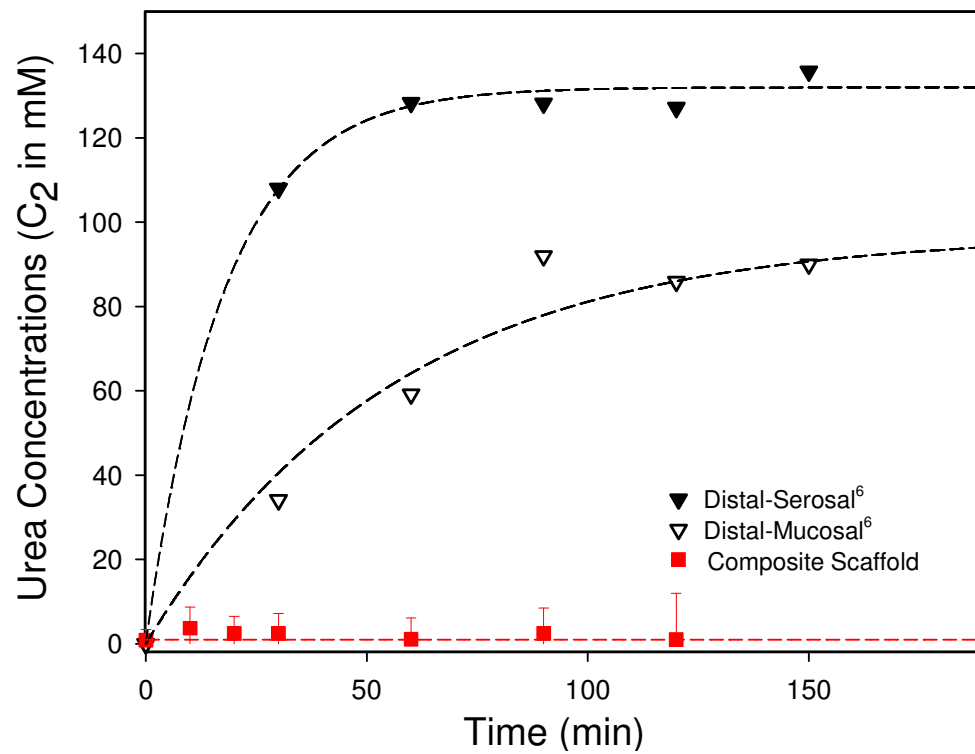


Figure 13. Diffusion of Urea across Composite Membrane.

3.4.4. Scaffold Degradation Characteristics.

In order to understand the utility of composite scaffolds, it was necessary to evaluate their degradation characteristics. For this purpose, samples were incubated in PBS containing 10mg/mL lysozyme. These results showed no significant changes in the width and length of the scaffolds. However, the scaffolds gradually lost their structural integrity and could no longer be handled with forceps at week 8. Of the 5 samples stopped at week eight, only two were successfully removed from the vials and weighed. Further, no significant changes were observed in the overall superstructure of the scaffolds over 4 weeks (**Figure 14**). Both the layered and porous elements of the scaffold were maintained over the full eight weeks, showing that the layers remained mechanically interlocked as the sample degraded. However, the chitosan layer developed a fluffy texture and the PLGA turned white as the degradation progressed. The mass loss data showed a slow decline to 80% of the starting mass in week 5 then a jump to 50% of the starting mass by week 8 (**Figure 15A**).

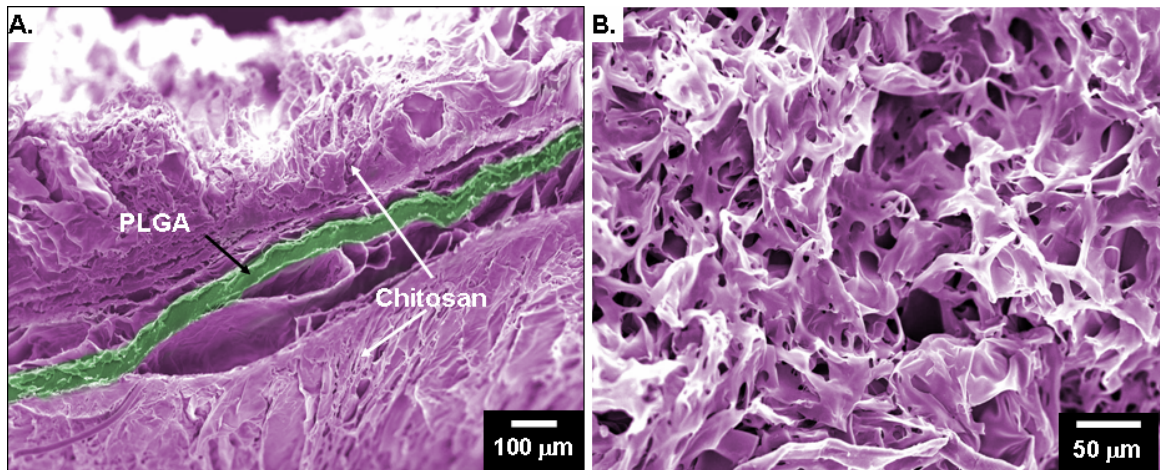


Figure 14. Composite Membranes Retain their 3D Structure during Degradation.
(A) Cross Sectional View of the Composite Membrane after 21 days in PBS, and (B) Top View of the Composite Membrane after 21 days in PBS.

To better understand scaffold degradation characteristics, the M_w and M_n of PLGA were measured using GPC. These results showed a continuous linear decrease in both M_w and M_n . The M_w reduced by 50% after 3 weeks and by 80% after 7 weeks (**Figure 15B**). The slope of M_w/M_n (polydispersity index) of the samples remained constant at 1.64 for all 7 weeks. The large drop in scaffold weight from week 5 – week 7 could be attributed to the decreasing M_w of PLGA. PLGA molecules could not disentangle themselves from the bulk polymer until their M_w was reduced. As shown in **Figure 12A**, a drop in M_w of PLGA to 19 kDa caused a significant drop in mechanical strength. The loss of mechanical strength leads directly to the loss of structural stability seen in **Figure 15A**. This further emphasizes that the composite's mechanical properties are directly controlled by the PLGA layer.

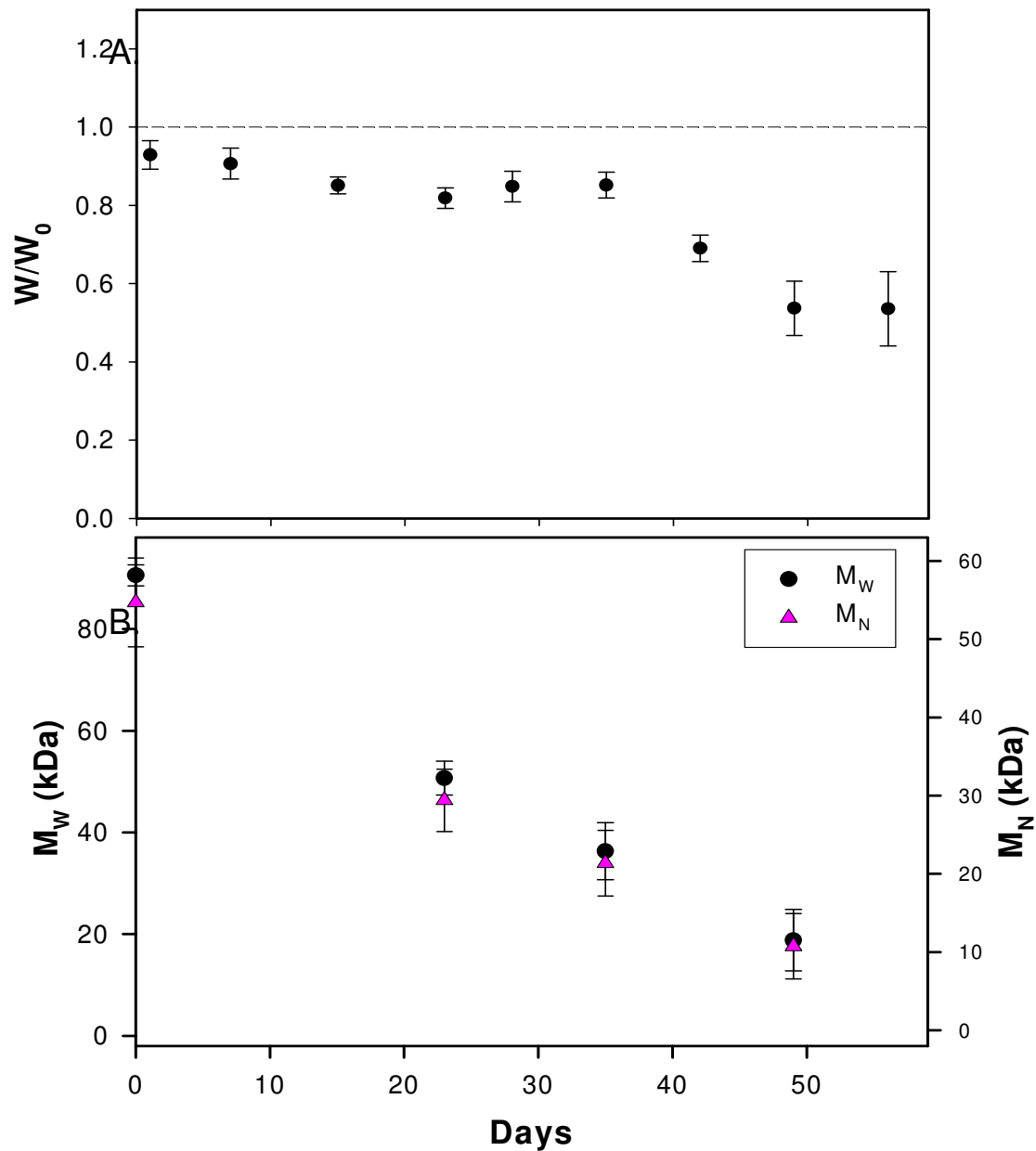


Figure 15. Degradation Characteristics of the Composite.

(A) Weight Loss. (B) Changes in PLGA molecular weight (MW) and molecular number (Mn).

3.4.5. Support for Cellular Activity.

Cell morphologies were evaluated to understand whether composite matrices support cell colonization. Cytoskeletal organization of MEFs was probed via actin staining. These results showed that PLGA films alone altered the shape of the cells relative to tissue culture plastic surface and the typical spindle shape of fibroblasts was not observed. However, on 3-D composite matrices, MEFs showed well spread spindle shape, similar to previous publications (**Figure 16A - C**)^{5, 14}. In addition, cellular attachment mimicked the pore morphologies of the scaffold showing that cell spreading and adhesion appeared to be guided by the porous structure. MEFs showed peripheral distribution of actin filaments, similar to cells on tissue culture plastic surface. Further analysis by SEM confirmed (**Figure 16D-E**) that cells on the PLGA films had reduced spreading. On the contrary, the cells on all 3-D composite matrices exhibited their typical elongated shapes. In addition, extensions resembling lamellapodia were also observed.

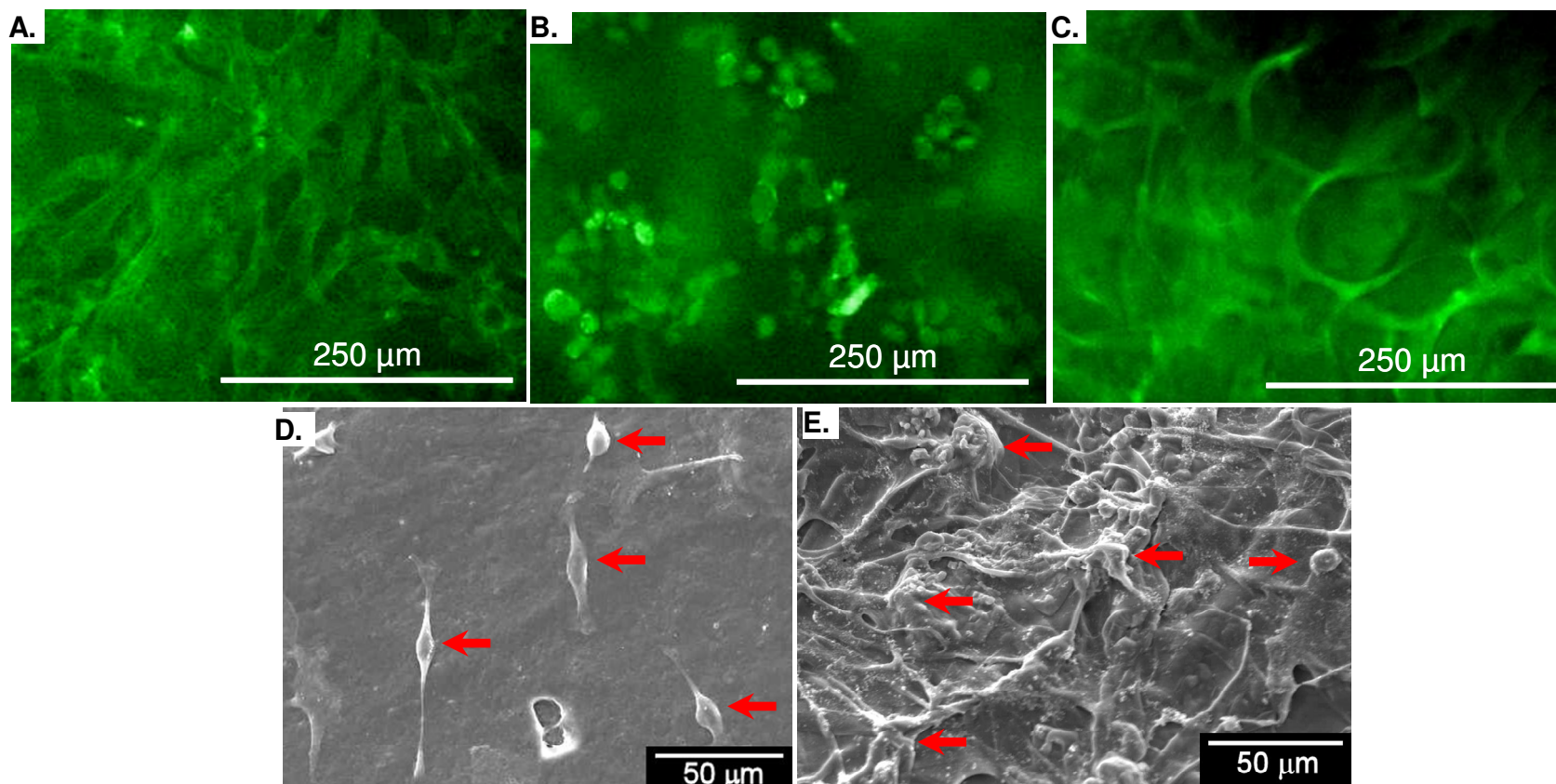


Figure 16. Composite Matrices Guide the Spreading, Adhesion, and Proliferation of MEFs.

Fluorescence micrographs of actin stained cells on (A) Tissue culture plastic, (B) 2-D PLGA films, and (C) 3-D composite scaffolds. Scanning electron micrographs of (A) 2-D PLGA films and (E) 3-D composite scaffolds. Arrows indicate the position of cells.

Viability of MEFs was measured by monitoring the metabolic oxidation of resazurin. The decrease in resazurin absorbance was similar for all samples, showing that the composite structure supported viable cells (**Figure 17A**). To understand the functionality of fibroblasts, the amount of MMP-2/MMP-9 secreted into the growth medium was monitored using a fluorogenic substrate specific for MMP-2/MMP-9. **Figure 17B** shows the MMP-2/MMP-9 activity in relative fluorescence units (RFU) per mg total protein. The RFU/mg is similar for all samples, showing that the composite scaffold does not harm the activity of MEFs. Additionally the decrease in activity seen in the TCP and PLGA samples by day 7 could be attributed to the contact inhibition of overconfluent cells and thus producing less MMP-2/MMP-9. However, this decrease was not observed in the composite scaffold as the 3D porous structure offered a larger surface area for cell attachment and may not have reached confluency.

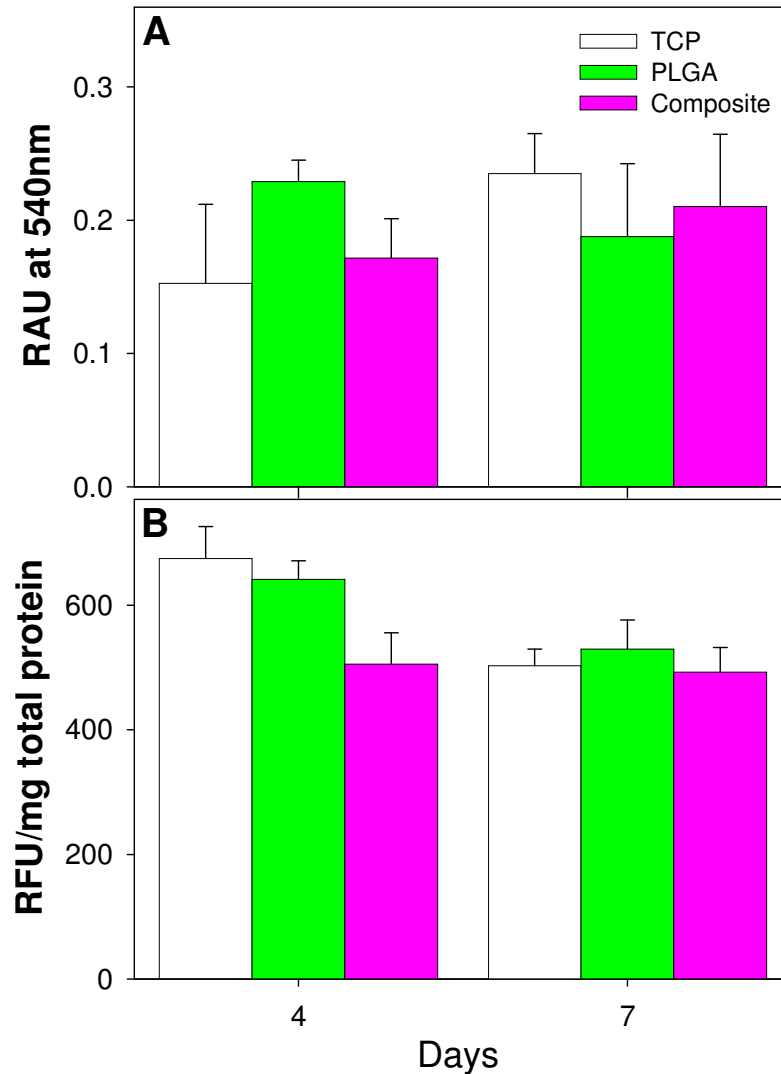


Figure 17. Composite matrices support fibroblast colonization and activity.

(A) Viability shown in relative absorbance units (RAU). (B) MMP2/MMP9 activity shown in relative fluorescence units (RFU) per mg of total protein in the medium.

Additionally, the colonization of SMCs on the composite structure was analyzed by SEM (**Figure 18A,B**) and fluorescence microscopy (**Figure 18C**). Results showed a large number of cells attached to the composite scaffold. Additionally, the cell structures mimicked the pore morphology suggesting that the porous structure can be used to guide the ingrowth and spatial arrangement of cells.

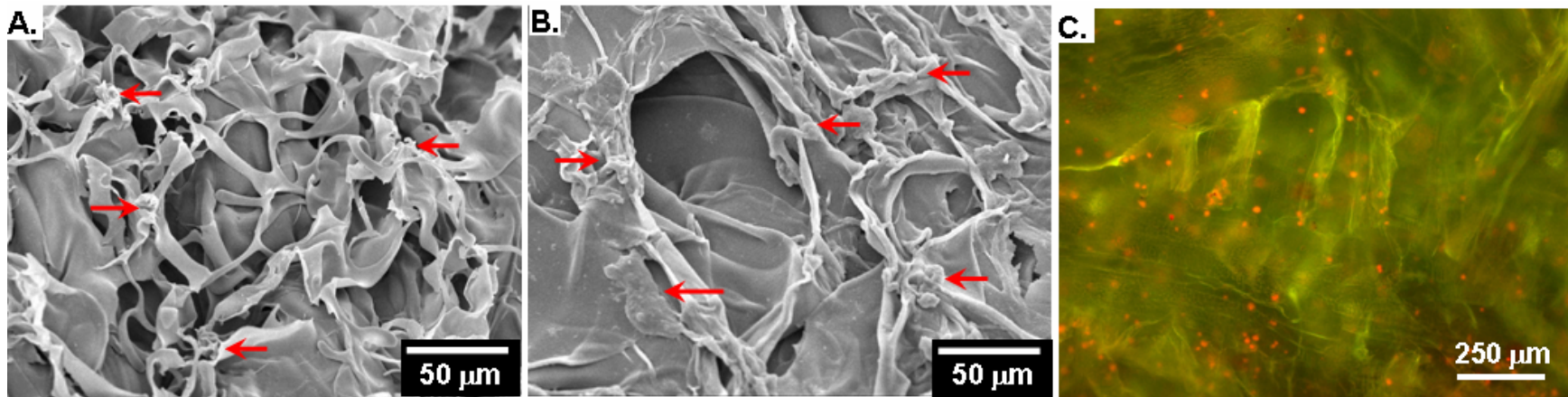


Figure 18. Composite matrices guide the spreading and adhesion of SMCs.

Scanning electron micrographs of smooth muscle cells on both (A) Chitosan and (B) Composite Scaffolds. Arrows indicate the position of cells. (C) Fluorescence micrograph of propidium iodide and actin stained composite scaffold.

3.5. Discussion.

The formed composite contained a three layer sandwich structure with two porous chitosan layers surrounding a continuous PLGA layer. The three layers were mechanically interlocked with the two chitosan layers forming anchor points through perforations in the PLGA. Perforations were formed by puncturing the PLGA film in a 1cm x 1 cm square pattern using stainless steel nails. Using this method the perforation size and layout could easily be controlled. Additionally, the composite matrix proved to be less permeable to urea than SIS³. Even after 48 hours the composite did not show appreciable urea diffusion. The lack of diffusion is a result of the transport barrier created by the mechanical interlocking, showing that the perforations were sealed by the chitosan layers. The reduced permeability should help limit inflammation by preventing urea leakage into surrounding tissue.

Three different M_w of PLGA were tested mechanically. Since 160 kDa PLGA membranes showed tensile strength values greater than SIS, they were used exclusively when fabricating the composite structure. The composite showed tensile properties similar to SIS³. The stress strain curve exhibited non-linear behavior and the break stress of the composite was larger than SIS. As expected, mechanical failure of the chitosan layers showed very little effect on the stress strain curve. Therefore, the majority of the composite matrix's tensile strength was provided by the PLGA membrane. This provides an opportunity to alter the bioregulatory properties of the chitosan matrix without greatly affecting the mechanical properties of the composite. Nevertheless, further mechanical testing including cyclical tests or burst stresses should be performed to explore the utility of formed composite matrices in tissue engineering

applications. The composite's nonlinear stress-strain behavior also suggests the possibility of viscoelastic behavior. Therefore, it would also be useful to model the viscoelastic behavior of the composite structure and compare it to SIS. Additionally, the strain for both PLGA films and composite structure was higher than other literature sources. Using 50:50 PLGA, others have reported up to 80% strain using acetone as the solvent²⁶¹. Previously, we have reported that the solvent affects the properties of the matrix. For example, using PCL membranes cast after dissolving in chloroform had an extension up to 1000% whereas membranes cast in water after dissolving in acetic acid had only 30% strain¹¹⁰. The variability of mechanical properties may be a result of the microstructural architecture of the material.

Long term composite degradation studies showed significant overall weight loss over eight weeks (50%). The weight loss was accompanied by a linear reduction in the M_w of PLGA layer, reducing the M_w by 80% over 7 weeks. A linear drop in M_w is expected because PLGA degrades hydrolytically. The drop in M_w correlates to a drop in mechanical strength and a loss of structural stability. After 8 weeks the scaffolds cannot be handled. This showed that the physical properties of the composite scaffold are primarily controlled by the PLGA layer.

Previous research has shown that porous chitosan matrices show support for cell growth and attachment of various cell types including fibroblasts and SMCs^{14, 231, 258}. Using both MEFs and SMCs the composite matrices demonstrated cell spreading characteristics similar to chitosan matrices. Additionally fibroblasts were found to be viable (capable of oxidizing resazurin) and functional (produced active MMP-2/MMP-9). This showed that the process of creating a composite scaffold does not hinder the

chitosan layers' capacity for cell colonization or the potential for cell growth.

Additionally, all the cell culture experiments were performed at a single seeding density and cells were seeded on only one side of the composite structure. The low density of seeding could have resulted in the i) cells remaining distant from each other, ii) attached to bottom of the pores near the vicinity of the PLGA membrane, and iii) decreased mass transfer of nutrients/waste products due to non-porous PLGA membrane. Previous research indicated that raising the seeding density shows a greater change in cell growth between the 2D and 3D chitosan material ¹⁴. Cells may also have entered into the scaffold and attached to or been influenced by the PLGA layer.

Based on the need to alter the biological activity, one could complex chitosan with other bioactive polymers such as gelatin⁵ or glycosaminoglycans²⁵⁸. In order to better mimic the biological properties, one could incorporate biodegradable nanoparticles to deliver essential growth factors²⁶². Cellular signals could be better controlled by adding a controlled release delivery mechanism to the composite scaffold. The multilayer design also shows the potential to grow multiple tissue layers simultaneously. For example, smooth muscle cells may be seeded onto one side of the composite while urothelial cells are seeded on the other to regenerate multilayer bladder tissue. Each side could be embedded with a different loaded enabling a heterogeneous release of signaling molecules. Additionally, the central layer should provide a barrier between the two tissue compartments, preventing in-growth of one cell type into the other until both regenerated tissues have time to reorganize.

This method for fabricating composite scaffolds is not limited solely to the PLGA and chitosan system. The central polymer film could be created by any desired method, and the outer layers could be added provided the solvent does not dissolve the central layer. Additional studies utilizing other polymers such as PCL and gelatin, should be performed. For example, a scaffold containing low molecular weight PCL and gelatin would provide faster degradation. Scaffolds containing PCL and a blend of chitosan and gelatin could possibly improve bioactivity. It may also be possible to form a two layer asymmetric matrix. Biological activity could be enhanced by using either gelatin or blended chitosan/gelatin hydrogels instead of the 3D porous chitosan. The system could also be modified for use in layer by layer microfabrication. Standard photolithographic methods which enable more precise control of the perforation pattern could also be used to fabricate composite scaffolds²⁶³.

3.6. Summary

In summary, the composite design retains both the desirable mechanical properties of synthetic polymers and the biological properties of natural polymers, and matches characteristics of SIS (**Table 2**). The composite material lacks growth factors and other signaling molecules, therefore it would be useful to incorporate a nanoparticle system for controlled release into the material. However, the composite shows tensile properties similar to SIS, demonstrates the capacity for cell colonization, undergoes substantial degradation after 8 weeks. The composite scaffold shows significant potential for use in tissue engineering applications.

Table 2. Summary of composite structure properties.

	Natural Matrices (SIS) ³	Natural Polymers ⁷⁷	Synthetic Polymers ¹⁶	Composite Scaffolds ¹⁶
Mechanical Strength	3 MPa	2 – 6 kPa	1 – 9 MPa	3.5 – 5 MPa
Degradation Time	4 weeks	6 – 12 months	4 weeks	8 weeks
Cellular Support	Yes	Yes	No	Yes
Growth Factors	Yes	No	No	No

Chapter 4

Local Mass Transport Properties

4.1 Nanoparticles in Tissue Engineering

An important factor in tissue growth and development is the presence of cellular signals. As discussed previously, one of the key advantages of natural matrices is that they already contain growth factors and other signaling molecules. Growth factors, such as vascular endothelial growth factor (VEGF) and basic fibroblast growth factor (bFGF) are important for cell colonization, growth differentiation, and vascularization. Therefore, it would be advantageous to incorporate growth factors into polymeric scaffolds. However, growth factors are proteins with short half lives, the half life of bFGF is only 45 minutes *in vivo*²⁶⁴. Growth factors must be protected from denaturation until they are released into the body. Because of this short half life, freely injected growth factor do not illicit an adequate healing response, but sustained release of the growth factor may lead to accelerated tissue regeneration²⁶⁵. One method of incorporating growth factors is to use degradable particles as delivery vehicles. A variety of controlled release particle systems, varying in size from micro (1-10 μm) to nano (<1000 nm, but typically under 200 nm) scale^{266, 267}, have been widely studied for cellular encapsulation⁷⁶ and drug delivery applications²⁶⁸.

Nanoparticles and other nanostructures materials have been used in a variety of aspects in tissue engineering^{269, 270}. Nanoparticles can be formed using several methods including double emulsion systems²⁷¹, emulsion polymerization²⁷², droplet formation²⁷³, or ionic condensation^{274, 275}, and have been used for controlled delivery of drugs or bioactive molecules. Degradable particles capable of controlled release have been created from chitosan²⁷⁴⁻²⁷⁶, PLGA^{268, 277}, and gelatin^{265, 278}. For example biodegradable poly(lactic-*co*-glycolic) acid (PLGA) nanoparticles (NPs) have been manufactured using double emulsification–solvent evaporation method and used as a vehicle for delivering various bioactive molecules including nucleotides²⁷⁹⁻²⁸¹, and drugs²⁸²⁻²⁸⁴ for therapeutic purposes²⁸⁵⁻²⁸⁷. Controlled release particle technology been used to incorporate a variety of growth factors important for angiogenesis, wound healing, and bone growth²⁸⁸ as well as dental, oral and craniofacial applications²⁸⁹.

Particles can be loaded for release either during fabrication, or by absorption of proteins after the particles are created. The growth factors can be encapsulated in nanoparticles and then released by diffusion through the polymer matrix²⁹⁰ or through expulsion of the growth factor using particle expansion²⁹¹, particle bursting²⁹², or surface erosion²⁹³. Nanoparticles can degrade via a wide variety of mechanisms, including surface erosion and bulk degradation. Surface eroding materials degrade via a surface initiated mechanism and degrade one layer at a time, providing a uniform release profile. Bulk erosion typically leads to a delayed release of the drug, providing a high concentration release at one time point. Bulk degrading materials degrade at all points of the material, often leading to the centers of the particles degrading faster than the edges. This is most prevalent in synthetic polyesters such as poly (lactic-*co*-glycolic acid)

(PLGA), which degrade by hydrolysis, and have acidic degradation products. Therefore the pH within the particle lowers the particle degrades, catalyzing faster degradation of the particle^{294, 295}.

After loaded nanoparticles are produced, there are several ways to include them in the scaffolds. In one configuration the particles are concentrated at one point within the scaffold. As the particles release their growth factors a concentration gradient forms with the maximum concentration at the particles. However, particles have other useful properties which affect the properties of tissue engineering materials. Particles can be used to modify the 3D structure of tissue scaffolds and thus alter their transport properties. If nanoparticles are entrapped in a porous material they will block small porous features and can change the material's transport properties. For example, latex particles have been used to lower the permeability to urea of SIS²⁷⁷. Other nanomaterials such as hydroxyapatite²⁹⁶ and carbon nanotubes²⁹⁷ have been used to physically reinforce scaffold matrices as well as provide specific 3D structural properties.

Nanoparticles have been developed to target specific tissues and areas of the body. Nanoparticle delivery can be controlled by modifying the surface to include specific marker and adhesion proteins. For example particles which display RGD binding proteins on their surface specifically target endothelial cells and reduce angiogenesis²⁹⁸. Additionally, the magnetic properties of specialized nanoparticles can be used direct particles to specific sites non-invasively using magnetic fields²⁹⁹. Some of the key weaknesses of magnetic particles are biocompatibility and the ability to control the quality of magnetic particles, their size distribution, their shape and surface. However, research into surface coatings has improved the quality of magnetic particles

²⁹⁹. The magnetic particles are surface modified with RGD binding sites and arranged by magnetic fields. Then the cells attach to the pattern determined by the particles ³⁰⁰.

Another method to target drug or growth factor release is through particle mediated heating of temperature sensitive materials. Nanosize particles within the matrix can be used to induce temperature changes thereby releasing a desired payload, causing a phase change or thermal expansion, or modifying the material's 3D architecture³⁰¹.

Several techniques exist to selectively heat particles including light induced heating of gold particles²⁹² and subjecting magnetic nanoparticles to alternating magnetic fields²⁹⁹. This heating may also be used to degrade and remove harmful elements from the body such as amyloid plaques common in Alzheimer's patients³⁰². The heat generated can also be utilized to selectively kill cancer cells³⁰³.

In living systems the nanoparticle itself must be biocompatible and non-toxic. However, when placed in a biological system the particles are rapidly coated with a layer of proteins. Therefore, the particle is identified in the system not by its own surface but by the protein corona on its surface ³⁰⁴. Therefore it is also important to study the adsorption of proteins onto the particle surface.

However, particles have other useful properties which affect the properties of tissue engineering materials. Particles can be used to modify the 3D structure of tissue scaffolds and thus alter their transport properties. If nanoparticles are entrapped in a porous material they will block small porous features and can change the material's transport properties. For example, both PLGA and latex particles have been used to lower the permeability to urea of SIS ¹⁰⁹. Other nanomaterials such as hydroxyapatite²⁹⁶ and carbon nanotubes ²⁹⁷ have been used to physically reinforce scaffold matrices as well

as provide specific 3D structural properties. By altering the microarchitecture of SIS we sought to lessen the sample to sample heterogeneity in order to improve the consistency of tissue regeneration using nanotechnology.

In this study, we investigated the possibility of modifying both SIS and the multilayer composite structure using a variety of nanoparticles made from polystyrene latex, PLGA, PLGA-HA, and chitosan. Modifications to the microstructure of both SIS and the composite were measured using scanning electron microscopy. Additionally, the change in the transport properties across SIS was characterized by the change in permeability of urea. The permeability was decreased based on both the size and number of particles present. NPs did not alter the mechanical properties of the SIS, and the both NP modified SIS and composite continued to support cell adhesion and proliferation; and cell growth was significantly higher in PLGA NP modified SIS as compared to the unmodified SIS.

4.2. Materials and Methods

4.2.1. Sources of Material

PLGA with a 50:50 monomer ratio, molecular weight of 106 kDa, and viscosity of 1.05 dl/g was purchased from Absorbable Polymers International (Pelham, AL). Negatively charged polystyrene latex spheres (six sizes between 50 nm and 2000 nm), urea, poly(vinyl alcohol) [PVA], poly(ethyleneimine) [PEI], and MCDB cell culture medium were obtained from Sigma–Aldrich (St. Louis, MO). Single layer SIS (Surgisis[®]) was obtained from Cook[®] Biotech (West Lafayette, IN). Chloroform was purchased from EMD Chemicals (San Diego, CA). Urea assay kit was purchased from Diagnostics Chemicals Limited (Oxford, CT). Fetal bovine serum (FBS) and penicillin–

streptomycin were obtained from Invitrogen (Carlsbad, CA). Human mammary endothelial cells (HMEC-1) were provided by Dr. Mike Ihnat at the University of Oklahoma Health Sciences Center³⁰⁵.

4.2.2. Synthesis of PLGA NPs

Both PLGA nanoparticles and nanoparticles formed by conjugating PLGA and hylauronic acid (PLGA-HA) were a gift from Mr. Fadee Mondalek and Dr. H-K Lin from the University of Oklahoma Health Sciences Center, Department of Urology. PLGA NPs were synthesized using a modified double emulsion solvent evaporation technique³⁰⁶. Briefly, 30 mg of PLGA was first dissolved in 1 ml of chloroform. An aliquot of 200 μ l of 7% PEI (used to produce positively charged nanoparticles) was added to the PLGA/chloroform solution followed by sonication on ice with a probe sonicator (model VC60; Sonics & Materials, Danbury, CT) set in a continuous mode for 30 s at 100% amplitude. The primary emulsion was transferred into 10 ml of 1% PVA; and the entire solution was sonicated on ice for another 1 min. The organic solvent in the final solution was allowed to evaporate overnight with continuous stirring. PLGA NPs were recovered by centrifugation at $30,000 \times g$ for 20 min at 4°C. The pellet consisting of aggregated NPs was weighed and washed three times with water to remove any residual PVA. PLGA NPs were then resuspended in water using sonication to obtain a final concentration of 2 mg/ml. The NPs were either used immediately or freeze-dried and then stored at -80°C for later use.

4.2.3. Forming Chitosan Nanoparticles

Chitosan nanoparticles were created using ionic condensation^{275, 307}. In brief, 300 μL of 0.93 mg/mL sodium tripolyphosphate (TPP) solution was added to 700 μL of 1.8 mg/mL high molecular weight chitosan solution containing 0.1% (v/v) acetic acid under sonication. Fluorescent particles included 50 μL of 0.5 mg/mL fluorescein isothiocyanate (FITC). Particles were centrifuged at (14,000 rpm), washed with water three times, and used immediately.

4.2.4. Characterization of Nanoparticles

Particles were assessed for the particle size, polydispersity index, and zeta potential using diffraction light scattering Zeta PALS (Brookhaven Instruments, Holtsville, NY) at room temperature. Viscosity and refractive indices were set equal to those specific of water. Particle concentration was measured using a FACSCalibur flow cytometer (Becton–Dickinson, San Jose, CA). For this purpose, synthesized NPs were diluted in water at four different concentrations. Particle concentrations were calculated using a calibration curve developed using commercially available latex particles with four different known concentrations.

4.2.5. Microarchitecture analysis of nanoparticle modified structures

SIS was cut into 1.2 cm \times 1.2 cm pieces and assembled in 1.5 ml Eppendorf tubes between the lid and the tube with mucosal side facing upwards. NPs were loaded onto the mucosal side of the SIS inserts. The inserts were incubated overnight at room temperature with a constant shaking on an orbital shaker. To evaluate the microarchitecture of the NP modified SIS, the modified biomatrix was dehydrated using increasing concentrations of

ethanol followed by a brief vacuum drying. Samples were then sputter coated with a 15 nm thick layer of gold at 40 mA and analyzed using an SEM (Joel scanning microscope).

4.2.6. Particles integrated into composite structure

PLGA/chitosan composite structures were formed as discussed previously. The composite was cut into 2 cm x 2 cm pieces and six pieces were secured to Teflon plates with silicon glue. Silicon wells were then formed as described previously. After the silicon dried the composite structure was neutralized with ethanol and rinsed with water. Then 1 mL of appropriate nanoparticle solution (2000 nm latex, 500 nm latex, PLGA, PLGA-HA, and chitosan particles, as well as a control without particles) was added to each well. The plates were then immersed in water and the particles were allowed to settle overnight. Finally the structures were air dried, sputter coated with a 15 nm thick layer of gold at 40 mA, and analyzed using an SEM (JEOL scanning microscope).

4.2.7. Characterization of properties of PLGA NP modified SIS

SIS was converted into wells constructed using silicone glue on the mucosal side; and PLGA NP suspensions with the concentration of 1.273 mg/cm^3 were added onto the mucosal side of SIS. The assembly was placed on an incubator shaker at 37°C overnight. The NP modified SIS membranes were rinsed with water to remove unattached NPs. The thickness of the NP modified SIS was measured using our previously described method³. Briefly, the NP modified SIS membranes were cut into small (2 mm \times 10 mm) strips. Digital micrographs of the cross section were recorded using an inverted microscope equipped with a CCD camera. The cross section distances were measured using Sigma

Scan Pro software (Systat Software, Inc., Point Richmond, CA) which was calibrated using an image of a hemocytometer. Tensile properties were then determined by our previously described method^{110, 308}. In brief, , 6 cm × 1 cm strips of NP modified SIS membranes were cut from each sample and analyzed using an INSTRON 5842 (INSTRON Inc., Canton, MA) with a constant crosshead speed of 10 mm/min. Tests were performed under hydrated conditions at 37°C using a custom designed chamber.

4.2.8. Urea permeability studies of NP modified SIS

Permeability was analyzed using the apparatus built in-house as previously described³⁰⁸. Briefly, latex spheres and PLGA NPs were suspended in phosphate buffered saline (PBS), and placed on the mucosal side of SIS placed in the permeability chamber. NPs were allowed to settle onto the SIS through gravity on an orbital shaker at 37 C overnight. The NP modified SIS membranes were washed three times with PBS in the chamber, and filled with 550 mM urea (typical concentration at physiological conditions) in PBS. PBS was then added to the serosal side of SIS in the second chamber. Aliquots of samples (20–50 µl) were collected from the second chamber between 0 min and 2 h. Samples collected immediately after the assembly of the chambers were used as time-zero values (i.e. C_2 at $t = 0$). Concentrations of urea were determined using a urea assay kit (Diagnostic Chemicals Limited, Oxford, CT).

Membrane permeability was calculated as described previously³⁰⁸. In brief, the following equation is obtained using a quasi-steady state approximation

$$\ln\left(\frac{C_0 - 2C_2}{C_0}\right) = -\left(\frac{A_m}{V}P\right)t \quad (4)$$

where C_2 is the concentration of the urea measured at any time t in chamber 2, C_0 (550 mM) is the initial concentration in chamber 1, A_m is the membrane area (3.1416 cm^2 as the radius of the chamber is 1 cm), V is the volume of each chamber (4 ml), and P is the permeability of the matrix. Then $\ln(C_0 - 2C_2)/C_0$ was plotted as a function of time from which the slope ($(A_m P)/V$) was determined using a linear fit. The permeability was calculated using the slope values.

4.2. Statistical analysis

Statistical differences between two experimental groups were evaluated using student's t -test. A statistically significant difference was considered when $p < 0.05$.

4.3. Results

4.3.1. Characteristics of synthesized NPs

The average diameter of synthesized PLGA NPs ranged between 162 nm and 306 nm. Polydispersity indices varied from batch to batch, but the value was approximately constant at 0.06. The zeta potential ranged between +40 mV and +50 mV, depending on the batch of PLGA NPs synthesized. The morphology of the PLGA NPs as assessed by the SEM showed a porous outer surface (data not shown). The concentration assessment by flow cytometry indicated that 1 mg/ml PLGA NPs suspended in water generated 1.62

$\times 10^8$ particles/ml. PLGA-HA particles averaged a diameter of 1300nm with a polydispersity of 0.3 and a zeta potential of -12 mV. Chitosan particles had a diameter of 270nm, a polydispersity of 0.25, and a zeta potential of 33 mV.

4.3.2. Surface structure of NP modified SIS

Commercial nominally monodisperse polystyrene latex spheres (sizes between 50 nm and 2000 nm) were used to determine appropriate sizes of NPs to embed within SIS in order to reduce permeability to urea. Latex spheres with diameters ranging between 200 nm and 500 nm appeared on both mucosal and serosal sides of SIS (**Figure 19 C, C'–E, E'**). In contrast, larger sizes (1000 nm and 2000 nm) of latex spheres were predominantly present on mucosal side of SIS (**Figure 19 A, A', B and B'**), whereas smaller size (50 nm) latex spheres were not observed on either side of SIS (**Figure 19 F and F'**). These results suggested that NPs smaller than 200 nm could not be retained in SIS; and NPs larger than 500 nm could not fit into the porous structure of SIS.

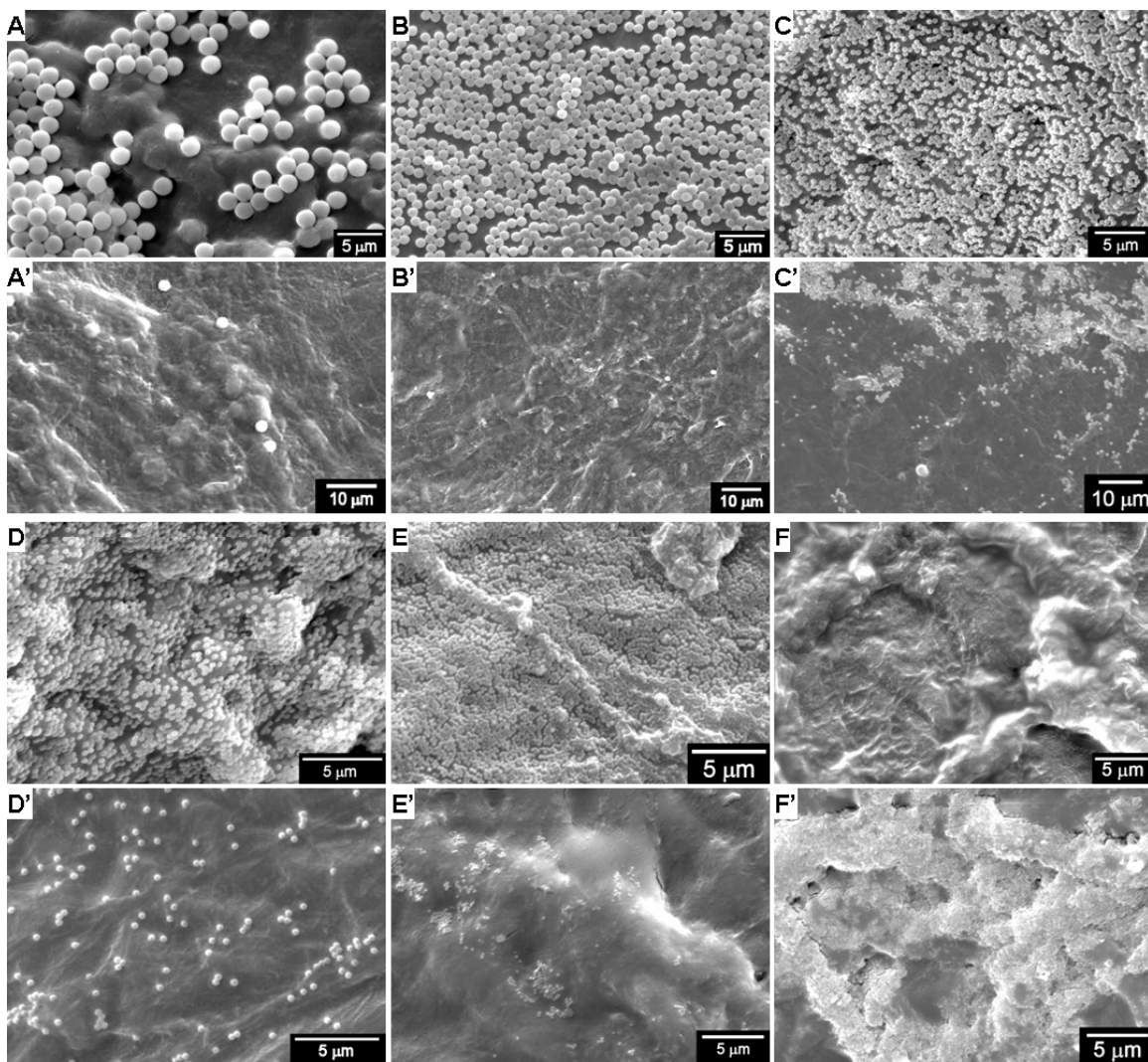


Figure 19. SEM images of latex spheres modified SIS.

Mucosal sides of SIS were imaged following overnight embedding of 2 μm (A), 1 μm (B), 500 nm (C), 300 nm (D), 200 nm (E), and 50 nm (F) latex spheres. Serosal sides of the same SIS membranes were also imaged (A'–F').

To determine whether PLGA NPs also possessed similar characteristics as latex spheres, two sizes of PLGA NPs (162 nm and 306 nm) were placed onto the SIS. SEM images demonstrated that both sizes of PLGA NPs (**Figure 20**) went through the SIS similar to latex spheres. However, less NPs with 162 nm in size (**Figure 20B**) were retained on the mucosal side of SIS as compared to the serosal side (**Figure 20B'**). Furthermore, more NPs with 306 nm in size were retained on the mucosal side (**Figure 20C**) relative to serosal side (**Figure 20C'**). Nevertheless, these results confirmed that NP sizes ranging between 200 nm and 500 nm would be appropriate to fit into the porous structure of SIS.

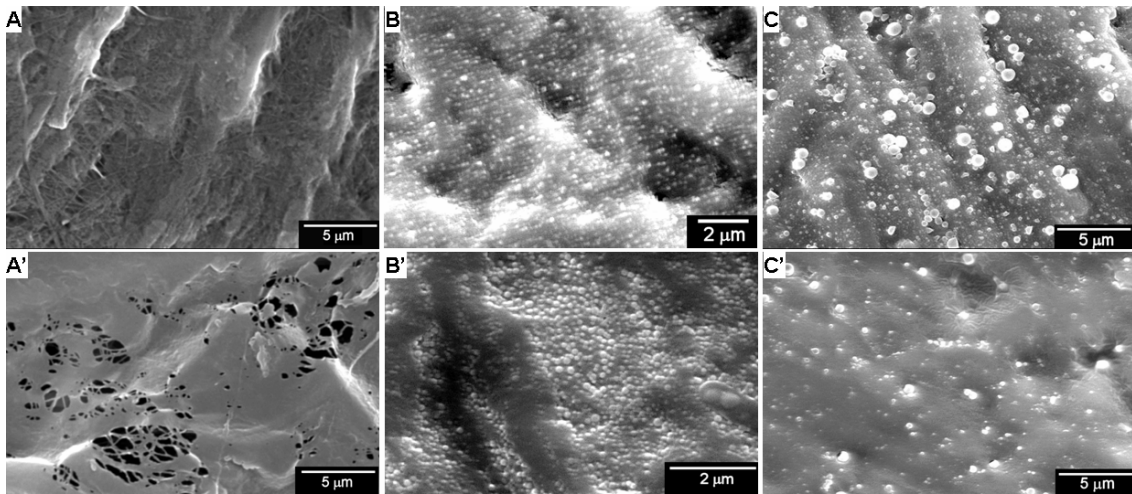


Figure 20. SEM images of PLGA NP modified SIS.

Unmodified SIS was imaged on mucosal side (A) and serosal side (A'). Following 162 nm PLGA NPs embedding, mucosal side (B) and serosal side (B') of the SIS structure were shown. Panels C and C' show SIS modified by 306 nm PLGA NPs on mucosal and serosal sides of SIS, respectively.

4.3.3. Particles integrated into composite structure

Next particles a variety of particle types were integrated into the composite matrix. Because of the mechanical interlocking through the composite particles can only be integrated one side at a time. However, particles are clearly visible, showing that they can be incorporated into the composite structure (**Figure 21**).

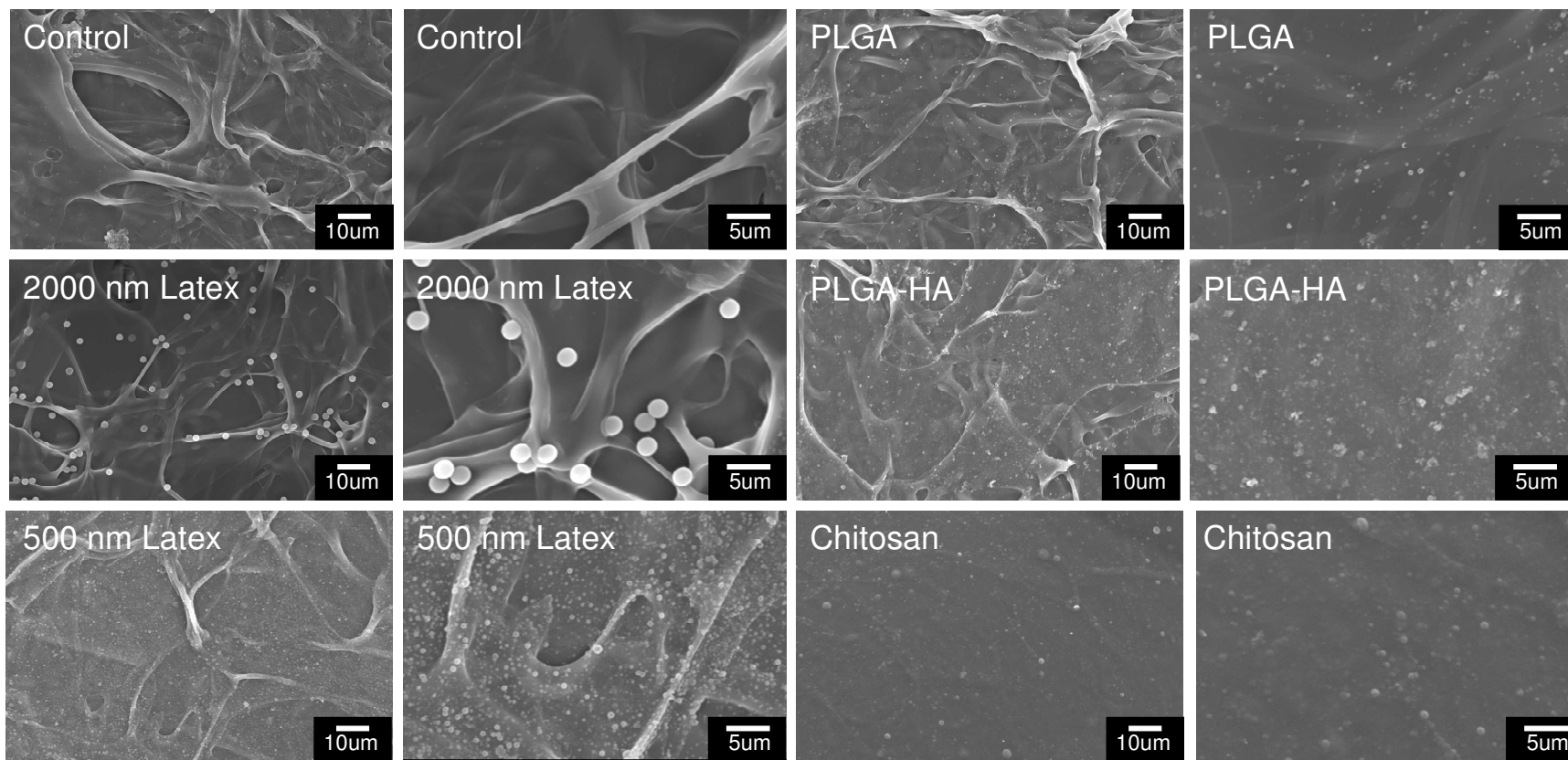


Figure 21. Particles integrated into the composite structure.

4.3.4. The effect of NPs on SIS permeability

NP modified SIS had reduced permeability as compared to unmodified SIS (**Figure 22A**). The permeability was 1.13×10^{-3} cm/s in unmodified SIS as compared to 7.71×10^{-4} cm/s in SIS embedded with 200 nm latex sphere. The permeability was reduced further to 6.53×10^{-4} cm/s when 300 nm latex spheres were used as compared to unmodified SIS. When 500 nm latex spheres were used, urea permeability did not show significant reduction from that of unmodified SIS.

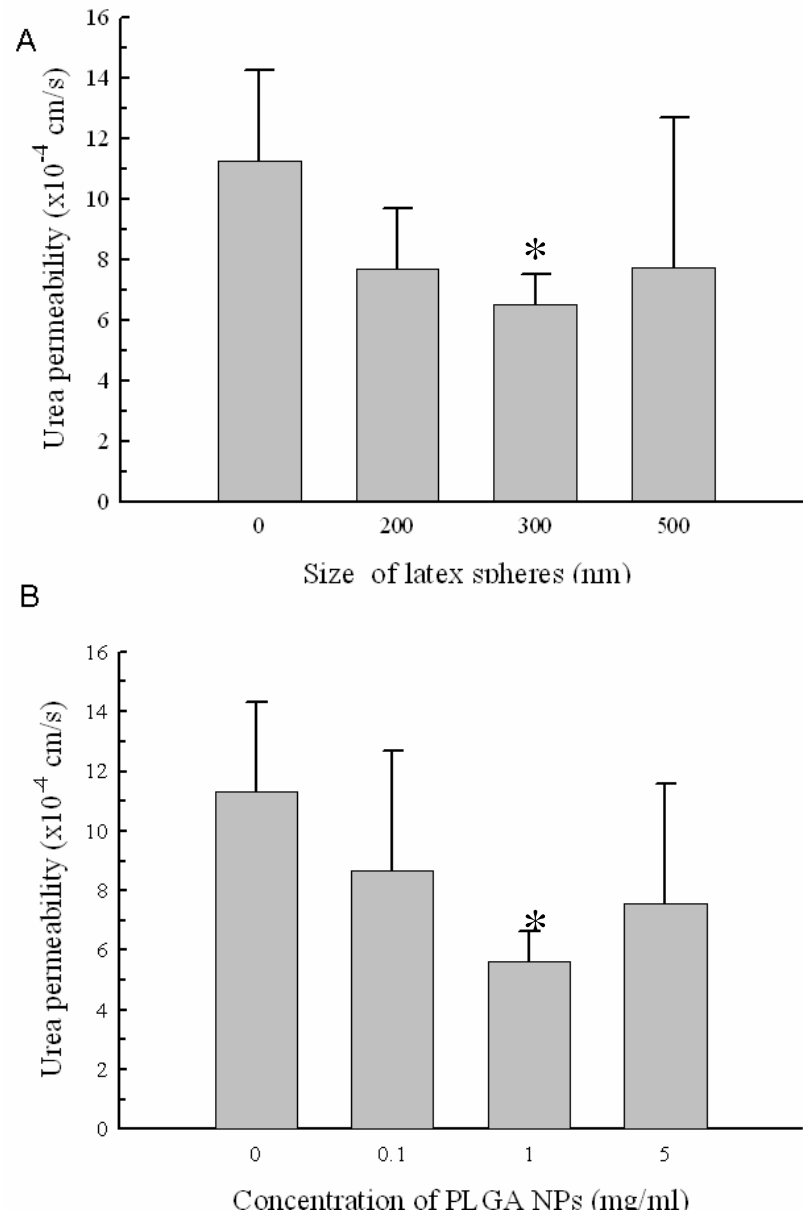


Figure 22. Alteration of SIS permeability to urea by NPs.

Permeability chambers were set up by placing latex spheres (A) or PLGA NPs (B) on the mucosal side of SIS to demonstrate size-dependent and concentration dependent permeability, respectively. Zero size or zero concentration indicates permeability measured with unmodified SIS, i.e. no particles. Results are present as mean \pm standard deviation from three independent experiments. * Indicates that these results were different vs. unmodified SIS ($p < 0.05$).

The permeability of the SIS to urea was then measured after introducing 260 nm PLGA NPs to SIS. Three different concentrations, 0.1 mg/ml, 1.0 mg/ml, and 5.0 mg/ml of PLGA NPs, were used to determine concentration dependent changes in permeability. The permeability was significantly reduced to 5.63×10^{-4} cm/s when 1.0 mg/ml PLGA NP was used to embed SIS as compared to either 0.1 mg/ml or 5.0 mg/ml PLGA NPs (**Figure 22B**).

4.3.5. The effect of NPs on SIS mechanical properties

To assess the effect of embedding NPs into SIS on its mechanical properties, tensile properties of PLGA NP modified and unmodified SIS were compared. These results showed no significant difference in break stress or break strain (**Figure 23**). In addition, when elastic modulus was calculated in the linear range (10–20% strain range), no significant difference was detected between NP modified SIS and unmodified SIS. Both samples showed elastic modulus of 26 MPa, similar to our previous results³. However, the thickness of wet SIS in this study averaged $110 \mu\text{m} \pm 21 \mu\text{m}$ as compared to $246 \pm 16 \mu\text{m}$ in our previous study.

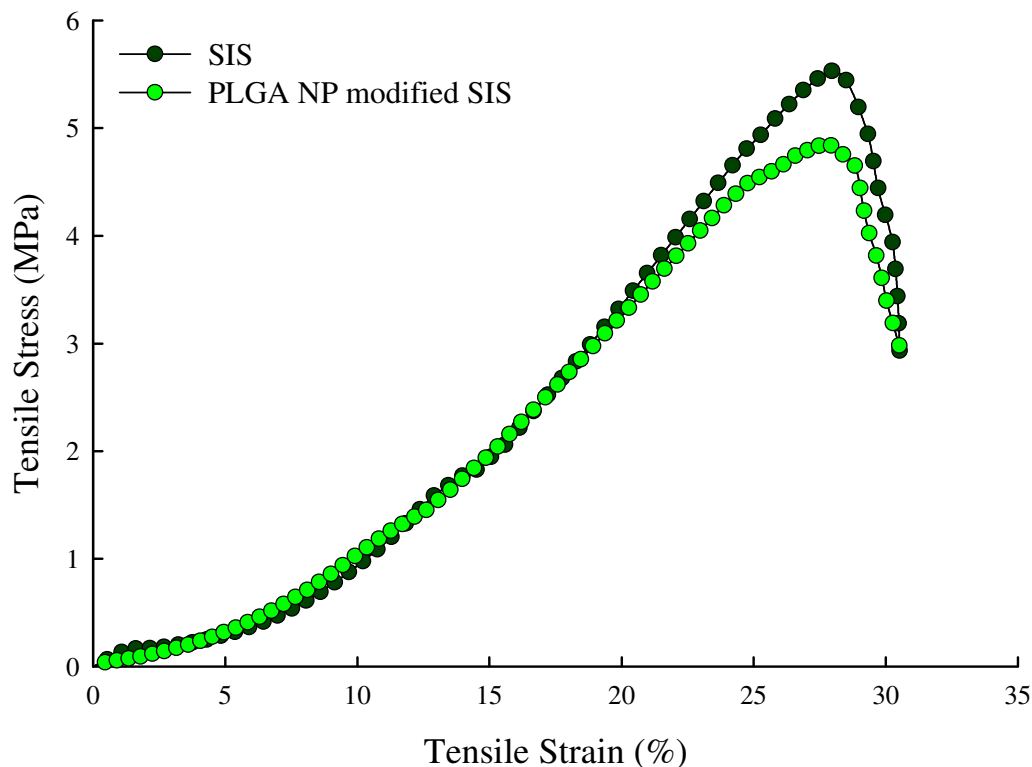


Figure 23. Stress–strain curves of SIS with and without PLGA NPs.

4.4. Discussion

As noted in chapter 3, SIS has been intensively investigated for its capability in tissue repair and regeneration in a variety of tissues and animal models in the last 20 years. SIS has been shown to be a promising biomaterial for tissue regeneration because it is formed from extracellular matrix elements and contains growth factors and other cellular signals that may promote cell migration, growth, and differentiation³⁰⁹. Therefore, one way to improve the composite polymer structure and better approximate the characteristics of SIS is to incorporate a mechanism for the controlled release of growth factors and other cellular signals into the polymer matrix. Additionally, numerous attempts have been made to produce “off-the-shelf” SIS products that would be

available for clinical reconstructive surgical procedures^{56, 310-312}. However, SIS suffers from inconsistent results in various applications. These inconsistencies may result from heterogeneities inherent in natural matrices³⁰⁸. The presence of a controlled release delivery system will affect the transport properties of the material. One such delivery system utilizes nanoparticles to deliver the cellular signals. These particles may embed themselves into the porous structure and reduce the permeability of the system. Therefore, incorporating the nanoparticle system into SIS may reduce the sample to sample heterogeneity in the system. A more consistent material may improve the consistency of tissue regeneration.

Because SIS is a decellularized natural matrix, the pores in the SIS are neither uniformly distributed, nor are they uniform in size³⁰⁸. They vary in size from pores that were previously blood vessels to tiny spaces between collagen fibers. Additionally, the porous structure changes across the thickness of the SIS. For example permeability of urea across the serosal side of SIS is greater than across the mucosal side³. This large pore size distribution explains the wide size ranges (200 nm – 500 nm) of particles capable of embedding themselves in SIS. The absence of small size NPs (50 nm) within SIS in the SEM images may be because the 50nm particles traveled completely through the porous matrix without embedding themselves, or it may be an artifact of the characterization techniques employed. First, the 15 nm gold used for coating during SEM procedures may make the particles difficult or impossible to be distinguished from the SIS, and visualizing the 50 nm latex particles on SIS may be beyond the resolution limitations of the SEM. It is also important to note that SIS differs from batch to batch from the same manufacturer. For example, in 2005 we reported Cook SIS thickness as

101 $\mu\text{m} \pm 19.84 \mu\text{m}$ (dry) and 246 $\mu\text{m} \pm 16.22 \mu\text{m}$ (wet)³. In the present study (2007), thickness of the Cook SIS was 29.6 $\mu\text{m} \pm 6.4 \mu\text{m}$ (dry) and 110 $\mu\text{m} \pm 21 \mu\text{m}$ (wet)²⁷⁷. Based on the inconsistency of the SIS and the wide variation in pore size, a combination of different sizes of NPs might ultimately be needed to achieve maximal uniformity of SIS. Additionally, further experiments by our collaborators confirmed that the modified SIS supports cellular colonization of endothelial cells²⁷⁷.

Permeability studies indicated that there was no statistically significant difference between the unmodified SIS and 200 nm latex spheres modified SIS, or between the unmodified SIS and 500 nm latex spheres embedded SIS. In contrast, a significant difference was detected between the unmodified SIS and 300 nm NP modified SIS. It appeared that the 200 nm NPs plugged some of the SIS pores as observed in the SEM images (**Figure 19**), and perhaps resulted in a slight reduction in permeability. However, the particles may not fill a critical number of the pores to provide a statistically significant reduction in permeability. The same explanation can be applied to 500 nm NPs. In contrast, 300 nm latex spheres seem to fill enough number of pores in SIS to provide a significant reduction in permeability. It may also be possible to further reduce the permeability of SIS if a combination of different sizes of NPs is used for SIS modification.

To determine the minimal concentration of PLGA NPs that can modify SIS, 260 nm PLGA NPs were used in urea permeability assays. With 1 mg/ml PLGA NPs, the permeability was reduced significantly as compared to unmodified SIS. The failure of a higher concentration, 5 mg/ml, to significantly reduce SIS permeability might result from aggregation of this concentration of PLGA NPs; and these aggregates were too large to fit

into the porous structure of SIS and hence could not reduce SIS permeability as seen with larger sizes of latex spheres (1 μm and 2 μm).

Reduction in SIS permeability may be a critical factor in determining the success of tissue repair and regeneration especially in bladder regeneration. Based on our observation, proximal sections of SIS are more permeable to urea than distal sections of SIS³⁰⁸, and have not been successful for bladder regeneration². The leakage of urine in augmented bladder can have detrimental effects on inflammatory responses during the process toward complete regeneration, and may result in the absence of bladder regeneration as we reported in a dog bladder augmentation model². We expect that the reduction in permeability in NP modified SIS may significantly improve tissue regeneration processes particularly in urinary bladder regeneration.

4.5. Conclusion

A nanoparticle system with the potential for controlled release of bioactive molecules has been developed in order to better mimic the properties of SIS in a polymer system. The nanoparticles integrate nicely into the composite as shown by SEM. However, the addition of particles into the system could affect the material transport properties. Therefore the change in transport properties was studied by incorporating the nanoparticle technology into SIS. The particle technology has potential to decrease the heterogeneity of SIS, is a major issue in producing consistent tissue repair and regeneration. The particle system can alter the permeability of the SIS without affecting the mechanical or biological properties of the system. Future work should focus on adding the controlled release element to particles for the polymer system and optimizing the particle embedding methods in order to achieve more a more consistent SIS material.

Chapter 5

Forces and Flow Dynamics in In Vitro Bioreactors

5.1. Bioreactor Overview.

Bioreactors have been widely utilized for regenerating tissues *in vitro*.

Maturation in bioreactors is an important aspect of tissue engineering. Currently, only a small cross section of tissue engineering materials can be used clinically without prior cell seeding². Other materials require that cells be incorporated into the porous structure before being used for tissue engineering.

The bioreactor configuration is becomes important during *in vitro* maturation cell seeded scaffolds. Maturation in reactors ensures sufficient nutrient transport through cell seeded porous scaffolds^{123, 313}. Using bioreactors, an improvement in the quality of the regenerated tissue is observed in some studies³¹⁴. However, other studies show deterioration in the quality of the tissue³¹⁵. Flow of growth medium improves nutrient and waste transport, but alterations in the synthesis of matrix elements induced by shear stresses could deteriorate the tissues³¹⁶. Nutrient transport also becomes important in composite systems. Modifications to the porous structure in order to increase mechanical strength will most likely create a barrier to mass transport¹⁶.

Most studies utilize small scale cylindrical or discoid scaffolds, focusing on wall shear stresses³¹⁷. However, flow within bioreactors containing large porous structures with high aspect ratios has not been studied. In these scale-up systems, non-ideal fluid distribution conditions could arise from two possible factors: channeling, and dead zones. When channeling is present, some of the fluid leaves the reactor immediately without dispersing within the reactor. Dead zones reduce the effective volume of the reactor and prolong the residence time of some of the fluid elements. Non-uniform flow patterns within the reactor could lead to i) poor distribution of nutrients and ii) non-uniform shear stress distribution. These factors affect cellular colonization, proliferation, and the assembly of extracellular matrix elements which affect the quality of regenerated tissues. Hence, one has to understand the fluid distribution and the effect of shape of the reactor.

Some cell types respond to mechanical stress and change the tissue structure and composition to meet the functional demands. There are two primary modes used to subject the scaffold materials to mechanical forces. First, the scaffolds can be mechanically strained utilizing by pushing or pulling on the material^{318, 319}. This mechanical extension or compression offers good control over the range and direction of forces that materials are subjected to. However, the need for a both a method to grip the scaffold and to control the applied forces complicates the design of the reactor adding to the cost. The other main method used to control the mechanical forces that cells are exposed to is through fluid shear stress. Hence, fluid flow within the reactor can be utilized as a way to introduce mechanical stresses to cells³²⁰. The interaction of fluid with a surface creates a shear stress upon the surface. The shear stress becomes especially important in cell seeded porous matrices because the cells see the shear within

the individual pores. The pore shear stress can also change during the process of cellular regeneration. As the cells colonize the material they produce both more cells and they remodel their local microenvironment by producing extracellular matrix (ECM) elements as the porous scaffold material degrades away. Additionally, shear stress affects the scaffold architecture as well as cellular alignment within the structures^{5, 125}.

There are several types of reactors commonly utilized in tissue engineering^{313, 320}. One of the simplest reactor configurations is a spinner flask. A spinner flask batch reactor where the cell seeded construct is placed into standard cell culture flask and agitated by a mechanical stir bar³²¹. Spinner flask design can be modified to better control the flow profile within the reactor. The scaffolds can be anchored to either the flask or the stirrer³²², and in one alternate design a wavy walled flask is used to create better mixing conditions³²³. Another popular reactor design developed by NASA utilizes rotating reactor walls in order to grow cellular constructs in simulated microgravity³²⁴. Rotating wall bioreactors consist of two concentric cylinders with their lengths parallel to the ground. The outer cylinder rotates pulling the fluid and scaffolds up over the inner tube and then the scaffolds free fall until they are pulled up and over again. The scaffold movement provides the driving force for nutrient transport within the porous matrix. Other rotating designs include disk reactors that rotate perpendicular to the ground with scaffolds anchored to the center tube³²⁵. Perfusion reactors are designed to force fluid through the porous matrix³²⁶. They come in a variety of configurations including hollow fiber and radial perfusion systems³²⁷. Some anchor the scaffold material to frames and place several immobilized scaffolds into the fluid flow³²⁸. Other designs allow the scaffold to be free floating adjust the flowrate to keep the scaffold suspended in the fluid

column³²⁹. Perfusion reactors may also be built in a parallel plate configuration where the walls of the reactor constrain the scaffold and force the flow through the porous matrix³¹⁸.

To better understand the effect of fluid flow during tissue regeneration, a number of studies using computational fluid dynamics (CFD) have been performed^{325, 330-334}. The majority of these studies assess the flow patterns and shear stresses either within the bioreactor or around the porous construct^{325, 335}. Additionally, some studies do not account for porosity or transport through the scaffold. They treat the scaffold as an impermeable solid instead of a porous region^{325, 336}.

Flow characteristics are analyzed using either Darcy's equation³³⁷, or the Brinkman equation which is considered as an extension of Darcy's equation³³⁸. The Brinkman equation accounts for both viscous and drag forces in the porous medium and reduces to either the Navier-Stokes equation or Darcy's law if either force becomes dominant³³⁹. However, porous characteristics change during tissue regeneration, i.e., permeability of the matrix decreases due to decreased pore size. Further, many tissues (for example cartilage and bladder) have a high aspect ratio (large surface area relative to the thickness of the matrix).

The non-ideal fluid distribution is characterized using the residence time distribution (RTD). The RTD measures the amount of time different molecules present in the fluid spend within the reactor^{340, 341}. In other words, RTD is a measure of dispersal of a molecule in a flowing medium owing to the combined action of a velocity profile and molecular diffusion. Understanding these characteristics is important in designing the reactor shape and optimizing the location of the inlets and outlets.

This study utilized a well understood perfusion reactor with a parallel plate configuration^{5, 342} and evaluated the effect of porous structure in the flow domain. The parallel plate reactor with three different inlet and outlet conditions was simulated using CFD packages CFX 11 (ANSYS Inc, Canonsburg, PA.) and/or Comsol Multiphysics 3.4 (COMSOL, Inc., Burlington, MA). Further experiments were performed to validate the simulation results. These results show significant increase in pressure drop when the porous characteristics are modified.

5.2. Materials and Methods.

5.2.1. Sources of Materials

Chitosan with >310 kDa MW and 85% degree of deacetylation, glucose, sodium bicarbonate, Dulbecco's modified Eagle medium (DMEM), and glacial acetic acid were obtained from Sigma Aldrich Chemical Co (St. Louis, MO). Ethanol (200 proof) was obtained from Aaper Alcohol and Chemical Company (Shelbyville, KY). All other reagents were purchased from Fisher Scientific (Waltham, MA).

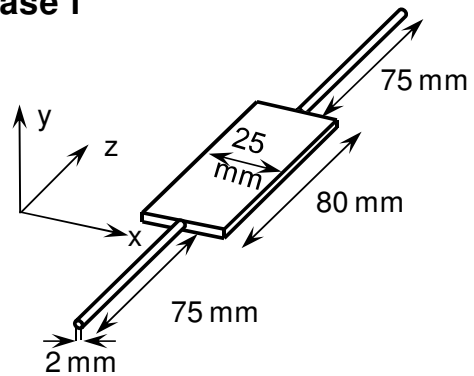
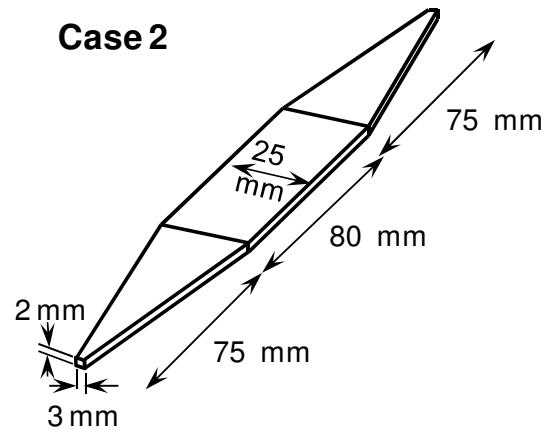
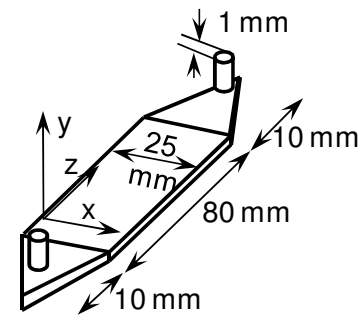
5.2.2. Obtaining RTD function using CFD:

One basic reactor geometry was used (8 cm long, 2.5 cm wide, and 0.2 cm high, with a 0.1 cm inlet and outlet diameter). For each shape, three inlet and outlet configurations (**Figure 24**) were chosen to understand the effect of inlet and outlet locations and design on flow patterns.

Case 1: with abrupt inlet and outlet to demonstrate non-ideal mixing.

Case 2: with long entrance and exit section to facilitate fully developed laminar flow.

Case 3: with inlet and outlet from the top. This configuration is commonly used in a variety of cell studies such as shear effect on endothelial cell, neutrophil sequestration, and long term bone marrow cultures^{5, 343}.

Case 1**Case 2****Case 3****Figure 24. Schematic of reactor designs utilized in this study showing major dimensions**

These reactor geometries were created using a CAD package (SolidworksTM or ANSYS Workbench 11). The CFX mesh was then created using ANSYS CAD2Mesh software. A critical challenge was overcoming problems associated with the aspect ratio i.e., very large surface area relative to the thickness of the channel. To ensure at least 10 nodes over the thickness of the reactor, the maximum element size of 0.2 mm was chosen.

Preliminary simulations used a water mass flowrate that corresponds to the average wall shear stress present in human blood vessels, 2.6 g/s (156 mL/min)⁵. Flow rates of 0.33 g/s (20 mL/min) and 0.0825 g/s (5 mL/min) were used for later simulations and experimental validation because higher flowrates compressed the porous structure. The simulation was run at steady state in order to visualize flow distributions and to generate the initial velocity profile for transient simulations. The outlet was set at atmospheric pressure and the walls were smooth with no slip condition.

Residence time distributions (RTDs) were obtained by introducing a tracer into the reactor feed starting at time equal to zero seconds. The tracer for the simulations was created as a duplicate fluid based on water and then renamed as tracer. This created a tracer with the same physical properties as that of water. The tracer was introduced as a step change in the concentration (represented as C_0). The values for steady state flow of water were used as initial conditions. Then, the inlet fluid was switched from 100% water to 100% tracer at time equals zero seconds. The simulations were run using 0.05 s time-steps until the concentration of tracer was at least 0.98 (300 steps, 15 s), with transient results written every 0.1 s. The RTD is obtained by applying a step change in the concentration of a tracer flowing into the reactor (represented as C_0) and evaluating

the temporal volumetric flow-averaged tracer concentration at the reactor outlet. The dimensionless mixing cup (or volumetric flow-averaged) tracer concentration ($C_{mix}(t)$) across the rectangular reactor outlet was evaluated using the equation ³⁴¹

$$C_{mix}(t) = \frac{\sum C_{avg} V_{avg} \Delta x \Delta z}{\sum V_{avg} \Delta x \Delta z} \quad (5)$$

where C_{avg} is the average tracer concentration across between two finite elements and V_{avg} is the average velocity in the z -direction between those elements. $C_{mix}(t)$ is also measured tracer concentration from the experiments at a given time when collecting samples at the reactor exit. Next the RTD function, $E(t)$, was calculated for a positive step change in the tracer concentration using the equation ³⁴⁰

$$E(t) = \frac{d}{dt} \left[\frac{C_{mix}(t)}{C_0} \right]_{Step} \quad (6)$$

Additionally, the RTD function was converted to dimensionless time (Θ) in order to directly compare multiple geometries and flow rates. The dimensionless form of the equation ($E(\Theta)$) was calculated using the equation

$$\Theta = \frac{t}{\tau} \quad (7)$$

where τ is the space time of the reactor i.e., the ratio of the volume of the reactor to volumetric flow rate.

5.2.3. Obtaining RTD using experimental setup.

The RTD function was determined experimentally by introducing a red food dye as a step change in the inlet concentration. A rectangular reactor similar to Case 3 (length of 8 cm, a width of 2.5 cm, a height of 0.2 cm, and a 0.1 cm inlet and outlet diameter) was fabricated in-house from polycarbonates as shown in **Figure 25A** and **Figure 25B**. The effective length and width of the reactor was based on the size of a standard microscope slide, and the height was based on the thickness of a porous matrix commonly used in our laboratory ¹⁶. The reactor's height and hexagonal flow field were maintained using a 2mm thick Teflon gasket.

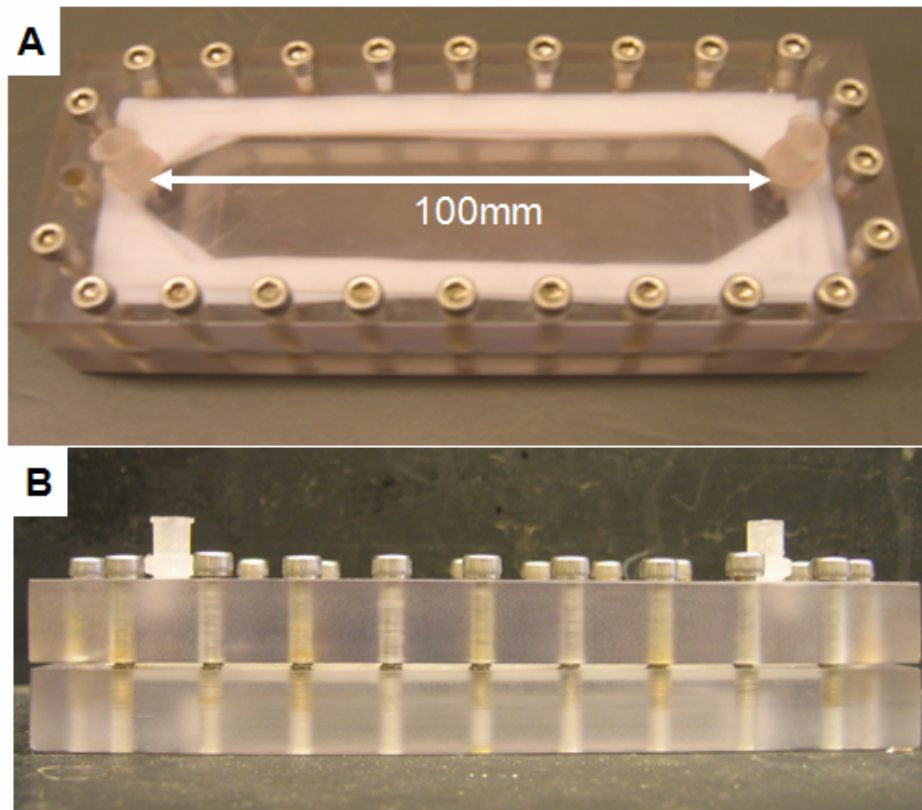


Figure 25. Reactor set-up used in experimentation.

(a) Top view of the rectangular reactor. (b) Side view of the rectangular reactor.

The reactors were attached to a flow system consisting of two fluid reservoirs, a variable speed Masterflex L/S peristaltic pump (Cole-Parmer, Vernon Hills, IL), an in-line physiological pressure transducer (Capto SP844, Capto, Skoppum, Norway), the bioreactor, and two waste reservoirs (**Figure 26**). The pressure transducer was connected to a computer via Powerlab/4SP System (ADI Instruments, Inc., Colorado Springs, CO) and data were acquired through Chart™ 5 for Windows. The tubing system for the reactor was designed in order to produce a step change in the reactor's inlet concentration. Two separate tubes were run through a peristaltic pump, one from a water reservoir and another from a reservoir filled with dye tracer solution. These tubes each led to a three way stopcock (V1 and V2) that would send the fluid either towards the reactor or into a waste reservoir. The two sides were connected by a T-joint, allowing dye solution or water to enter the reactor.

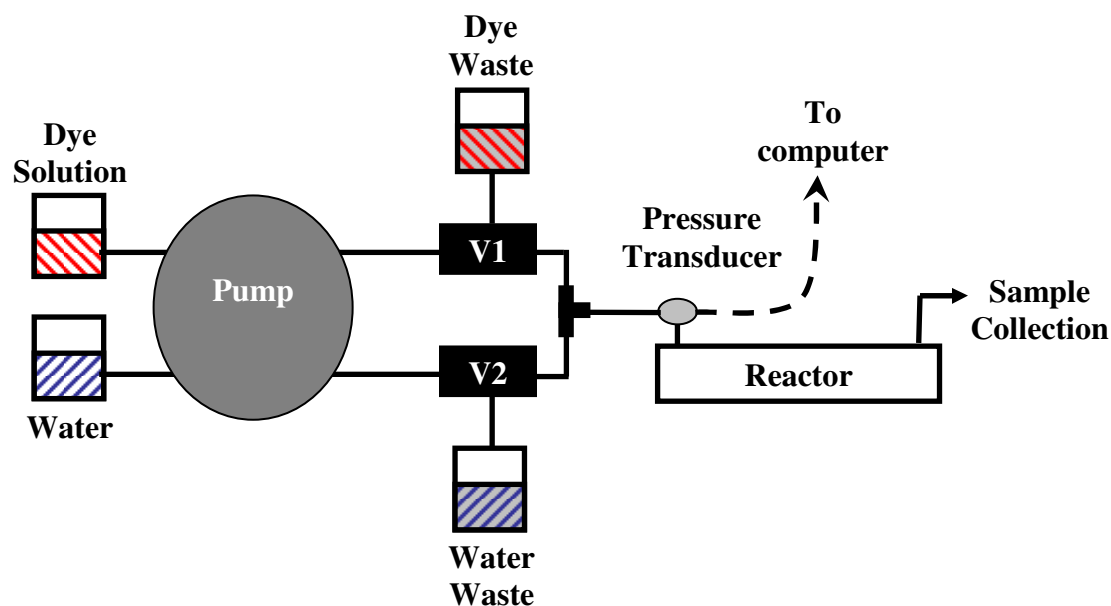


Figure 26. Flow system used in reactor experiments.

Initially the flow loop was primed with the valve positions (V1 to dye waste and V3 to reactor) set so as the water traveled through the reactor while the dye solution was sent to a waste container. Water was run through the system for until steady state was obtained. At time zero, V1 and V3 were changed simultaneously (V1 to reactor and V3 to water waste) so the dye solution traveled through the reactor and water was sent to the waste container. Fractions were collected in a 24 well plate at the reactor outlet over regular intervals. Next 100 μ L of each fraction was transferred to a 96 well plate and the absorbance was measured at 490nm; initial spectral scan over visible spectra showed that the maximum absorbance was at 490 nm wavelength. The relative concentration ($C(t)/C_0$) was calculated from the relative absorbance (A/A_0)

$$\frac{C(t)}{C_0} = \frac{A(t)}{A_0} \quad (8)$$

where A_0 is the initial concentration of the dye solution. The RTD function ($E(t)$) was calculated using Equation 6 as before. Since 20mL/min flowrate compressed the porous scaffold structure, 5mL/min was used. For the rectangular reactor 20mL/min fractions were collected over 1 s intervals, and fractions for the 5 mL/s flow rate were collected over 5 s intervals.

5.2.4. Analytical Model Derivation.

The RTD function for an ideal completely developed laminar flow with no slip at the boundaries was derived as another method of verifying simulation data for rectangular reactor³⁴⁰. The reactor was modeled as a set of parallel plates with a width (w) and a height (h)³⁴⁴. Side and end effects were ignored with the assumption of

completely developed laminar flow profile in the y-direction (direction of the reactor height). The velocity in the z-direction was calculated from the volumetric flowrate (see Appendix 1 for detailed derivation of the equation).

$$V_z = \frac{3v_0}{2wh} \left(1 - 4 \frac{y^2}{h^2} \right) \quad (9)$$

The final external age distribution expression is

$$E(t) = \frac{\tau^2}{6t^3} \left(1 - \frac{2\tau}{3t} \right)^{-1/2} \quad (10)$$

The minimum residence time was calculated from the maximum velocity equation

$$t_{\min} = \frac{L}{V_{\max}} = \frac{L}{\frac{3}{2}V_{\text{avg}}} = \frac{2Lwh}{3V_{\text{avg}}wh} = \frac{2\tau}{3} \quad (11)$$

$$E(t) = 0, t < \frac{2\tau}{3} \quad (12)$$

$$E(t) = \frac{\tau^2}{6t^3} \left(1 - \frac{2\tau}{3t} \right)^{-1/2}, t \geq \frac{2\tau}{3} \quad (13)$$

Eq. (12) and Eq.(13) were used to generate E(t) curves for the ideal case.

5.2.5. Preparation of porous structure.

Porous structures of dimensions appropriate for each reactor were generated by freezing 0.5% (wt/v) chitosan solution prepared in with 0.1 M acetic acid at -80°C, then lyophilized overnight (Virtis, Gardiner, NY). The porosity and pore size distribution of these matrices in hydrated condition has been extensively characterized in our laboratory^{5, 14, 112}. Scaffolds were stabilized in 100% ethanol and incubated in red-dye prior to use in experiments. The pore size distribution and porous structure characteristics of the wet scaffolds were analyzed using light microscopy. Prior to viewing under light

microscopy, chitosan structures were sectioned to view cross sectional architecture. Pore size and number of pores was determined from digital micrographs using Sigma Scan Pro software (Systat Software, Inc., Point Richmond, CA).

5.2.6. Simulation including the porous structure.

Next, a porous medium was created within the reactor space to better understand the effect of porous structure on fluid flow, simulations were performed using COMSOL Multiphysics 3.3 (COMSOL inc, Burlington, MA). Both the case 3 and case 6 geometries were created in COMSOL using configurations identical to described above. Fluid flow through the porous structures was modeled using the Brinkman equation

$$\mu \nabla^2 u_s - \frac{\mu}{\kappa} u_s = \nabla p \quad (14)$$

$$\nabla \bullet u_s = 0 \quad (15)$$

where κ is the permeability of the porous medium, u_s denotes the fluid superficial velocity vector, p is the fluid pressure, μ the effective viscosity in the porous medium, and κ is the permeability of the porous medium³⁴⁴. Nonporous sections of the reactor were modeled as incompressible Navier-Stokes regions. The permeability (κ) of the porous medium is a geometric characteristic of the porous structure at several length scales³⁴⁴. The permeability was calculated using $85\mu\text{m}$ and 120 pores/mm^2 and the equation

$$\kappa = \frac{\pi}{128} n_A d^4 \quad (16)$$

where n_A is the number of pores per unit area and d is the pore diameter assuming the pores to be circular in shape. To understand the effect of pore size and number of pores, κ values were calculated for (**Table 3 and Table 4**) different pore sizes and pore numbers. These values were used in the simulation. Shear stresses within the reactor were calculated using the shear stress tensor .

$$\tau = \eta \left(\nabla u + (\nabla u)^T \right) \quad (17)$$

where η is the dynamic viscosity (Pa·s) and u is the velocity in the open channel (m/s). The shear stress tensor is an integral part of the Navier-Stokes equations describing flow in a free channel, at steady state, given by

$$\rho(u \bullet \nabla)u = -\nabla \bullet (-\tau + p\delta_{ij}) \quad (18)$$

$$\nabla \bullet u = 0 \quad (19)$$

where η is the dynamic viscosity (Pa·s), u refers to the velocity in the open channel (m/s), ρ is the fluid's density (kg/m³), δ_{ij} is the Kronecker delta function, and p is the pressure (Pa). Both the permeability (κ , m²) and void fraction (ε_p , dimensionless) were incorporated into Equation 18 in order to account for the porous characteristics of the matrix, yielding another form of the Brinkman Equation

$$\frac{\eta}{k} u = \nabla \bullet \left(\frac{-\tau}{\varepsilon_p} + p\delta_{ij} \right) \quad (20)$$

The simulation was run at 5 mL/min (similar to experiments), with atmospheric pressure as the outlet condition. From the steady state output results, the pressure drop and the maximum shear stress were determined across the porous subdomain. Further, the

shear stress was visualized as the viscous force per area in the z direction, as calculated by Equation 21.

$$\tau \bullet n \quad (21)$$

Table 3. Effect of pore size and pore number on pressure drop and shear stress.

Pore Size (μm)	Pores/ mm ²	k (μm ²)	Pressure Drop (kPa)	Maximum Shear Stress (dyne/cm ²)
10	1500	0.368	238	0.228
17.5	1050	2.42	36.4	0.227
25	600	5.75	15.2	0.227
37.5	450	21.8	4.02	0.224
50	300	46	1.91	0.220
85	120	154	0.57	0.207
120	60	305	0.287	0.192
150	35	435	0.202	0.181
200	15	589	0.149	0.171

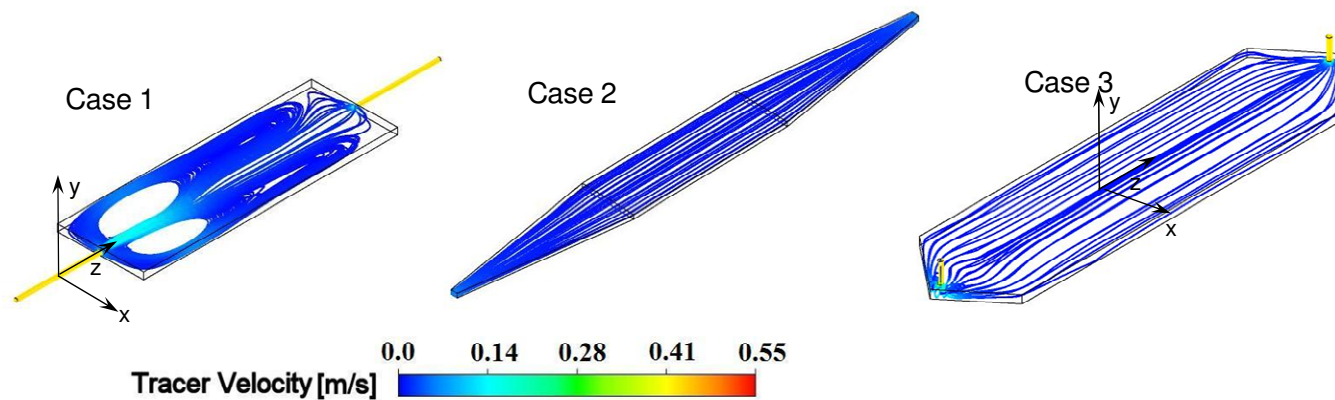
Table 4. Effect of reduced pore size with constant pore number on pressure drop and shear stress.

Pore Size (μm)	Pores/mm ²	k (μm ²)	Pressure Drop (kPa)	Maximum Shear Stress (dyne/cm ²)
85	120	154	0.57	0.207
50	120	18.4	4.76	0.225
37.5	120	5.82	15.1	0.227
25	120	1.15	76.2	0.228
17.5	120	0.276	318	0.228
10	120	0.0295	2970	0.228

5.3. Results and Discussion.

5.3.1. *Steady state profile in unpacked reactors.*

First, the streamline patterns for water flowing through the reactor without porous structures were analyzed in all the reactors at steady state. For individual reactor cases, no significant difference in the streamline patterns was observed between 156 mL/min and 20 mL/min flow rates. However, different reactor geometries showed significantly different streamline patterns. In case 1 (**Figure 27A**), a number of recirculation zones were observed through out the reactor. This could lead to a large dead volumes and a random orientation of cells. Case 2 (**Figure 27B**) showed completely developed flow pattern without any recirculation in the entire length of the reactor. In case 3 (**Figure 27C**), recirculations were observed at the entrance of the reactor but the majority of the reactor shows laminar streamlines. Differences in the flow distribution as a result of increased flowrate can be seen in **Figure 28**.



110 **Figure 27. Steady state stream line profiles in different reactors simulated with a flow rate of 20mL/min.**

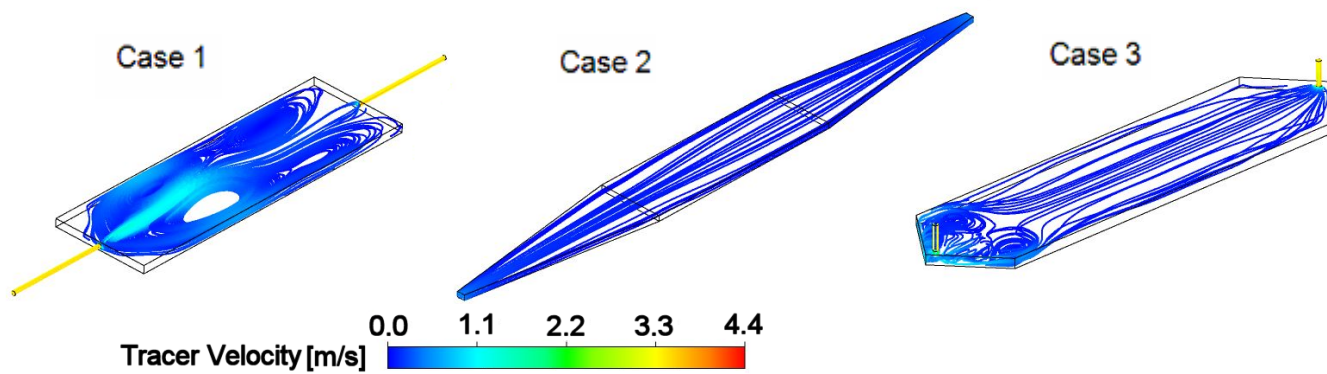


Figure 28. Steady state stream line profiles in different reactors simulated with a flow rate of 156 mL/min

5.3.2. Residence time distributions without porous structure

Transient residence time distributions for the tracer were analyzed at the reactor outlet to better understand the flow distribution of nutrients. First, the changes in the tracer concentration across the outlet diameter were examined so that a method to determine $C_{mix}(t)$ from the simulation results could be developed. For this purpose, tracer concentration across the reactor outlet was plotted (**Figure 29**). Examination of these results showed that for 1 mm outlet diameter, the tracer concentration was virtually linearly distributed over the cross section area. Examination of the tracer concentration at the reactor exit showed that case 1 had a relatively constant outlet concentration at each time point. Similarly, case 2 also showed flat concentration profiles. Initial and final concentration profiles were flat in case 3 at the initial time points which changed to linear variation across the outlet before reaching a flat profile. However, it only took about one second for a complete changeover from water to tracer. This suggested that for rectangular reactors approximating $C_{mix}(t)$ using Equation 5 is valid.

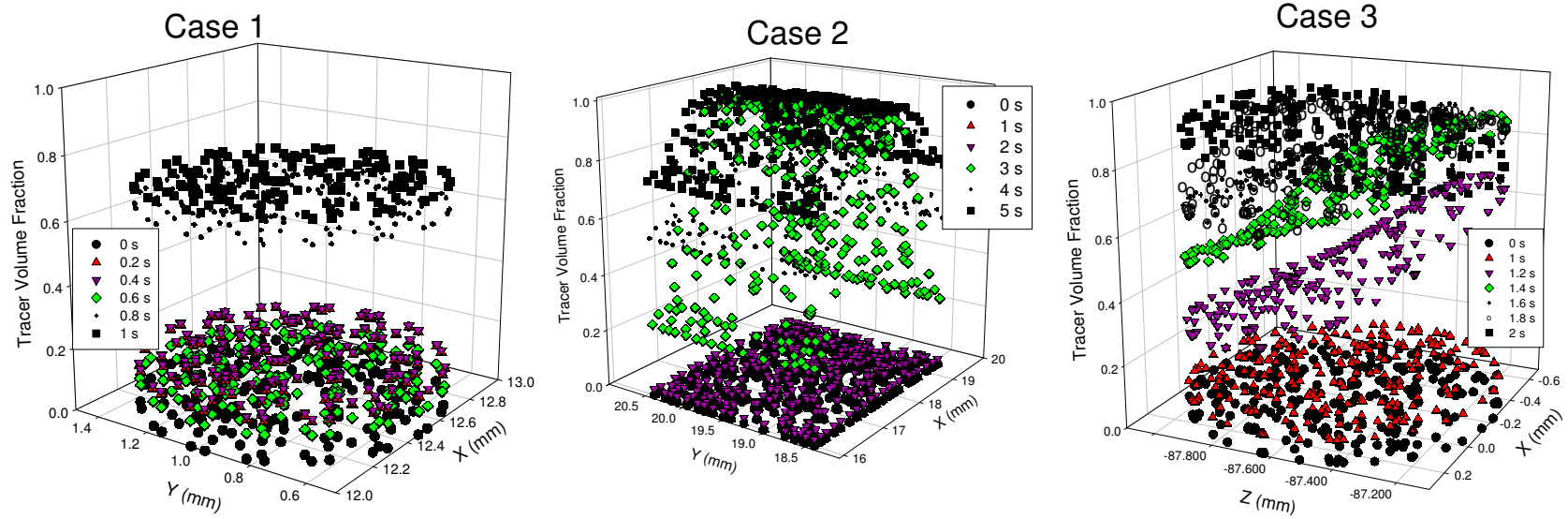


Figure 29. Concentration profiles at the reactor outlet for different times at the 20 mL/min flowrate.

The relative concentration (C_{mix}/C_0) was plotted against dimensionless time (**Figure 30A** and **Figure 30C**). In case 1 and case 4 the tracer exited the reactor much sooner than in other geometries. This premature exit of the tracer could be attributed to the dead volume or channeling. Next, $E(t)$ was calculated for different time steps and plotted as a function of dimensionless time (**Figure 30B** and **Figure 30D**). All rectangular reactor peaks except case 1 aligned as expected at $2/3^{\text{rd}}$ the ideal space time. Additionally, peak spreading was observed in case 1, case 2, and case 3 indicating dispersion of the tracer or flow non-idealities. Further, $E(t)$ peak heights for case 1 and case 3 were higher than case 2. These observations suggest that there are dead-spaces within the reactor in case 1 and case 3. The simulation results for case 3 were validated by experiment. The simulations and experiments had similar concentration and RTD profiles when plotted, showing that methodology is a valid approach to analyze flow properties in the reactor systems.

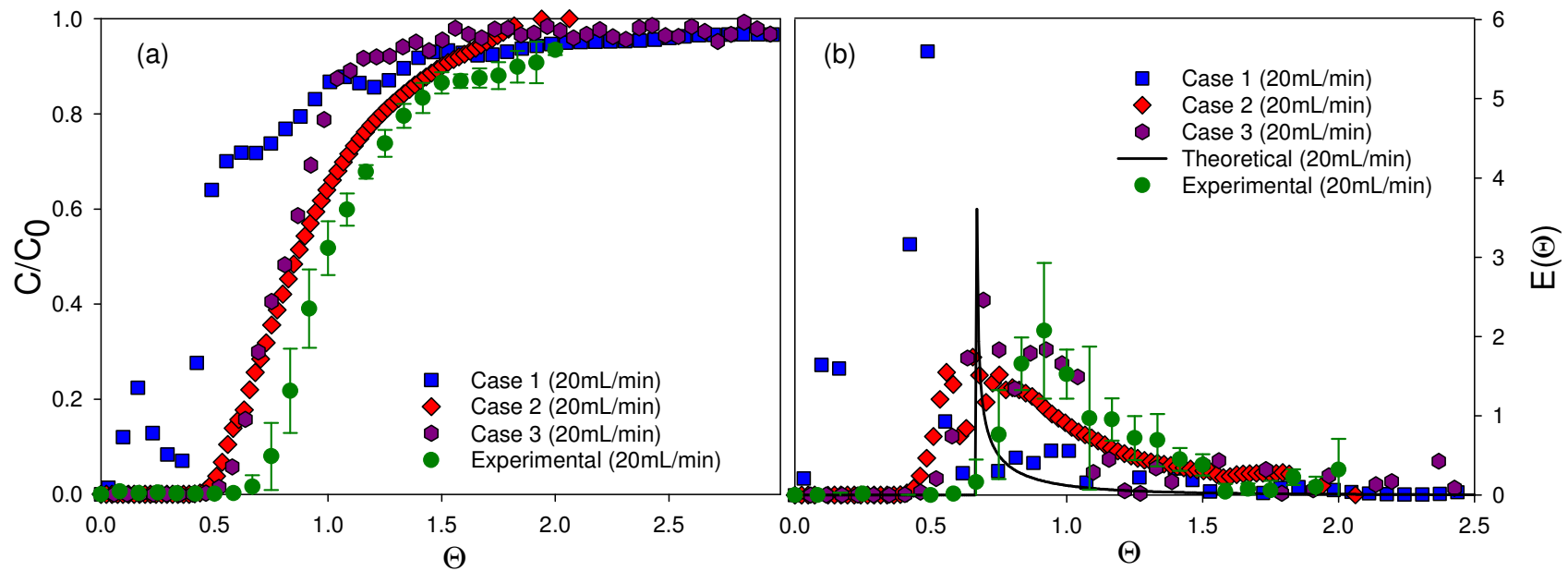


Figure 30. of reactor shape on the residence time distribution of the tracer at 20 mL/min.

a) Concentration of the tracer at the outlet of rectangular reactor. b) E-curve for rectangular reactor.

5.3.3. Effect of porous structure on flow distribution.

This study utilized chitosan porous structures prepared by freeze drying at -80°C . Chitosan was selected because i) it is optically transparent, enabling visual monitoring of the flow distribution, ii) the matrix will not degrade in the absence of enzymes, iii) its mechanical properties are well described, and iv) pore characteristics of the scaffold have been analyzed extensively^{5, 14, 112}. Scaffolds formed by freezing at -80°C showed an average pore size of $85\text{ }\mu\text{m}$ ($\pm 20\text{ }\mu\text{m}$), 120 pores per mm^2 , and a porosity of 85%. Porosity values were used to calculate the available reactor volume and space time.

When RTD was examined for reactors containing the porous structure, results indicated (**Figure 31**) that the tracer exited the reactor sooner relative to conditions without the porous structure. This could be attributed to the increased resistance to flow caused by the presence of the porous structure which could favor channeling. When fluid entered the system, the hydrodynamic forces deformed the polymer scaffold, creating a shorter path to the outlet of the reactor. While performing experiments, it was observed that the scaffolds were compressed near the inlet and the flow traveled over the top of the matrix and along the walls without significantly infiltrating into the porous structure. This bypass effect was minimized by providing space for entry and exit effects, thereby ensuring that the flow entered the porous structure instead of bypassing it.

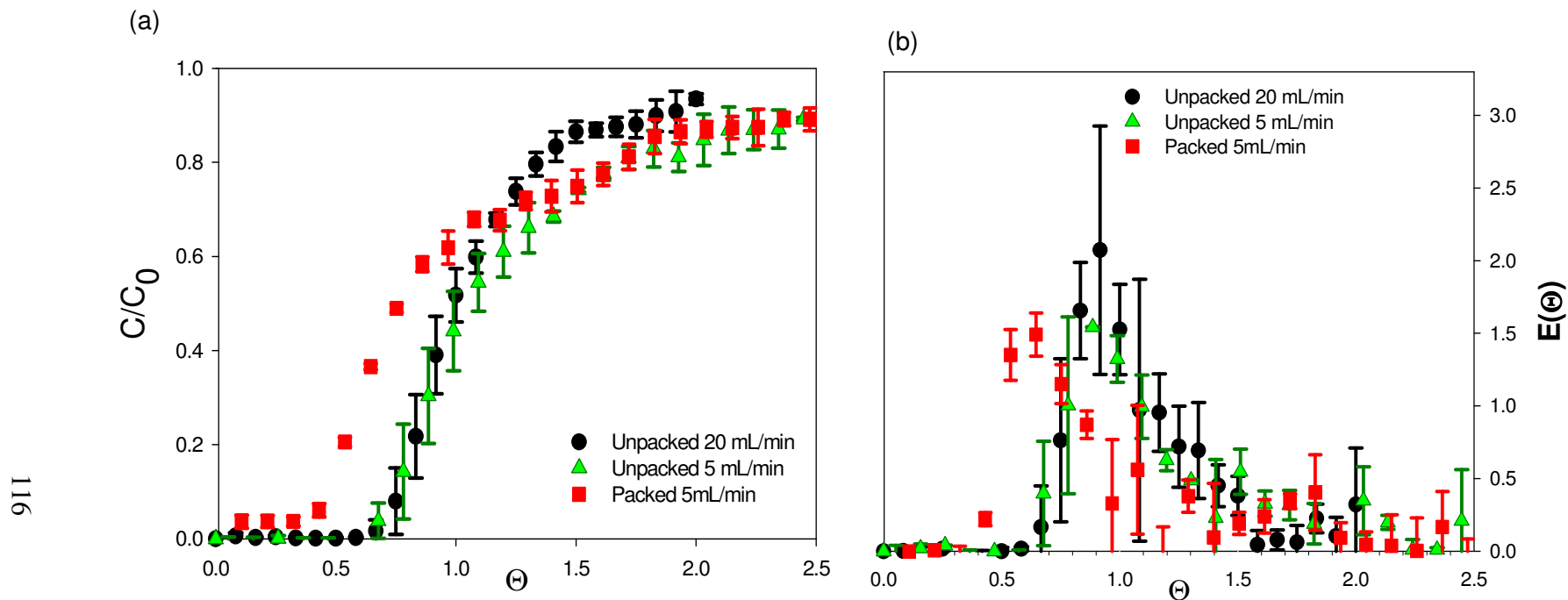


Figure 31. Effect of flow rate and porous structure on the residence time of the tracer.

a) Concentration of the tracer at the outlet of rectangular reactor. b) E-curve for rectangular reactor.

5.3.4. Effect of changing pore sizes.

Next, the pressure drop across the reactors and the shear stresses developed within the porous structures were assessed. When fabricating scaffold the number of pores and the pores per area do not change independently. For example, a matrix with smaller pores should have more pores in any given area than a scaffold with larger pores. Therefore, simulations were performed using various pore sizes and pores per area to better understand the effects of the porous architecture. Values for pore size and pores per area were centered on an experimentally determined value (85 μm diameter pores and 120 pores/ mm^2) (**Table 3**). These results showed significant changes in the pressure drop across the bed for rectangular reactors. The pressure drop increased when the pore size was reduced, and increased when the number of pores per unit area (pores/ mm^2) was increased. Additionally, the pressure drop was inversely proportional to $1/\kappa$ as predicted by the Brinkman equation (**Equation 14**). The experimentally measured pressure drop within the reactors was slightly higher than pressure drop predicted by the simulation. The pressure drop at the 5 mL/min flowrate was 2-5 mmHg (0.267 –0.667 kPa), which agreed with the simulation value.

In the rectangular reactors (**Figure 32**), the shear stress increased in a linear fashion as the pore size decreased, but that the shear stress increased exponentially as the pore density (pores/mm²) increased settling on a value of 0.228 dyne/cm². Flow within the rectangular reactor was in the *z* direction only; therefore, shear stresses for the rectangular reactor occurred in the *z* direction.

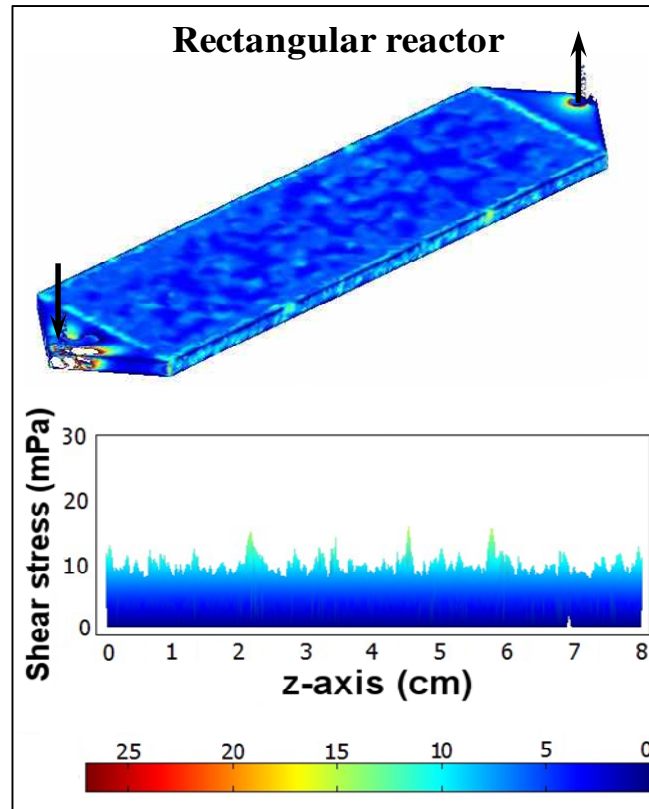


Figure 32. Shear stresses within the porous structure for the case with 85 μm pore size and 120 pores/mm². Arrows indicate the flow direction.

5.3.5. *Effect of changing porosity.*

During the course of tissue remodeling, cells will proliferate and *de novo* synthesize extracellular matrix elements which are deposited in the porous structures. These processes reduce the pore space available for fluid flow. Hence the pore size decreases but the number of pores per area does not. To understand the implications of these dynamic changes, simulations were carried out with six decreasing pore sizes (**Table 4**) but using the number of pores per unit area that was determined experimentally (120 pores/mm²). These results showed significant increase in the pressure drop across the bed with decreased pore size.

5.4. DISCUSSION.

In this study, simulations and experimental validation were performed with and without porous structures to understand the fluid flow distribution within the bioreactor. The rectangular reactor used in this study has been widely utilized in various studies including long term bone marrow cultures³⁴⁵, atherosclerosis and endothelial function⁵, homing and rolling of immune cells and liver-assist bioreactor^{346, 347}. The reactor systems used have distinct advantages for regenerating large clinically transplantable tissues such as cartilage, bladder and skin; scaffolds can have very large surface area to volume ratios with very small thickness. Another popular bioreactor configuration involves growing cell seeded constructs in microgravity³⁴⁸. However, for growing large aspect ratio tissues, microgravity reactor would deform the structure due to bending and rolling while tumbling through the growth medium, creating a random stress pattern within the developing material. Hence, microgravity reactors may not be suitable for regenerating thin cross-sectional tissues. The parallel plate reactors provide stability and

support for the porous structure and developing tissue.

Further, the experimental results showed compression of the porous structure at 20 mL/min flowrates. The compression can be attributed to the mechanical properties of the chitosan porous structure (elastic modulus is 2-6 kPa). To minimize the compressive damage on the porous structure, flow rate was reduced to 5 mL/min. However, in the simulation results, these compressive changes were not considered and the porous medium was treated as a rigid matrix. Hence, further studies in which the elastic properties of the porous structure are coupled to the fluid force are necessary to better understand the fluid distribution.

Understanding pressure drop changes is important to determine the pressure to be maintained during tissue regeneration³⁴⁹. To mimic tissue regeneration process, the number of pores was kept constant while decreasing the pore size. The exponential increase in pressure drop as pore sizes shrink indicates that liquid flow through a porous scaffold will decrease and possibly stop unless flow system is adjusted to provide large pressure gradients. The nonlinear properties of both shear stress distributions and pressure drop suggest that there is room for optimization of the porous structure. Others have reported the effect of changing porous structure due to cell growth on the growth media distribution in cylindrical scaffolds³³⁸. These studies used porosity based permeability values, which could change by either decreased number of pores or decreased the pore size. Hence, it may not reflect the true regeneration characteristics.

While the scaffold is subjected to the bulk forces supplied by the tissue and fluid flow, the cells experience the micromechanical properties of the individual fibers and local shear stresses within the porous structure. Flow within the reactor determines the

orientation of cells within the material. Shear stresses generated by the fluid motion influence alignment of endothelial cells⁵ and chondrocytes¹²⁵ grown in the parallel plate reactor. Alignment of cells and the de novo synthesized matrix elements determine the ultimate quality of the regenerated tissue. We evaluated the shear stresses within the porous structure through simulations. Shear stress in the porous structures are less compared to the estimated wall shear stresses³⁵⁰. The shear stress in the porous structure is $\sim 0 - 0.05 \text{ dynes/cm}^2$ in the rectangular reactor. A microgravity reactor rotating at 10 rpm has an average wall shear stress of 0.2 dyne/cm^2 and a maximum shear stress of 0.3 dyne/cm^2 ¹²³, comparable to parallel plate bioreactors. However, the tumbling free fall motion of the scaffolds produces a non-uniform stress distribution. Another method uses mechanical action to stretch or compress the scaffold material^{351, 352}. One configuration utilizes screw driven actuators to impart bidirectional stresses to the material¹²⁴. Further studies are necessary to determine the optimal method or methods for controlling the mechanical forces acting on material within bioreactors³⁵³. Cellular constructs grown *in vitro* shrink, possibly as a result of cellular attachment and contraction or as a result of hydrodynamic forces compressing the scaffold.

Non-ideal fluid flow patterns lead to non-uniform distribution of nutrients present in the fluid. The RTD analysis is independent of the metabolic reactions and hence nutrient consumption is not integrated into the CFD modeling. To understand the implications of non-ideal flow on tissue regeneration, nutrient transfer characteristics have to be analyzed. Nutrient transport and consumption can be investigated through use of the reactions package. Flow rates must be optimized based on i) nutrient distribution, ii) effect on assembly of matrix elements, and iii) cellular response to local shear stress.

Chapter 6

Modeling Oxygen Transport within Porous Matrices

6.1. Introduction

As described in the previous chapter, bioreactors are used to encourage 3D cell growth and colonization by using a direct perfusion system to supply a continuous flow of nutrients. The upper limit for the perfusion rate is set by the tolerance of cells to shear effects induced by the flowing fluid. The lower limit is set by the metabolic demand for nutrients of each cell type. The flowrate through the reactor controls the concentration of nutrients such as oxygen and glucose. Therefore, by studying both the flow properties through the porous matrix and consumption of nutrients within the system an upper and lower range can be determined for bioreactor optimization.

One of the main ways cells change their local microenvironment is through cellular respiration, the process where cells consume oxygen and nutrients and produce carbon dioxide, waste, and energy. One cause of failure in tissue engineering structures is hypoxia, a lack of oxygen in the center of the scaffold. Before new microvasculature has formed, cells within the scaffold are dependent upon the flow and diffusion of oxygen for survival. Therefore it is important to study the oxygen transport across the scaffold. Further, glucose was used because of its importance in cellular metabolism. Glucose is used as a cellular energy source and plays a central role in various disease states such as diabetes³⁵⁴.

In order to combat this problem, the role of oxygen transport has been explored in a variety of bioreactor configurations. There are several ways to experimentally monitor the dissolved oxygen level in the fluid using either fluorescence quenching^{355, 356} or electrochemical reduction^{357, 358}. Work has also been done simulating cell growth in gas sparged and agitated vessels that do not contain porous structures³⁵⁹. Shear stresses have also been investigated both computationally and experimentally using parallel plate bioreactors with micron scale surface topography³⁶⁰. Both consumption of oxygen and shear stresses for bone tissue engineering have been explored as a 2D computational model³⁶¹. The concentration of oxygen in rotating wall vessels which utilize nonporous micro-carrier beads as cellular supports has also been studied using at a variety of conditions³⁶². Other models have been developed to study the cell population dynamics and oxygen consumption within porous matrices. However, the population models do not account for the effect of fluid flow and shear stress in directing cellular growth and attachment, or changes in the 3D porous structure due to cell proliferation, extracellular matrix production, and matrix turnover^{363, 364}. The main drawback to these studies is that they use small structures with limited porosity. Currently there is limited understanding of the transport phenomena in large porous structures with a high aspect ratio.

It is important to understand the processes that occur within the porous matrix as the tissue regenerates. Understanding the regeneration process is especially important in high aspect ratio reactors, similar to configurations described in Chapter 5. The goal of this work is to determine a minimum flowrate required to provide adequate nutrients to the cells seeded within the porous matrix housed in the parallel plate reactor. Therefore, the effects of cellular metabolism on both oxygen and glucose concentrations within the

matrix were added to the simulations developed in Chapter 5. While performing simulations, metabolic consumption for both oxygen and glucose was included using kinetic rate laws. The rate law was defined in the COMSOL simulation, enabling the visualization of both the oxygen and glucose profiles within the porous structure. Additionally, the simulation data was used to determine appropriate flowrate for an optical profiler system, developed in-house to visualize oxygen profile across the bioreactor. These results show different minimum flow rates for different cell types and the potential use of oxygen profiler.

6.2 Materials and Methods

6.2.1. Sources of Materials

Chitosan with >310 kDa MW and 85% degree of deacetylation, glucose, sodium bicarbonate, Dulbecco's modified Eagle medium (DMEM), and glacial acetic acid were obtained from Sigma Aldrich Chemical Co (St. Louis, MO). Ethanol (200 proof) was obtained from Aaper Alcohol and Chemical Company (Shelbyville, KY). Human foreskin fibroblasts (referred to as HFF-1 cell line) were purchased from American Tissue Culture Collection (Walkersville, MD). L-glutamine, penicillin-streptomycin, amphotericin, trypsin/EDTA, and Fetal Bovine Serum (FBS) were purchased from Invitrogen Corp. (Carlsbad, CA). All other reagents were purchased from Fisher Scientific (Waltham, MA).

6.2.2. Simulation nutrient distributions

The consumption of oxygen was simulated using the COMSOL Multiphysics software. The reaction was added to the simulation by adding a 3D convective diffusion model to the Brinkman model already in place (**Equation 14**). The convective diffusion equation was used to obtain the concentration at varying position along the cross section of the reaction:

$$\nabla \bullet (-D \nabla c) + u \bullet \nabla c = r_A \quad (22)$$

where c is the concentration of the species, r_A is the rate of reaction, D is the diffusivity of the species, and u is velocity. Additionally, the fluid system was split into multiple parts using two dependent variables in the convective diffusion model. The rate of reaction could then be entered using the reaction rate tab in the subdomain setting of the convective diffusion model. A Michaelis-Menten rate law was used for both oxygen and glucose consumption based on the reaction rates reported in the literature^{340, 365-367}. The rate law is given by the expression

$$-r_A = \frac{V_{Max} C_A}{K_m + C_A} \quad (23)$$

where r_A is the rate of reaction, V_{Max} is the maximum reaction rate, and K_m is the Michaelis constant. Two cell types, chondrocytes and smooth muscle cells (SMCs) were evaluated using rate constants shown in the **Table 5**.

Table 5. V_{Max} and K_m value for different cell types.

Cell Type	V_{Max} (mol/m ³ s)	K_m (mol/m ³)
chondrocytes ³⁶⁵	2.47×10^{-6}	6.00×10^{-3}
SMCs ^{366, 367}	3.16×10^{-5}	0.205

Flowrates between 0.01 mL/min and 0.001 mL/min were simulated to determine the appropriate flowrate where a difference in signal may be measurable experimentally. The effect of changing the porous architecture was analyzed similar to Chapter 5, using pore diameter and pores/area values from **Table 4**. Both the pressure drop and shear stress were also evaluated in the reacting simulations. Additionally, the effect of increasing the cell population on oxygen consumption was evaluated using smooth muscle cell. For this purpose, the simulation was performed by using a rate law multiplied by 2 and 4 times that of the original rate law as shown below.

$$-r_A = \frac{2V_{Max}C_A}{K_m + C_A} \quad (24)$$

$$-r_A = \frac{4V_{Max}C_A}{K_m + C_A} \quad (25)$$

These simulations were performed at two different pore sizes with the same number of pores. Only one flow rate was used per cell type. In order to quantify the change in oxygen concentration, exiting oxygen content was assessed.

6.2.4 Cell culture

Human foreskin fibroblasts (HFF-1), from American Tissue Culture Collection (Walkersville, MD), were maintained in Dulbecco's modified Eagle's medium (DMEM) supplemented with 4 mM glutamine, 4.5 g/L glucose, 1.5 g/L sodium bicarbonate, 100 U/mL penicillin-streptomycin, 2.5 mg/mL amphotericin B, and 20% fetal bovine serum (FBS). Cells were maintained at 37°C, in a 5% CO₂/95% air and fed with fresh medium every 48 h. Cells were dissociated with 0.01% trypsin / 10 mM EDTA, centrifuged, and resuspended in medium prior to cell seeding.

Cell culture procedure for the reactor experiments is shown in **Figure 33**. In brief, chitosan porous structures were prepared by pouring 20mL of 0.5% (wt/v) chitosan solution with 0.7% (v/v) acetic acid into the Teflon silicon well system described previously¹⁶, freezing at -80°C, and lyophilizing overnight. Samples were cut into 2.5 cm × 8 cm, sterilized with ethanol, rinsed twice with PBS, and placed into a sterile Petri dish. Cell growth media was added, and the scaffolds were then seeded with 450 cells/mm² (9×10^5 cells/scaffold), three times more than used in previous experiments^{5, 231}. The cells were allowed to attach and colonize the scaffold overnight, and then used for reactor experiments.

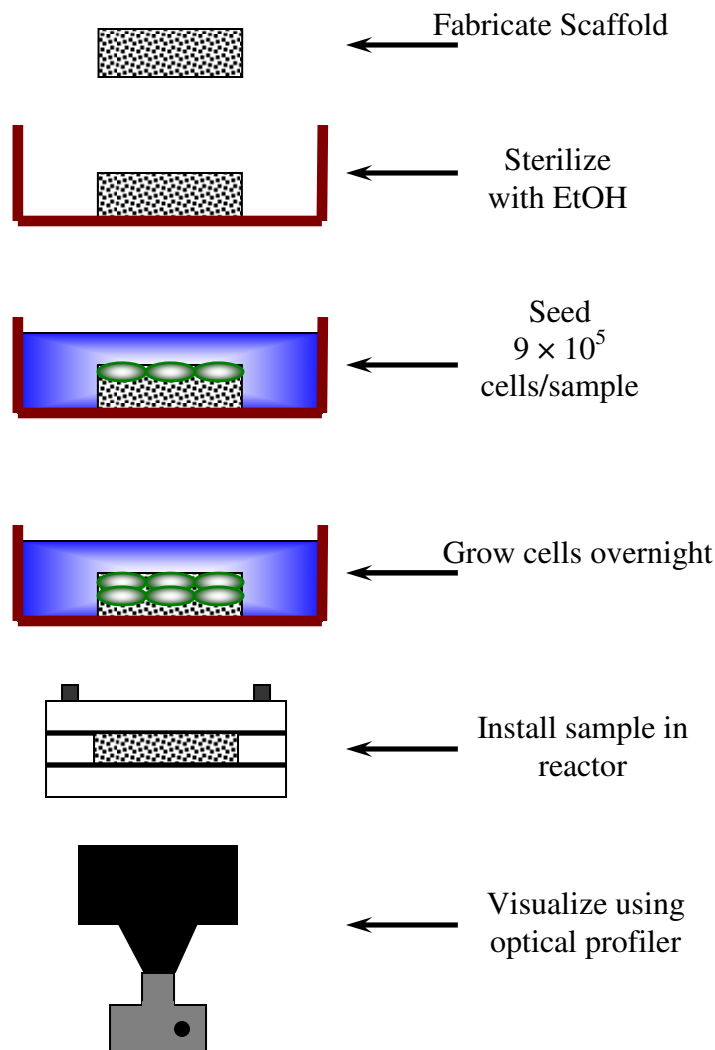


Figure 33. Cell culture technique used with the optical profiler

6.2.3. Constructing an optical profiler

The oxygen profile was visualized using an optics system developed in house. The optical profiling system is based on a glass slide coated with an oxygen sensitive material, Tris(4,7-diphenyl-1,10-phenanthroline)ruthenium(II) chloride³⁵⁶, purchased from Ocean Optics (Dunedin, FL). The ruthenium based coating is encapsulated in a sol gel matrix and thereby protected from the environment. The coating absorbs light at 470 nm (blue) and has an emission peak between 500nm and 600 nm (green to yellow). The

dissolved oxygen level in the media can then be determined because the fluorescence is dynamically quenched by oxygen. Therefore, more fluorescent signal should correlate to less oxygen present in the media³⁶⁸. The glass slide is placed in a recessed area of the bioreactor as shown in **Figure 34**. This recess allows the slide to contact the fluid flow area while maintaining a uniform height for the bottom plate of the reactor.

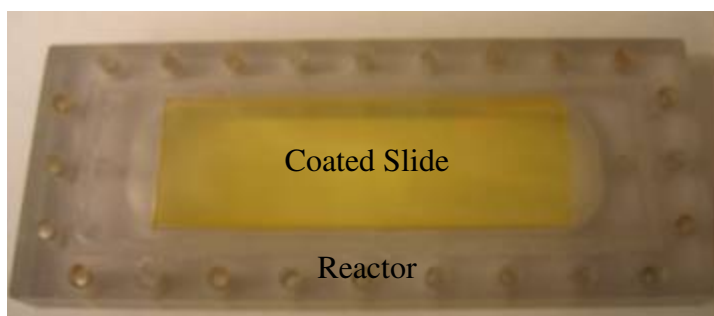


Figure 34. Coated glass slide inserted into reactor.

The reactor is then placed into an optics system shown in **Figure 35**. The system is supported on a system of interconnected round bar, and uses a 250 W Utilitech™ halogen work light (Purchased from Lowe's Home Improvement) as a light source. Light is funneled from the work light into a sealed black metal container using reflective aluminum ducting, commonly used in clothing dryer vents. As the light enters the sealed box containing the reactor it passes through a blue emission filter (Science Kit and Boreal Laboratories, Tonawanda, New York). The blue light excites the oxygen sensor and which emits fluorescence at 600nm wavelength. Next both the blue light and fluorescent emissions travel down an optical tube originally designed for a Spencer Spectrographic Camera (circa 1938)³⁶⁹. As the light exits the objective lens of the old camera optics it passes through a 515 nm excitation filter (Ocean Optics, Dunedin, FL) in

order to remove any remaining lower wavelengths, while still retaining the entire fluorescent emission spectra. The 515nm filter sits on a 90° mirror that fits nicely on the digital camera lens. The mirror redirects the fluorescent signal into a digital camera (Canon Powershot 550, Canon U.S.A., Lake Success, New York) so it can be visualized and recorded. For samples containing cells, first a 2 cm × 8 cm × 0.2 cm section of porous chitosan was prepared by freezing 0.5% chitosan at -80°C and lyophilizing overnight. The scaffolds were then seeded with 450 cells/mm² (9×10^5 cells/scaffold), three times more than used in previous experiments^{5, 231}. The reactor was then sterilized with ethanol, and the cell seeded scaffolds were loaded into the reactor. The reactor was then placed into the optics system and images were captured every 10 minutes for 1 hour using a flowrate of 0.05 mL/min. Next, the flowrate was lowered to 0.005 mL/min and images were captured every 10 minutes for another hour. To obtain such a low flowrate, 0.19mm ID microbore (Masterflex,) tubing was used. The microbore tubing was attached to the reactor inlet using silicon glue. Additionally, in order to reduce the amount oxygen leaking into the system, experiments were performed in an anaerobic chamber that had been purged with nitrogen three times.

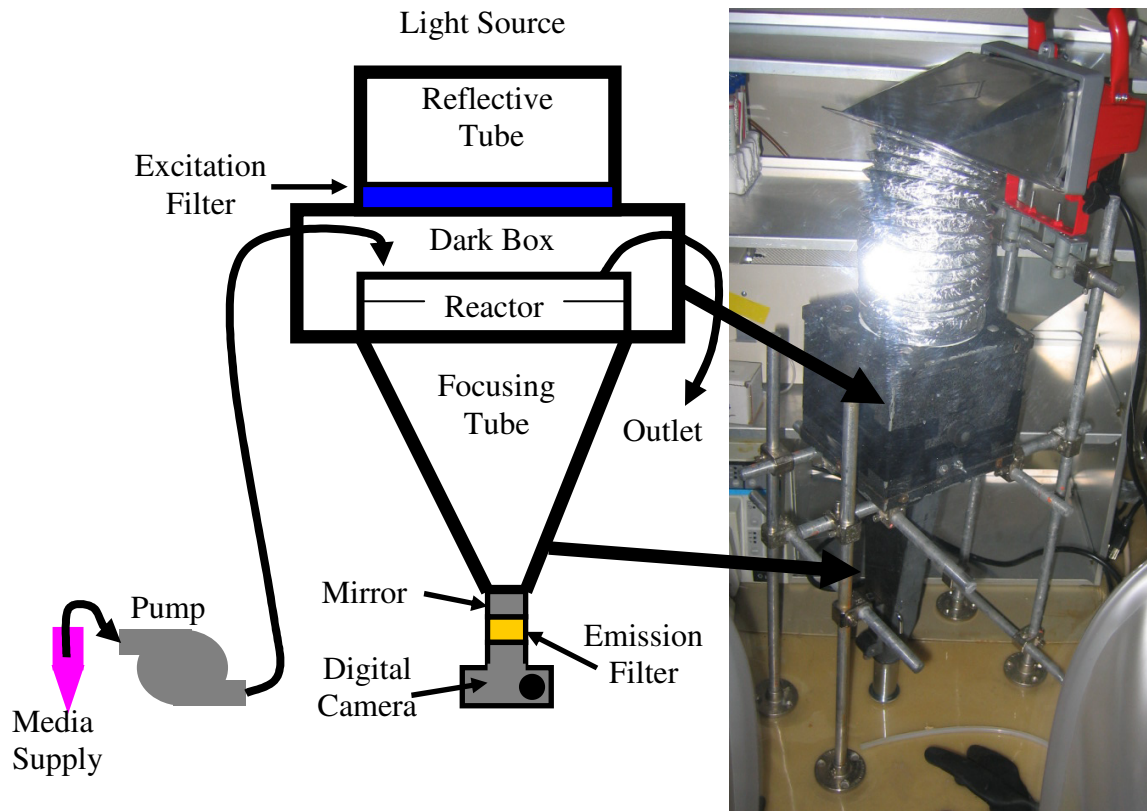


Figure 35. Diagram and photograph of the optics system.

6.3 Results

6.3.1. *Simulating oxygen profile*

Computational simulations were performed in order to determine the appropriate flowrates such that it might be possible to detect a signal from the oxygen profiling apparatus. COMSOL simulations were created using both oxygen and glucose rate law data for both smooth muscle cell and chondrocytes. Both sets of simulations were performed at the same cell density (1.2×10^{12} cells/m³). These results showed (**Figure 36**) that flowrate between 0.001 mL/min and 0.005 mL/min may have measurable oxygen profiles for chondrocytes, and flowrate between 0.01 mL/min and 0.05 mL/min may have measurable oxygen profiles for SMCs. The simulations also show that both oxygen and

glucose consumption is lower in smooth muscle cells than in chondrocytes (**Figure 37**).

The results also show that there is a difference between oxygen and glucose consumption for both cell types. Additionally, the difference in oxygen and glucose consumption is higher in SMCs than in chondrocytes.

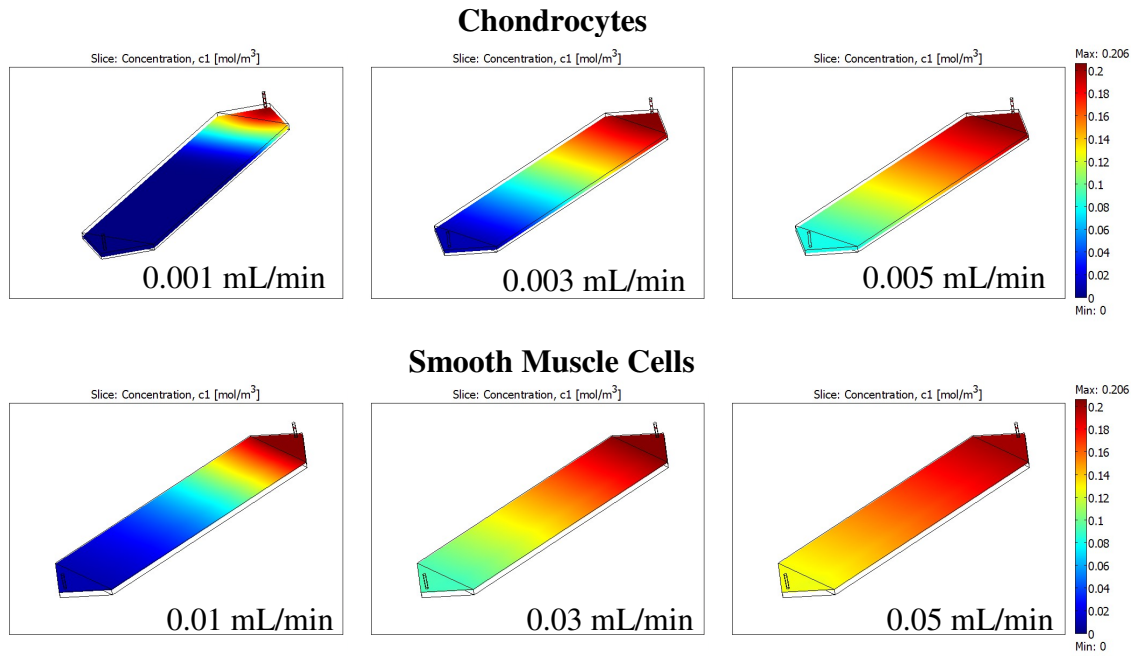


Figure 36. Simulated oxygen profiles for the rectangular reactor

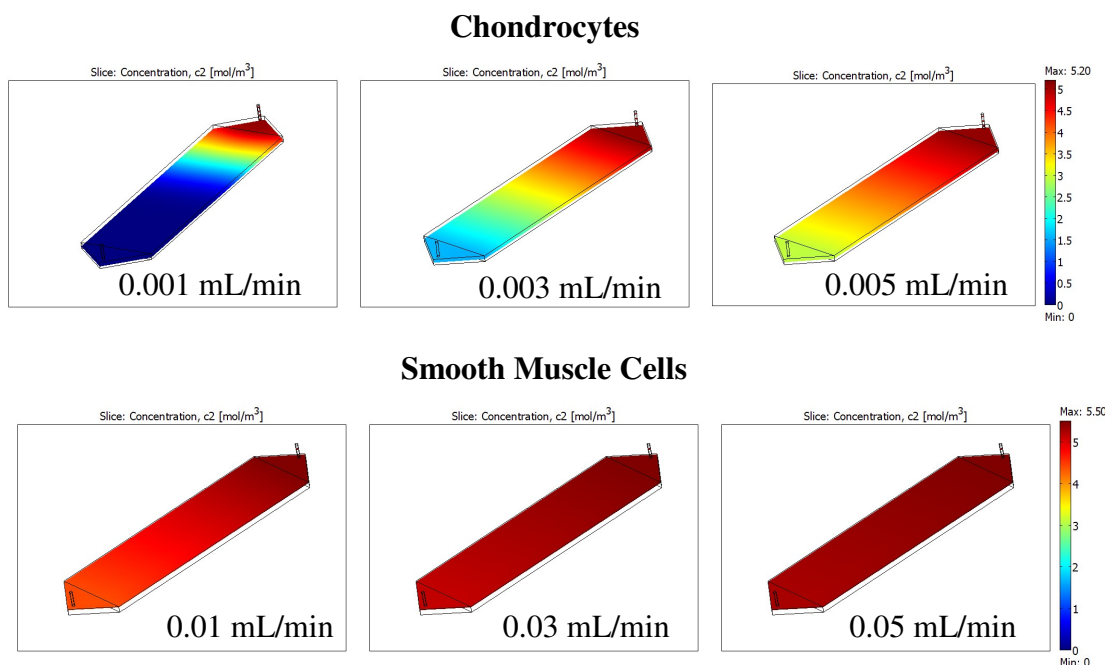


Figure 37. Simulated glucose profiles for the rectangular reactor

6.3.2. *Effect of reaction on pressure drop and shear stress.*

The pressure drop and shear stress within the reactor were measured using an 85 μm pore diameter and 120 pores/ mm^2 ($\kappa = 154 \mu\text{m}^2$) at a variety of flowrates (**Table 6**). These results show that both the pressure drop and max shear stress vary linearly with the flowrate. Additionally, for each flowrate the pressure drop and shear stress are identical for both cell types. The identical pressure drop and shear stress numbers show that they are controlled by the Brinkman equation and not affected by the convective diffusion model that contain the reaction rate law. Additionally, the values for shear stress and pressure drop did not change when the simulation was run without the reaction (rate = 0).

Table 6. Pressure drop and shear stress within the reaction simulations at a variety of different flowrates.

Flowrate (mL/min)	Chondrocyte		SMC	
	Pressure Drop (Pa)	Maximum Shear Stress (Pa)	Pressure Drop (Pa)	Maximum Shear Stress (Pa)
0.001	0.126	4.77×10^{-6}	0.126	4.77×10^{-6}
0.002	0.253	9.54×10^{-6}		
0.003	0.378	1.43×10^{-5}		
0.0035	0.441	1.67×10^{-5}		
0.004	0.504	1.91×10^{-5}		
0.005	0.631	2.39×10^{-5}		
0.01	1.26	4.77×10^{-5}	1.26	4.77×10^{-5}
0.02			2.52	9.54×10^{-5}
0.03			3.79	1.43×10^{-4}
0.04			5.04	1.91×10^{-4}
0.05			6.31	2.39×10^{-4}
1	126	4.77×10^{-3}	126	4.77×10^{-3}
5	631	0.0237	631	0.0237

6.3.3. Effect of changing pore size on reaction

Next the effect of changing pore size within the reacting system was analyzed, similar to Chapter 5. The effect of changing pore size in the cellular system was simulated using smooth muscle cells and a 0.05 mL/min flowrate. Once again nonlinear behavior is seen in both the pressure drop and shear stress (**Table 7**). Additionally, the reaction is not affected by changing the pore size.

Table 7. Effect on pressure drop and shear stress in reacting systems as pore size is decreased.

Pore Size (μm)	Pores/ mm^2	k (μm^2)	Pressure Drop (Pa)	Maximum Shear Stress (Pa)	Minimum Oxygen Concentration (mol/m^3)
85	120	154	6.31	2.39×10^{-4}	0.125
50	120	18.4	52.6	2.46×10^{-4}	0.125
37.5	120	5.82	166	2.47×10^{-4}	0.125
25	120	1.15	842	2.48×10^{-4}	0.125
17.5	120	0.276	3510	2.48×10^{-4}	0.125
10	120	0.0295	32800	2.48×10^{-4}	0.125

6.3.4. Effect of changing the number of cells

The number of cells was changed in the experiment using a cell multiplier. By including the multiplier in the rate law calculation it is possible to simulate the effect of doubling or quadrupling the number of cells present in the matrix. Therefore the effect of doubling or quadrupling the number of cells present in the matrix. Therefore the effect of increasing the cells within the reactor was explored using smooth muscle cells and a 0.05 mL/min flowrate. As shown in **Table 8** and **Figure 38**, the oxygen concentration at the exit of the porous structure decreased with the increase in the number of cells, and the pressure drop and shear stress were not affected. Additionally, the oxygen concentration was affected only by the changing the number of cells. As expected this shows that the oxygen concentration is controlled by the convective diffusion model, while shear stress and pressure drop are controlled by the Brinkman equation.

Table 8. Outlet oxygen concentration decreases as the number of cells increases.

Cell Multiplier	Pore Size (μm)	Pores/ mm^2	k (μm^2)	Pressure Drop (Pa)	Maximum Shear Stress (Pa)	Minimum Oxygen Concentration (mol/m^3)
1x	85	120	154	6.31	2.39×10^{-4}	0.125
2x	85	120	154	6.31	2.39×10^{-4}	0.071
4x	85	120	154	6.31	2.39×10^{-4}	0.018
1x	25	120	1.15	842	2.48×10^{-4}	0.125
2x	25	120	1.15	842	2.48×10^{-4}	0.071
4x	25	120	1.15	842	2.48×10^{-4}	0.018

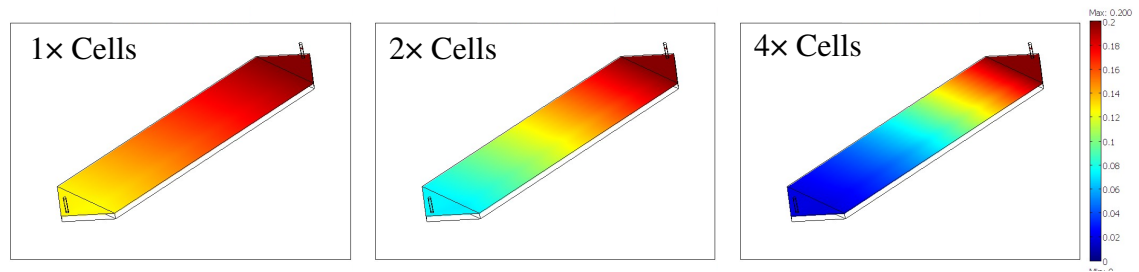


Figure 38. Effect of increasing the number of cells present in the simulation.

6.3.5. Experimental visualization of the oxygen profile

The optical profiler system offers a new method for viewing the flow profile across the porous matrix (**Figure 39**). Experiments were carried out at both 0.05 ml/min and 0.005 mL/min flowrates. First the experiment was run with unseeded chitosan scaffolds in order to get a base reading for the experimental setup. Next a cell seeded matrix was used as a packing material. All three results clearly show the physical features of the porous matrix including areas which are more densely packed and air bubbles contained within the material (**Figure 39**). However, further research is needed in order to increase the sensitivity of the system. Possibly reasons for lower sensitivity could be the sensitivity and resolution of the digital camera, non-uniform distribution of lighting (causing bright spots), long wavelengths of light leaking past the blue filter, or a final filter with too low a wavelength cutoff. Low cell concentration is another possible reason the optical profiler. Therefore, future experiments should use a higher cell count and double check the viability cells after use in the reactor. More research is needed to modify the existing setup in order to increase the amount of useful data obtained from the optical profiler, possibly including exchanging the digital camera for a spectrophotometer, replacing existing light source with a bank of blue LEDs, or using microelectrodes to measure the oxygen distribution at the inlet and outlet of the reactor.

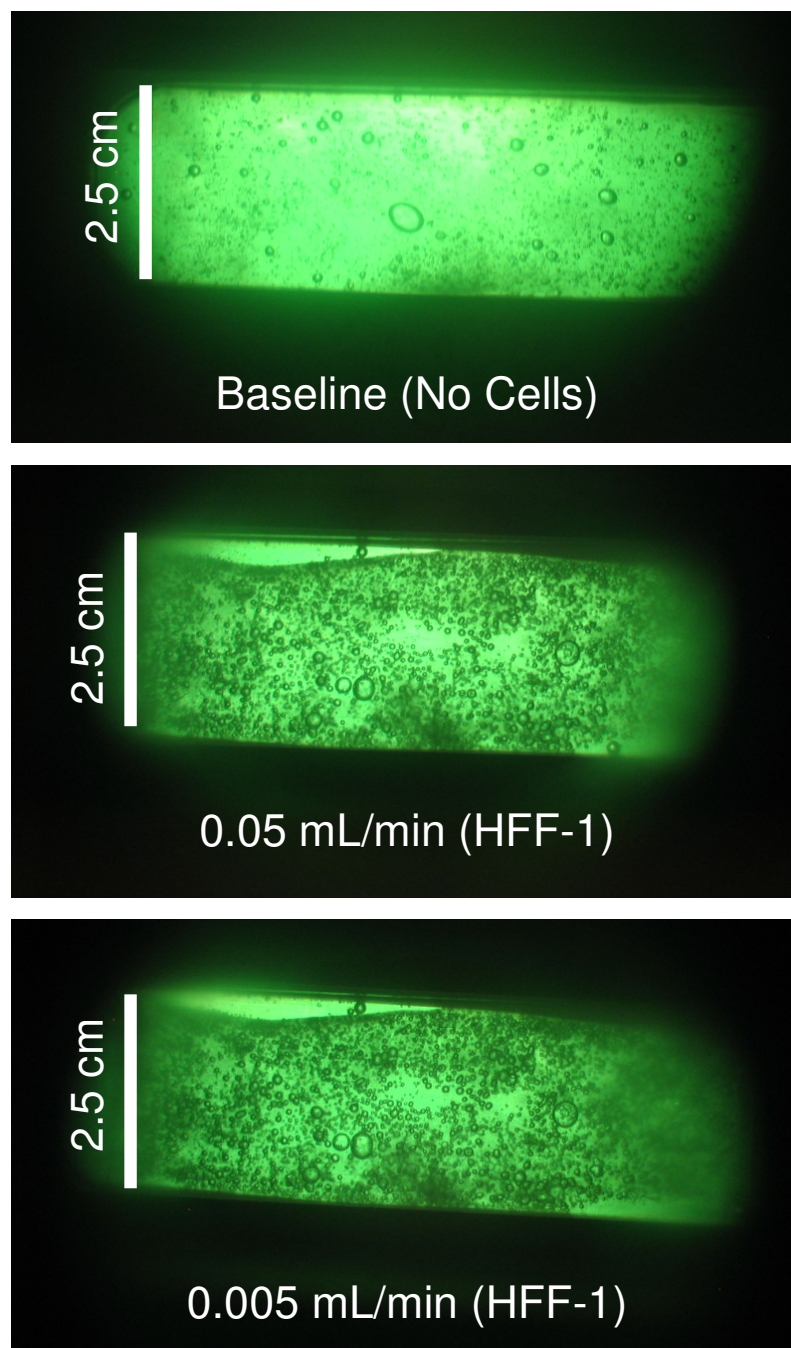


Figure 39. Fluorescent images from bioreactor in the optical system.

6.4. Discussion

One of the key goals to this work is to determine a minimum flowrate required to ensure proper nutrient flow to cells within parallel plate direct perfusion reactors. As such, two very different cell types (chondrocytes and smooth muscle cells) were analyzed via simulation. Chondrocytes are the cells primarily responsible for producing cartilage, an avascular tissue whose function is to provide cushioning and lubrication at joints. Smooth muscle cells expand and contract to ensure involuntary movement within the body. Because of their functions within the body chondrocytes are far from the blood supply while smooth muscle cells are near the blood stream. As expected the simulation data confirms that chondrocytes consumed oxygen and glucose slower than smooth muscle cells, and that the minimum flowrate required for smooth muscle cells is an order of magnitude higher than for chondrocytes.

Another issue of interest is whether the reaction and flow properties are coupled together. In real tissues when cells multiply the new cells both demand nutrients and take up space. Therefore cell growth will change the demand for oxygen and nutrients as well as the pore size and void fraction of the porous structure. However, the simulation is controlled by the permeability, void fraction, and the rate law for the consumption of oxygen. This work has shown that the permeability of the matrix controls both the pressure drop and shear stress, and the reaction rate controls the oxygen and glucose distribution across the reactor.

One of the limitations to the current model is that change in permeability, void fraction, and rate of oxygen consumption are treated as completely independent phenomena. However, these are interdependent factors which dynamically change

during tissue regeneration. Therefore, future work should focus on providing a better understanding of the microscale phenomena that occur during tissue regeneration in order to better couple the changes in reaction rate to changes in the porous structure as cells colonize the scaffold material.

Because different finite element mesh sizes were used for Chapter 5 and Chapter 6, the Chapter 6 simulation data was similar but not identical to the Chapter 5 data. For example structures 85 μm pore diameter, 120 pores/ mm^2 , and a 5mL/min flowrate the simulations developed for Chapter 5 give a pressure drop of 0.57 kPa while simulations developed for Chapter 6 give a pressure drop as 0.63 kPa. This difference is a result of computational error and shows the importance of the meshing technique and mesh size in finite element analysis. The importance of the meshing technique can also be seen in a cross sectional analysis of the results. **Figure 40** shows both the surface mesh and velocity field in the porous subdomain for both Chapter 5 and Chapter 6. Simulations including the chemical reaction would not solve using the Chapter 5. So a coarser mesh was used in Chapter 6 in order to reduce the computational load of the simulations. As expected the finer mesh used in Chapter 5 provides a more uniform velocity field then the course mesh from Chapter 6. Therefore, the effects of mesh size on the flow and reaction properties of the simulation should be monitored in future work.

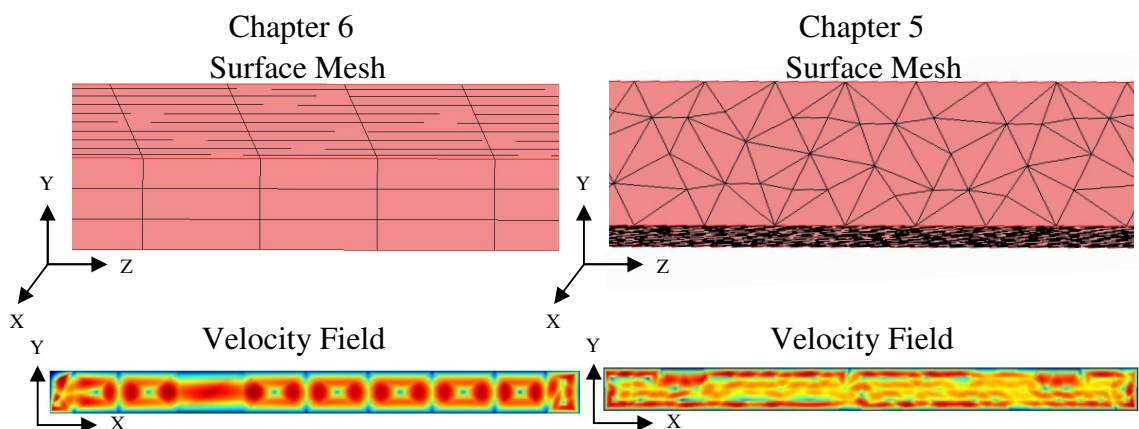


Figure 40. Surface Meshes and Velocity fields for Chapter 5 and Chapter 6, 85 μm pores, 120 pores/ mm^2 , 5 mL/min

Additionally, the simulation results were used as a basis to perform experiments and use the optical profiler system. Using flowrates between 0.01 and 0.001 mL/min the scaffold should generate a twofold difference in dissolved oxygen concentration across the reactor. However, the profiler was not able to detect that difference. This could be Future work, including the use of spectrophotometry or improvements to the existing optics, is required before the profiler will be a valid method for viewing the oxygen profile through a bioreactor system.

6.5 Acknowledgements

The author would like to thank Mamatha Devarapalli for providing data for the reacting simulations.

Chapter 7

Summary and Future Work

7.1. Summary

Tissue engineering is a field that seeks to provide materials to help alleviate the transplant crisis by regenerating damaged or diseased tissue using biodegradable materials. In brief, the damaged tissue is removed and replaced by a porous tissue scaffold. Over the course of regeneration, cells grow into the scaffolding and the material degrades away, eventually leaving only normal healthy tissue. Current clinical practice for tissue engineering uses natural matrices, such as small intestinal submucosa (SIS) which has seen partial success. However, the heterogeneous nature of natural materials leads to inconsistent tissue regeneration. Therefore polymer matrices are used in order to create scaffolds with consistent properties. Currently, there is no single material that will satisfy both the structural and biological requirements for tissue engineering. There are several methods for designing new scaffolding materials. Materials for tissue regeneration can be improved by either focusing on the synthesis of novel biomaterial or by blending existing biomaterials with required composition. My strategies focus on blending biomaterials to develop materials structures mimicking natural materials clinically utilized in few selected regeneration applications. The goal of this reverse engineering principle is to address fundamental design principles necessary for tissue regeneration strategies.

As such a multilayer composite material has successfully been developed combining both natural and synthetic polymer systems. The composite is fabricated in a mechanically interlocked 3 layer sandwich configuration. The two outer layers are made from porous chitosan and provide biological activity, and the inner layer is PLGA, providing mechanical strength²⁵⁷. The mechanical and degradation are similar to SIS, and the composite material supports the colonization and proliferation of cells¹⁶. Additionally, the mechanical properties can be tailored by modifying the molecular weight of the PLGA independent of the biological properties of the chitosan layer. The next step in the research is improving the material. The improvements made focus on studying mass transfer properties at both the local and global scale in order to better model the biological properties of SIS and to help improve in vitro regeneration when the cell seeded material is matured in a bioreactor system.

Specific Aim 1.

A nanoparticle system was developed in order to better control the local mass transport properties in the porous matrix. A variety of nanoparticles (PLGA, PLGA-HA, polystyrene latex, and chitosan) were successfully integrated into both the composite matrix and SIS. The particles were visible on both sides of the SIS, showing that the particles were embedded in the material. Additionally, the mass transport properties of SIS were successfully modified using the nanoparticles. The permeability of SIS to urea was reduced by the presence of nanoparticles, and the permeability is a function of both the size and number of nanoparticles present.

Specific Aim 2:

Engineered tissue can be matured in *in vitro* bioreactors before implantation. Non-ideal flow problems, such as poor nutrient distribution and variable mechanical forces, become more pronounced in large scale, high aspect ratio materials that are required for bladder, blood vessel, or articular cartilage applications. Therefore, the effects of flow distribution through the porous matrix were also investigated. First, the flow dynamics, characterized by residence time distribution (RTD), in a parallel plate reactor with no porous structure present were successfully simulated in the computational fluid dynamics (CFD) software CFX. The RTD was then successfully validated using a bench top reactor and a colored dye tracer, and b calculating an analytical solution. Additionally, RTD experiments utilizing the porous chitosan material provided insight into the effect of the porous structure on the flow distribution within the material. Next, the effect of changes in the porous structure, as a result of both scaffold fabrication and cellular ingrowth, on flow distribution, pressure drop, and shear stress within the matrix were successfully simulated using COMSOL Multiphysics. The simulations including the porous matrix were then validated using a benchtop reactor.

Specific Aim 3.

The effect of cellular metabolism was included into the simulation. Both the concentration of oxygen and glucose were integrated into the simulation using a Michaelis-Menten rate law. Simulations were performed using data from both chondrocytes and smooth muscle cells, showing that a flowrate between 0.01 mL/s and 0.001mL/s gives a profile across the reactor with a twofold difference in oxygen concentration. Further, an optics system was created in order to attempt to visualize the

oxygen profile across the reactor. However, further research is required to make the optical profiler a viable method for measuring the oxygen concentration across a reactor system.

7.2. Future Work

While these developments have helped to improve polymer tissue engineering materials there is still room for improvement. One goal is to enable the intelligent design of scaffold materials tailored to each specific clinical need. A better understanding for the fundamental processes during tissue regeneration is needed in addition to improvements to the tailorability of existing materials.

7.2.1. Nanoparticle delivery of heterogeneous cellular signals.

As mentioned previously, most biomaterials research focuses on one aspect of tissue regeneration to the exclusion of others. During my graduate work I focused on improving the structural properties of tissue engineering materials. However the biological properties of the scaffolding must also be improved. Cells receive biological signals from a variety of molecules. Some, like growth factors, have very short (minutes to hours) half-lives in solution. Therefore in order to better utilize these signals they must be protected from denaturation and released in a controlled manner. One release method uses micro and nano-particles for controlled release of bioactive molecules. The field of drug delivery tends to focus on the homogeneous sustained release of the molecule of interest. However, human tissue is a heterogeneous material, containing different cell types and materials. Therefore heterogeneous signaling is required for optimal regeneration using tissue engineering materials. Additionally, nanometer size particles

are uptaken by the cells, enabling both the intracellular and extracellular delivery of active biomolecules within the tissue construct. The nano sized particles are also important because most cells have a diameter of roughly 10 μm . Therefore the nano size is required in order to send heterogeneous signals to a single cell. Another advantage of using particles is that they can be created from a large group of materials, be fabricated over multiple size ranges, and be distributed in a variety of manners. Therefore it is should be possible to achieve both homogeneous and heterogeneous release behaviors. By modifying the size, location, and concentration of particles within the material it should be possible to form sustained concentration gradients within the material, and by using multiple sets of particles loaded with different bioagents it is possible to regenerate complex tissue structures containing multiple cell types. Additionally, the presence of nanoparticles can be used to further tailor the transport properties within the scaffold material.

7.2.2. Complex scaffold architecture mimicking anatomical structures.

One inherent weakness in the current fabrication techniques for porous tissue scaffolds is their simple structures, typically either planar sheets or small cylinders. However, tissues in the body come in a variety of geometries. For example the bladder is a hollow spherical structure, blood vessels are cylindrical. Additionally, both bladder and blood vessels have a multilayer asymmetric architecture. While some fabrication schemes like those that rely on photolithography are planar in nature, several other techniques such as wet spinning, electrospinning, controlled rate freezing and lyophilization, and rapid prototyping could be adapted to form hollow 3D scaffold

material suitable for clinical use. Additionally, the composite system could be used to create a layered asymmetric structure similar to native tissue.

7.2.3. Mechanotransduction in bioreactor engineering.

The effect of stress on tissue regeneration is another area that has not been fully explored in the context of tissue engineering. Both physical stresses and fluid shear stress affect the colonization, alignment, and extracellular matrix production of a variety of cells grown on 3D tissue scaffolds, from endothelial cells and smooth muscle cells (blood vessels) to chondrocytes (cartilage). Therefore, the forces in and around the scaffold material affect the quality of regenerated tissue. There are several methods available to directly place stresses on scaffold materials. Two methods are currently used to generate stresses with the scaffold material. Hydraulic shear stress can be controlled using fluid flow within the reactor, or mechanical stresses can be added by deforming the stretching or compressing the material. Therefore a comparison study of these two mechanisms for mechanotransduction should lead to improved quality of regenerated tissue, as well as helping elucidate the fundamental effects of mechanical stimulus upon regenerating tissue.

7.2.4. Improving reactor simulations and the optical profiler system.

Both the reactor simulations and the optical profiler show promise in providing a better understanding of nutrient transport within the system. One way to improve the data generated by simulations is to provide better models for the porous structure. Currently, the simulation uses the Brinkman equations (which assume a symmetric spherical pore system) to model transport through the porous structure. In reality the porous matrix is

not symmetric and the pores are not spherical. Therefore, it would be beneficial to measure the actual porous structure by micro-computer tomography (μ -CT) and then use that data to build the mesh in the porous region. With μ -CT it is also possible to measure cell seeded matrices and determine how the porous structure and the porosity change as cells colonize the material. Additionally, by altering the μ -CT settings it is possible to differentiate between matrix and cells, giving a 3D representation for the cell density on all areas of the scaffold. The main drawbacks to μ -CT imaging are that it has only a 10 μ m resolution and it is difficult to get high quality pictures of soft materials, other options for determining how cell colonization changes the porous structure include both histology and environmental SEM. Another important step in simulation work is experimental validation. Therefore, future work should also attempt to validate the simulations using electrochemical dissolved oxygen probes. The cellular tolerance for hypoxia within the parallel plate reactor is not well understood, and with validation equipment in place a more accurate lower bound on the flowrate may be determined.

A possible reason for the optical profiler not to show a measurable signal could be attributed to low a number of cells used in the experiments. Hence, experiments have to be performed with increased cell number, similar to the numbers used in simulation. In addition, the experiments should use a cell type similar to the simulation (e.g. SMCs). Experiments using a higher cell number may provide a measurable signal. Future experiments should also check the viability of cell seeded matrices after they are used in the optical profiler.

Appendix 1

A.1: Mathematical Derivations.

The RTD function for an ideal completed developed laminar flow with no slip at the boundaries can be derived by the method described in Fogler³⁴⁰. The reactor was modeled as a set of parallel plates with a width (w) and a height (h) as described in Truskey et al³⁴⁴. For the ideal case, side and end effects are ignored leaving a laminar flow profile only in the y-direction. Therefore, the velocity in the z-direction can be calculated from the volumetric flowrate.

$$V_z = V_{\max} \left(1 - \frac{4y^2}{h^2} \right) \quad (\text{A.1})$$

$$v_0 = \frac{2}{3} V_{\max} wh \quad (\text{A.2})$$

$$V_z = \frac{3v_0}{2wh} \left(1 - 4 \frac{y^2}{h^2} \right) \quad (\text{A.3})$$

Next the required for a fluid particle to travel in the z direction is calculated.

$$t(z) = \frac{L}{V_z} = \frac{L2wh}{3v_0} \left(\frac{1}{1 - \frac{4y^2}{h^2}} \right) \quad (\text{A.4})$$

$$\tau = \frac{\text{Volume}}{v_0} = \frac{Lwh}{v_0} \quad (\text{A.5})$$

$$t(z) = \frac{2\tau}{3\left(1 - \frac{4y^2}{h^2}\right)} \quad (\text{A.6})$$

Next the volume fraction of total fluid passing between y and $y + dy$, $\frac{dv}{v_0}$, and the fraction spending between time between t and dt in the reactor were calculated.

$$\frac{dv}{v_0} = \frac{\Delta v}{v_0} = \frac{V_z w y}{v_0} \quad (\text{A.7})$$

$$E(t)dt = \frac{dv}{v_0} \quad (\text{A.8})$$

$$E(t)dt = \frac{V_z}{v_0} w dy \quad (\text{A.9})$$

Eq. (A.8) was differentiated in order to replace the dt term.

$$dt(z) = \frac{16\tau}{3} \left(\frac{\frac{y}{h^2}}{\left(1 - \frac{4y^2}{h^2}\right)^2} \right) dy \quad (\text{A.10})$$

The dt value was then substituted into Eq. (A.9).

$$E(t) \frac{16\tau}{3} \left(\frac{\frac{y}{h^2}}{\left(1 - \frac{4y^2}{h^2}\right)^2} \right) = \frac{Lw}{t(z)v_0} \quad (\text{A.11})$$

The equation is further simplified by substituting in t^2 .

$$E(t) = \frac{\tau^2 h}{12t^3 y} \quad (\text{A.12})$$

Further, from Eq. (A.8).

$$\frac{y}{h} = \frac{1}{2} \sqrt{1 - \frac{2\tau}{3t}} \quad (\text{A.13})$$

The final RTD expression is

$$E(t) = \frac{\tau^2}{6t^3} \left(1 - \frac{2\tau}{3t} \right)^{-1/2} \quad (\text{A.14})$$

Finally the minimum residence time is calculated from the maximum velocity.

$$t_{\min} = \frac{L}{V_{\max}} = \frac{L}{\frac{3}{2} V_{\text{avg}}} = \frac{2Lwh}{3V_{\text{avg}}wh} = \frac{2\tau}{3} \quad (\text{A.15})$$

$$E(t) = 0, t < \frac{2\tau}{3} \quad (\text{A.16})$$

$$E(t) = \frac{\tau^2}{6t^3} \left(1 - \frac{2\tau}{3t} \right)^{-1/2}, t \geq \frac{2\tau}{3} \quad (\text{A.17})$$

Eq. (A.16) and Eq.(A.17) were used to generate E(t) curves for the ideal conditions.

Appendix 2

A.2. CFX Walkthrough

This is a walkthrough for creating a simulation of liquid flowing through a tubular reactor where a tracer is added as a step change at time zero and the simulation is run until the reactor contains 100% tracer

Building and running a CFX model

Open CFX

Create a working directory

- working directory should not be located on desktop or contain spaces.

Start CAD2Mesh (ANSYS workbench)

CAD2Mesh

Click on New – Geometry

Select desired length – Inch

Select x-y plane

Select sketching tab

Select draw – circle

Draw the circle with a center point at the origin

Select Dimensions Tab – Diameter

Click on circle – specify diameter

Click on the dimensions box – Enter 6in diameter

Click Extrude button – set depth = 144in

Click Generate

Awe in wonder at the tube you've drawn!!! Then save it, and close DesignerModeler!

From Project screen choose DesignerModeler Tasks – New CFX Mesh

Go to Model – Geometry – Verify Options – Short Edge Length

- This is where you set the minimum edge length for the tetrahedral volume elements

Go to Mesh – Spacing – Default Body Spacing – Maximum Spacing

- This is where you set the maximum edge length for body spacing

Go to Mesh – Spacing – Default face Spacing – Minimum Edge Length

- This is where you set the minimum edge length for face spacing

Go to Mesh – Spacing – Default face Spacing – Maximum Edge Length

- This is where you set the maximum edge length for face spacing
- I like to make this number less than the radius

Next go to the upper toolbar click on Go – Verify Geometry

Click on Go – Generate All Surface Meshes

Click on Go – Generate Volume Mesh

I like to adjust the edge lengths and spacing until I get 30,000 – 50,000 volume elements

Save your work, close ANSYS workbench, Start CFX-Pre

CFX-Pre

Making the Tracer

Click the “Materials” tab

Scroll down and select Water.

Click the “Duplicate Selected Objects” button (looks like two sheets of paper connected by an arrow)

Enter Name for duplicate (I used “Tracer”)

Import the Mesh

Click the mesh tab

Click the “Import Mesh” button (has a folder with a blue mesh behind it)

Browse for a new file (click the button that looks like a folder next to the file entry box)

Open Unnamed.gtm

Click OK

Setting up the simulation

Next you’re going to walk down the buttons at the top of the screen.

Starting with “Define Simulation Type” (looks like a clock) and ending with “Write Definition File.” First run the simulation in Steady State, then modify it to run in transient conditions.

Define Simulation Type

Select Steady State – Click OK

Create a Domain

Name your domain and click OK

General Options – Fluids List - Choose Water and Tracer

Leave the rest as defaults

Fluid Models – check “Homogeneous Model” for both Multiphase and Heat transfer Model

Tracer, Water, and Fluid Pairs – use default values

Boundary Conditions

Create Boundary – Boundary Type - Inlet

Basic Settings – Location – select the inlet location (click on the arrow and it will let you see where the selected boundary is)

Boundary Details –

Flow Regime – Subsonic

Mass and Momentum – Option Bulk mass flow rate (set the mass flow in)

Flow direction – normal to boundary

Turbulence – depends on info available (I usually use “default intensity and autocompute length scale”)

Fluid Values – Boundary Conditions

Tracer volume fraction = 0

Water Volume Fraction = 1

Create Boundary – Boundary Type – Outlet

Basic Settings – Location – select the inlet location (click on the arrow and it will let you see where the selected boundary is)

Boundary Details –

Flow Regime – Subsonic

Mass and Momentum – Option Bulk mass flow rate (set the mass flow out)

Create Boundary – Boundary Type – Wall

Basic Settings – Location – select the inlet location (click on the arrow and it will let you see where the selected boundary is)

Boundary Details – No Slip, Smooth wall

Global Initialization

Global Settings – Check “Turbulent Eddy Dissipation”

Leave the rest set to defaults

Fluid Settings –

Tracer Volume Fraction = 0

Water Volume Fraction = 1

Solver Control

Use Defaults

Results

Use either Full or Selected variables (Velocity and tracer volume fraction)

Write Solver File

Add file name and start solver manager

Solver Manager

Load your definition file and run solver

Modifying the Simulation for Transient Flow

First you may want to save your file as a new file, that way you still have the steady state file you just ran. Then modify the following:

Simulation Type – Basic settings – Option – Transient

Next set the time duration and timesteps... I like to set the number of timesteps per run and the timestep length

Example: For the 30mL/s flowrate I used 80 timesteps with 30 second timestep durations (giving a total run time of 40 minutes), or I set the time per run and timestep duration (40 minutes at a 30 second timestep durations is 80 timesteps)

Physics – Inlet – Change your entering volume fractions to all tracer and no water

Physics – Global Initialization – Fluid Setting - Change the volume fractions automatic

Output Control – Transient Results – Create Transient Results File

The transient results file is what saves your data at each timestep, if you don't make one then only your last timestep data will be recorded.

Write a Solver File

Name the transient definition file something different than the steady state file

Solver Manager

Definition file: The Transient definition file

Initial Values File: The Steady State results file

Check Interpolate Initial values onto def file mesh (if you get a mesh doesn't match error check this box)

Start Run!

CFX-Post

Load Results

Create plane in center of tube (YZ plane at $X = 0$)

Create contour plot

Location: The plane in the center of the tube

Variable: Tracer.VolumeFraction

Range: Global

Now play with the timestep selector (Top menu, looks like a clock) and watch the colors move!

Create plane just before the outlet (XY plane at $Z = 143.9$ in)

Using the actual outlet tends to be problematic

Optional but pretty - Create contour plot

Location: The plane near the outlet

Variable: Tracer.VolumeFraction

Range: Global

To export data

File – Export

Filename – pick a filename (the file will be written to your working directory unless you browse to a different folder)

Type: Generic

Locators: Plane near the outlet

Select Variables: Tracer Velocity, Tracer Volume Fraction

Save

Open the .csv file in MS Excel

Taking Pictures

File - Print

Format – JPEG

Filename – this is where it will save the file

If you want to print it on paper, then check “use white background”

References

1. United Network for organ sharing. New Stats Illustrate Donor Shortage. Retrieved on April 5, 2008, <http://www.unos.org/>.
2. Kropp, B. P.; Cheng, E. Y.; Lin, H.-K.; Zhang, Y., Reliable and reproducible bladder regeneration using unseeded distal small intestinal submucosa. *Journal of Urology* **2004**, 172, ((4 Pt 2)), 1710-3.
3. Raghavan, D.; Kropp, B. P.; Lin, H. K.; Zhang, Y.; Cowan, R.; Madihally, S. V., Physical characteristics of small intestinal submucosa scaffolds are location-dependent. *J Biomed Mater Res A* **2005**, 73A, (1), 90-6.
4. Risbud, M. V.; Hardikar, A. A.; Bhat, S. V.; Bhonde, R. R., pH-sensitive freeze-dried chitosan-polyvinyl pyrrolidone hydrogels as controlled release system for antibiotic delivery. *J Control Release* **2000**, 68, (1), 23-30.
5. Huang, Y.; Onyeri, S.; Siewe, M.; Moshfeghian, A.; Madihally, S. V., In vitro characterization of chitosan-gelatin scaffolds for tissue engineering. *Biomaterials* **2005**, 26, (36), 7616-27.
6. Lavik, E.; Teng, Y. D.; Snyder, E.; Langer, R., Seeding neural stem cells on scaffolds of PGA, PLA, and their copolymers. *Methods Mol Biol* **2002**, 198, 89-97.
7. Nakamura, T.; Hitomi, S.; Watanabe, S.; Shimizu, Y.; Jamshidi, K.; Hyon, S. H.; Ikada, Y., Bioabsorption of polylactides with different molecular properties. *J Biomed Mater Res* **1989**, 23, (10), 1115-30.
8. Mooney, D. J.; Mazzoni, C. L.; Breuer, C.; McNamara, K.; Hern, D.; Vacanti, J. P.; Langer, R., Stabilized polyglycolic acid fibre-based tubes for tissue engineering. *Biomaterials* **1996**, 17, (2), 115-24.
9. Gao, J.; Niklason, L.; Langer, R., Surface hydrolysis of poly(glycolic acid) meshes increases the seeding density of vascular smooth muscle cells. *J Biomed Mater Res* **1998**, 42, (3), 417-24.
10. Marra, K. G.; Szem, J. W.; Kumta, P. N.; DiMilla, P. A.; Weiss, L. E., In vitro analysis of biodegradable polymer blend/hydroxyapatite composites for bone tissue engineering. *J Biomed Mater Res* **1999**, 47, (3), 324-35.
11. Engelberg, I.; Kohn, J., Physico-mechanical properties of degradable polymers used in medical applications: a comparative study. *Biomaterials* **1991**, 12, (3), 292-304.
12. Ozawa, T.; Mickle, D. A.; Weisel, R. D.; Koyama, N.; Wong, H.; Ozawa, S.; Li, R. K., Histologic changes of nonbiodegradable and biodegradable biomaterials used to repair right ventricular heart defects in rats. *J Thorac Cardiovasc Surg* **2002**, 124, (6), 1157-64.
13. Kulkarni, R. K.; Moore, E. G.; Hegyeli, A. F.; Leonard, F., Biodegradable poly(lactic acid) polymers. *J Biomed Mater Res* **1971**, 5, (3), 169-81.
14. Huang, Y.; Siewe, M.; Madihally, S. V., Effect of spatial architecture on cellular colonization. *Biotechnol Bioeng* **2006**, 93, (1), 64-75.

15. Lawrence, B. J.; Madihally, S. V., Cell colonization in degradable 3D porous matrices. *Cell Adhesion and Migration* **2008**, 2, (1), 9-16.
16. Lawrence, B.; Maase, E.; Lin, H.-K.; Madihally, S., Multilayer Composite Scaffolds with Properties Similar to Small Intestinal Submucosa. *Journal of Biomedical Materials Research, Part A* **2007**, [in press].
17. Korossis, S. A.; Bolland, F.; Kearney, J. N.; Fisher, J.; Ingham, E., Bioreactors in Tissue Engineering. In *Topics in Tissue Engineering, Volume 2*, Ashammakhi, N.; Reis, R. L., Eds. EXPERTISSUES: Helsinki, Finland., 2005.
18. Langer, R.; Vacanti, J. P., Tissue engineering. *Science* **1993**, 260, (5110), 920-6.
19. Persidis, A., Tissue engineering. *Nat Biotechnol* **1999**, 17, 508-510.
20. Vyavahare, N.; Ogle, M.; Schoen, F. J.; Zand, R.; Gloeckner, D. C.; Sacks, M.; Levy, R. J., Mechanisms of bioprosthetic heart valve failure: fatigue causes collagen denaturation and glycosaminoglycan loss. *J Biomed Mater Res* **1999**, 46, (1), 44-50.
21. Chvapil, M., Collagen sponge: theory and practice of medical applications. *Journal of Biomedical Materials Research* **1977**, 11, (5), 721-741.
22. Gunatillake, P. A.; Adhikari, R., Biodegradable synthetic polymers for tissue engineering. *Eur Cell Mater* **2003**, 5, 1-16; discussion 16.
23. Oberpenning, F.; Meng, J.; Yoo, J. J.; Atala, A., De novo reconstitution of a functional mammalian urinary bladder by tissue engineering. *Nat Biotechnol* **1999**, 17, (2), 149-55.
24. Medalie, D. A.; Eming, S. A.; Tompkins, R. G.; Yarmush, M. L.; Krueger, G. G.; Morgan, J. R., Evaluation of human skin reconstituted from composite grafts of cultured keratinocytes and human acellular dermis transplanted to athymic mice. *J Invest Dermatol* **1996**, 107, (1), 121-7.
25. Feng, X.; Tan, J.; Pan, Y.; Wu, Q.; Ruana, S.; Shena, R.; Chena, X.; Dua, Y., Control of hypertrophic scar from inception by using xenogenic (porcine) acellular dermal matrix (ADM) to cover deep second degree burn. *Burns* **2006**, 32, (3), 293-298.
26. Hoenicka, M.; Lehle, K.; Jacobs, V. R.; Schmid, F. X.; Birnbaum, D. E., Properties of the Human Umbilical Vein as a Living Scaffold for a Tissue-Engineered Vessel Graft. *Tissue Engineering* **2007**, 13, (1), 219-229.
27. Daniel, J.; Abe, K.; McFetridge, P. S., Development of the Human Umbilical Vein Scaffold for Cardiovascular Tissue Engineering Applications. *SO - ASAIO Journal May/June 2005*;51(3):252-261.
28. Knight, R. L.; Wilcox, H. E.; Korossis, S. A.; Fisher, J.; Ingham, E., The use of acellular matrices for the tissue engineering of cardiac valves. *Proceedings of the I MECH E Part H Journal of Engineering in Medicine* **2008**, 222, 129-143.
29. Mirsadraee, S.; Wilcox, H. E.; Watterson, K. G.; Kearney, J. N.; Hunt, J.; Fisher, J.; Ingham, E., Biocompatibility of Acellular Human Pericardium. *Journal of Surgical Research* **2007**, 143, (2), 407-414.
30. Ott, H. C.; Matthiesen, T. S.; Goh, S.-K.; Black, L. D.; Kren, S. M.; Netoff, T. I.; Taylor, D. A., Perfusion-decellularized matrix: using nature's platform to engineer a bioartificial heart. *Nat Med* **2008**, 14, (2), 213-221.
31. Badylak, S. F., The extracellular matrix as a biologic scaffold material. *Biomaterials* **2007**, 28, (25), 3587-3593.
32. Kropp, B. P., Small-intestinal submucosa for bladder augmentation: a review of preclinical studies. *World J Urol* **1998**, 16, (4), 262-7.

33. Badylak, S. F.; Record, R.; Lindberg, K.; Hodde, J.; Park, K., Small intestinal submucosa: a substrate for in vitro cell growth. *J Biomater Sci Polym Ed* **1998**, 9, (8), 863-78.
34. Pariente, J. L.; Kim, B. S.; Atala, A., In vitro biocompatibility evaluation of naturally derived and synthetic biomaterials using normal human bladder smooth muscle cells. *J Urol* **2002**, 167, (4), 1867-71.
35. Hiles, M. C.; Badylak, S. F.; Lantz, G. C.; Kokini, K.; Geddes, L. A.; Morff, R. J., Mechanical properties of xenogeneic small-intestinal submucosa when used as an aortic graft in the dog. *J Biomed Mater Res* **1995**, 29, (7), 883-91.
36. Badylak, S. F.; Kropp, B.; McPherson, T.; Liang, H.; Snyder, P. W., Small intestinal submucosa: a rapidly resorbed bioscaffold for augmentation cystoplasty in a dog model. *Tissue Eng* **1998**, 4, (4), 379-87.
37. Allman, A. J.; McPherson, T. B.; Badylak, S. F.; Merrill, L. C.; Kallakury, B.; Sheehan, C.; Raeder, R. H.; Metzger, D. W., Xenogeneic extracellular matrix grafts elicit a TH2-restricted immune response. *Transplantation* **2001**, 71, (11), 1631-1640.
38. Badylak, S. F.; Lantz, G. C.; Coffey, A.; Geddes, L. A., Small intestinal submucosa as a large diameter vascular graft in the dog. *The Journal Of Surgical Research* **1989**, 47, (1), 74-80.
39. Pavcnik, D.; Uchida, B. T.; Timmermans, H. A.; Corless, C. L.; O'Hara, M.; Toyota, N.; Moneta, G. L.; Keller, F. S.; Rosch, J., Percutaneous bioprosthetic venous valve: a long-term study in sheep. *J Vasc Surg* **2002**, 35, (3), 598-602.
40. Bruntzos, E.; Pavcnik, D.; Timmermans, H. A.; Corless, C.; Uchida, B. T.; Nihsen, E. S.; Nakata, M.; Schoder, M.; Kaufman, J. A.; Keller, F. S.; Rosch, J., Remodeling of suspended small intestinal submucosa venous valve: an experimental study in sheep to assess the host cells' origin. *J Vasc Interv Radiol* **2003**, 14, (3), 349-56.
41. Matheny, R. G.; Hutchison, M. L.; Dryden, P. E.; Hiles, M. D.; Shaar, C. J., Porcine small intestine submucosa as a pulmonary valve leaflet substitute. *J Heart Valve Dis* **2000**, 9, (6), 769-74; discussion 774-5.
42. Bello, Y. M.; Falabella, A. F.; Eaglstein, W. H., Tissue-engineered skin. Current status in wound healing. *Am J Clin Dermatol* **2001**, 2, (5), 305-13.
43. Badylak, S. F.; Tullius, R.; Kokini, K.; Shelbourne, K. D.; Klootwyk, T.; Voytik, S. L.; Kraine, M. R.; Simmons, C., The use of xenogeneic small intestinal submucosa as a biomaterial for Achilles tendon repair in a dog model. *Journal Of Biomedical Materials Research* **1995**, 29, (8), 977-985.
44. Prevel, C. D.; Eppley, B. L.; Summerlin, D. J.; Sidner, R.; Jackson, J. R.; McCarty, M.; Badylak, S. F., Small intestinal submucosa: utilization as a wound dressing in full-thickness rodent wounds. *Ann Plast Surg* **1995**, 35, (4), 381-8.
45. Nuininga, J. E.; Moerkerk, H.; Hanssen, A.; Hulsbergen, C. A.; Oosterwijk-Wakka, J.; Oosterwijk, E.; de Gier, R. P.; Schalken, J. A.; Kuppevelt, T. H.; Feitz, W. F., A rabbit model to tissue engineer the bladder. *Biomaterials* **2004**, 25, (9), 1657-61.
46. Cheng, E. Y.; Kropp, B. P., Urologic tissue engineering with small-intestinal submucosa: potential clinical applications. *World J Urol* **2000**, 18, (1), 26-30.
47. Colvert, J. R., 3rd; Kropp, B. P.; Cheng, E. Y.; Pope, J. C. t.; Brock, J. W., 3rd; Adams, M. C.; Austin, P.; Furness, P. D., 3rd; Koyle, M. A., The use of small intestinal submucosa as an off-the-shelf urethral sling material for pediatric urinary incontinence. *J Urol* **2002**, 168, (4 Pt 2), 1872-5; discussion 1875-6.

48. Smith, T. G., 3rd; Gettman, M.; Lindberg, G.; Napper, C.; Pearle, M. S.; Cadeddu, J. A., Ureteral replacement using porcine small intestine submucosa in a porcine model. *Urology* **2002**, 60, (5), 931-4.
49. El-Assmy, A.; El-Hamid, M. A.; Hafez, A. T., Urethral replacement: a comparison between small intestinal submucosa grafts and spontaneous regeneration. *BJU Int* **2004**, 94, (7), 1132-5.
50. Kropp, B. P.; Cheng, E. Y., Bioengineering organs using small intestinal submucosa scaffolds: in vivo tissue-engineering technology. *J Endourol* **2000**, 14, (1), 59-62.
51. Kropp, B. P., Small-intestinal submucosa for bladder augmentation: a review of preclinical studies. 262-7.
52. Kropp, B. P.; Rippy, M. K.; Badylak, S. F.; Adams, M. C.; Keating, M. A.; Rink, R. C.; Thor, K. B., Regenerative urinary bladder augmentation using small intestinal submucosa: urodynamic and histopathologic assessment in long-term canine bladder augmentations. *J Urol* **1996**, 155, (6), 2098-104.
53. Pope, J. C. t.; Davis, M. M.; Smith, E. R., Jr.; Walsh, M. J.; Ellison, P. K.; Rink, R. C.; Kropp, B. P., The ontogeny of canine small intestinal submucosa regenerated bladder. *J Urol* **1997**, 158, (3 Pt 2), 1105-10.
54. Kropp, B. P.; Cheng, E. Y.; Pope, J. C. t.; Brock, J. W., 3rd; Koyle, M. A.; Furness, P. D., 3rd; Weigel, N. D.; Keck, R. W.; Kropp, K. A., Use of small intestinal submucosa for corporal body grafting in cases of severe penile curvature. *J Urol* **2002**, 168, (4 Pt 2), 1742-5; discussion 1745.
55. Zhang, Y.; Kropp, B. P.; Lin, H. K.; Cowan, R.; Cheng, E. Y., Bladder regeneration with cell-seeded small intestinal submucosa. *Tissue Eng* **2004**, 10, (1-2), 181-7.
56. Kropp, B. P.; Eppley, B. L.; Prevel, C. D.; Rippy, M. K.; Harruff, R. C.; Badylak, S. F.; Adams, M. C.; Rink, R. C.; Keating, M. A., Experimental assessment of small intestinal submucosa as a bladder wall substitute. *Urology* **1995**, 46, (3), 396-400.
57. Kropp, B. P.; Rippy, M. K.; Badylak, S. F.; Adams, M. C.; Keating, M. A.; Rink, R. C.; Thor, K. B., Regenerative urinary bladder augmentation using small intestinal submucosa: urodynamic and histopathologic assessment in long-term canine bladder augmentations. *J Urol* **1996**, 155, (6), 2098-104.
58. Lee, S. H.; Kim, B. S.; Kim, S. H.; Kang, S. W.; Kim, Y. H., Thermally produced biodegradable scaffolds for cartilage tissue engineering. *Macromol Biosci* **2004**, 4, (8), 802-10.
59. Mooney, D. J.; Baldwin, D. F.; Suh, N. P.; Vacanti, J. P.; Langer, R., Novel approach to fabricate porous sponges of poly(D,L-lactic-co-glycolic acid) without the use of organic solvents. *Biomaterials* **1996**, 17, (14), 1417-22.
60. Riddle, K. W.; Mooney, D. J., Role of poly(lactide-co-glycolide) particle size on gas-foamed scaffolds. *J Biomater Sci Polym Ed* **2004**, 15, (12), 1561-70.
61. Chun, K. W.; Cho, K. C.; Kim, S. H.; Jeong, J. H.; Park, T. G., Controlled release of plasmid DNA from biodegradable scaffolds fabricated using a thermally-induced phase-separation method. *J Biomater Sci Polym Ed* **2004**, 15, (11), 1341-53.
62. Mikos, A. G.; Thorsen, A. J.; Czerwonka, L. A.; Bao, Y.; Langer, R.; Winslow, D. N.; Vacanti, J. P., Preparation and characterization of poly(L-lactic acid) foams. *Polymer* **1994**, 35, (5), 1068-1077.

63. Hutmacher, D. W., Scaffolds in tissue engineering bone and cartilage. *Biomaterials* **2000**, 21, (24), 2529-2543.
64. Smay, J. E.; Nadkarni, S. S.; Xu, J.; Wiist, D.; Madihally, S. V., Direct Writing of Multi-Material Structures using Colloidal Inks. *Proceedings of 2006 NSF Design, Service, and Manufacturing Grantees and Research Conference, St. Louis, Missouri 2006*.
65. Wang, Y. C.; Ho, C. C., Micropatterning of proteins and mammalian cells on biomaterials. *Faseb J* **2004**, 8, 8.
66. Yang, Y. B., S.; Tomasko, D. L.; Lee, L. J.; Yang, S., Fabrication of well-defined PLGA scaffolds using novel microembossing and carbon dioxide bonding. *Biomaterials* **2005**, 26, (15), 2585-2594.
67. Yang, R. C., T.; Chen, H.; Wang, W., Microfabrication of biodegradable (PLGA) honeycomb-structures and potential applications in implantable drug delivery. *Sensors and Actuators B: Chemical* **2005**, 106, (2), 506-511.
68. Thapa, A. M., D. C.; Webster, T. J.; Haberstroh, K. M., Nano-structured polymers enhance bladder smooth muscle cell function. *Biomaterials* **2003**, 24, (17), 2915-2926.
69. Pham, Q. P.; Sharma, U.; Mikos, A. G., Electrospinning of polymeric nanofibers for tissue engineering applications: a review. *Tissue Engineering* **2006**, 12, (5), 1197-1211.
70. Li, W. J.; Laurencin, C. T.; Caterson, E. J.; Tuan, R. S.; Ko, F. K., Electrospun nanofibrous structure: a novel scaffold for tissue engineering. *J Biomed Mater Res* **2002**, 60, (4), 613-21.
71. Lee, C. H.; Shin, H. J.; Cho, I. H.; Kang, Y. M.; Kim, I. A.; Park, K. D.; Shin, J. W., Nanofiber alignment and direction of mechanical strain affect the ECM production of human ACL fibroblast. *Biomaterials* **2005**, 26, (11), 1261-70.
72. Bryant, S. J.; Chowdhury, T. T.; Lee, D. A.; Bader, D. L.; Anseth, K. S., Crosslinking density influences chondrocyte metabolism in dynamically loaded photocrosslinked poly(ethylene glycol) hydrogels. *Annals of Biomedical Engineering* **2004**, 32, (3), 407 - 417.
73. Chenite, A.; Chaput, C.; Wang, D.; Combes, C.; Buschmann, M. D.; Hoeman, C. D.; Leroux, J. C.; Atkinson, B. L.; Binette, F.; Selmani, A., Novel injectable neutral solutions of chitosan form biodegradable gels in situ. *Biomaterials* **2000**, 21, (21), 2155-2161.
74. Nuttelman, C. R.; Tripodi, M. C.; Anseth, K. S., In vitro osteogenic differentiation of human mesenchymal stem cells photoencapsulated in PEG hydrogels. *Journal of Biomedical Materials Research Part A* **2004**, 68A, (4), 773 - 782.
75. Bryant, S. J.; Bender, R. J.; Durand, K. L.; Anseth, K. S., Encapsulating chondrocytes in degrading PEG hydrogels with high modulus: Engineering gel structural changes to facilitate cartilaginous tissue production. *Biotechnology and Bioengineering* **2004**, 86, (7), 747 - 755.
76. Weber, L. M.; He, J.; Bradley, B.; Haskins, K.; Anseth, K. S., PEG-based hydrogels as an in vitro encapsulation platform for testing controlled β -cell microenvironments. *Acta Biomaterialia* **2006**, 2, (1), 1-8.
77. Madihally, S. V.; Matthew, H. W., Porous chitosan scaffolds for tissue engineering. *Biomaterials* **1999**, 20, (12), 1133-42.
78. Tissue engineering. *Nat Biotechnol* **2000**, 18 Suppl, IT56-8.

79. Balgude, A. P.; Yu, X.; Szymanski, A.; Bellamkonda, R. V., Agarose gel stiffness determines rate of DRG neurite extension in 3D cultures. *Biomaterials* **2001**, 22, (10), 1077-84.
80. Dar, A.; Shachar, M.; Leor, J.; Cohen, S., Optimization of cardiac cell seeding and distribution in 3D porous alginate scaffolds. *Biotechnol Bioeng* **2002**, 80, (3), 305-12.
81. Ranucci, C. S.; Moghe, P. V., Substrate microtopography can enhance cell adhesive and migratory responsiveness to matrix ligand density. *J Biomed Mater Res* **2001**, 54, (2), 149-61.
82. Zeltinger, J.; Sherwood, J. K.; Graham, D. A.; Mueller, R.; Griffith, L. G., Effect of pore size and void fraction on cellular adhesion, proliferation, and matrix deposition. *Tissue Eng* **2001**, 7, (5), 557-72.
83. Rajnicek, A.; Britland, S.; McCaig, C., Contact guidance of CNS neurites on grooved quartz: influence of groove dimensions, neuronal age and cell type. *J Cell Sci* **1997**, 110, (Pt 23), 2905-13.
84. Chung, T. W.; Lu, Y. F.; Wang, S. S.; Lin, Y. S.; Chu, S. H., Growth of human endothelial cells on photochemically grafted Gly-Arg-Gly-Asp (GRGD) chitosans. *Biomaterials* **2002**, 23, (24), 4803-9.
85. Curtis, A.; Wilkinson, C., New depths in cell behaviour: reactions of cells to nanotopography. *Biochem Soc Symp* **1999**, 65, 15-26.
86. Huang, Y., Influence of Scaffold Properties on Cellular Colonization for Tissue Engineering. *PhD Dissertation* **2005**.
87. Freed, L. E.; Vunjak-Novakovic, G.; Biron, R. J.; Eagles, D. B.; Lesnoy, D. C.; Barlow, S. K.; Langer, R., Biodegradable polymer scaffolds for tissue engineering. *Biotechnology (N Y)* **1994**, 12, (7), 689-93.
88. Ishaug-Riley, S. L.; Crane-Kruger, G. M.; Yaszemski, M. J.; Mikos, A. G., Three-dimensional culture of rat calvarial osteoblasts in porous biodegradable polymers. *Biomaterials* **1998**, 19, (15), 1405-12.
89. Agrawal, C. M.; Ray, R. B., Biodegradable polymeric scaffolds for musculoskeletal tissue engineering. *J Biomed Mater Res* **2001**, 55, (2), 141-50.
90. Marois, Y.; Sigot-Luizard, M. F.; Guidoin, R., Endothelial cell behavior on vascular prosthetic grafts: effect of polymer chemistry, surface structure, and surface treatment. *Asaio J* **1999**, 45, (4), 272-80.
91. Miot, S.; Woodfield, T.; Daniels, A. U.; Suetterlin, R.; Peterschmitt, I.; Heberer, M.; van Blitterswijk, C. A.; Riesle, J.; Martin, I., Effects of scaffold composition and architecture on human nasal chondrocyte redifferentiation and cartilaginous matrix deposition. *Biomaterials* **2005**, 26, (15), 2479-2489.
92. Sodian, R.; Hoerstrup, S. P.; Sperling, J. S.; Martin, D. P.; Daebritz, S.; Mayer, J. E., Jr.; Vacanti, J. P., Evaluation of biodegradable, three-dimensional matrices for tissue engineering of heart valves. *Asaio J* **2000**, 46, (1), 107-10.
93. Zhang, H.; Cooper, A. I., Aligned Porous Structures by Directional Freezing. *Advanced Materials* **2007**, 19, (11), 1529-1533.
94. O'Brien, F. J.; Harley, B. A.; Yannas, I. V.; Gibson, L. J., The effect of pore size on cell adhesion in collagen-GAG scaffolds. *Biomaterials* **2005**, 26, 433-441.
95. Teebken, O. E.; Haverich, A., Tissue engineering of small diameter vascular grafts. *Eur J Vasc Endovasc Surg* **2002**, 23, (6), 475-85.

96. Yannas, I. V.; Lee, E.; Orgill, D. P.; Skrabut, E. M.; Murphy, G. F., Synthesis and characterization of a model extracellular matrix that induces partial regeneration of adult mammalian skin. *Proc Natl Acad Sci U S A* **1989**, 86, (3), 933-7.
97. Zeltinger, J.; Sherwood, J. K.; Graham, D. A.; Mueller, R.; Griffith, L. G., Effect of pore size and void fraction on cellular adhesion, proliferation, and matrix deposition. *Tissue Engineering* **2001**, 7, (5), 557-572.
98. Salem, A. K.; Stevens, R.; Pearson, R. G.; Davies, M. C.; Tendler, S. J.; Roberts, C. J.; Williams, P. M.; Shakesheff, K. M., Interactions of 3T3 fibroblasts and endothelial cells with defined pore features. *J Biomed Mater Res* **2002**, 61, (2), 212-7.
99. Ng, K. W.; Khor, H. L.; Hutmacher, D. W., In vitro characterization of natural and synthetic dermal matrices cultured with human dermal fibroblasts. *Biomaterials* **2004**, 25, (14), 2807-18.
100. Wang, Y. C.; Ho, C. C., Micropatterning of proteins and mammalian cells on biomaterials. *Faseb J* **2004**, 18, (3), 525-7. Epub 2004 Jan 8.
101. Doi, K.; Nakayama, Y.; Matsuda, T., Novel compliant and tissue-permeable microporous polyurethane vascular prosthesis fabricated using an excimer laser ablation technique. *J Biomed Mater Res* **1996**, 31, (1), 27-33.
102. Sachlos, E.; Czernuszka, J. T., Making Tissue Engineering Scaffolds Work. Review: The application of solid freeform fabrication technology to the production of tissue engineering scaffolds. *European Cells and Materials Journal* **2003**, 5, 29-40.
103. Ranucci, C. S.; Kumar, A.; Batra, S. P.; Moghe, P. V., Control of hepatocyte function on collagen foams: sizing matrix pores toward selective induction of 2-D and 3-D cellular morphogenesis. *Biomaterials* **2000**, 21, (8), 783-93.
104. Clarke, K. M.; Lantz, G. C.; Salisbury, S. K.; Badylak, S. F.; Hiles, M. C.; Voytik, S. L., Intestine Submucosa and Polypropylene Mesh for Abdominal Wall Repair in Dogs. *Journal of Surgical Research* **1996**, 60, (1), 107-114.
105. Walboomers, X. F.; Croes, H. J.; Ginsel, L. A.; Jansen, J. A., Contact guidance of rat fibroblasts on various implant materials. *J Biomed Mater Res* **1999**, 47, (2), 204-12.
106. Lampin, M.; Warocquier, C.; Legris, C.; Degrange, M.; Sigot-Luizard, M. F., Correlation between substratum roughness and wettability, cell adhesion, and cell migration. *J Biomed Mater Res* **1997**, 36, (1), 99-108.
107. Pattison, M. A.; Wurster, S.; Webster, T. J.; Haberstroh, K. M., Three-dimensional, nano-structured PLGA scaffolds for bladder tissue replacement applications. *Biomaterials* **2005**, 26, (15), 2491-2500.
108. Park, G. E.; Pattison, M. A.; Park, K.; Webster, T. J., Accelerated chondrocyte functions on NaOH-treated PLGA scaffolds. *Biomaterials* **2005**, 26, (16), 3075-3082.
109. Mondalek, F. G.; Lawrence, B. J.; Kropp, B. P.; Grady, B. P.; Fung, K.-M.; Madihally, S. V.; Lin, H.-K., The incorporation of poly(lactic-co-glycolic) acid nanoparticles into porcine small intestinal submucosa biomaterials. *Biomaterials* **2008**, 29, (9), 1159-1166.
110. Sarasam, A.; Madihally, S. V., Characterization of chitosan-polycaprolactone blends for tissue engineering applications. *Biomaterials* **2005**, 26, (27), 5500-8.
111. Sarasam, A. R.; Krishnaswamy, R. K.; Madihally, S. V., Blending Chitosan with Polycaprolactone: Effects on Physicochemical and Antibacterial Properties. *Biomacromolecules* **2006**, 7, (4), 1131-1138.

112. Tillman, J.; Ullm, A.; Madihally, S. V., Three-dimensional cell colonization in a sulfate rich environment. *Biomaterials* **2006**, 27, (32), 5618-5626.
113. VandeVondele, S.; Vörös, J.; Hubbell, J. A., RGD-grafted poly-l-lysine-*g*-(polyethylene glycol) copolymers block non-specific protein adsorption while promoting cell adhesion. *Biotechnology and Bioengineering* **2003**, 82, (7), 784-790.
114. Nomi, M.; Atala, A.; Coppi, P. D.; Soker, S., Principals of neovascularization for tissue engineering. *Molecular Aspects of Medicine* **2002**, 23, (6), 463-483.
115. Laschke, M. W.; Harder, Y.; Amon, M.; Martin, I.; Farhadi, J.; Ring, A.; Torio-Padron, N.; Schramm, R.; Rucker, M.; Junker, D.; Haufel, J. M.; Carvalho, C.; Heberer, M.; Germann, G.; Vollmar, B.; Menger, M. D., Angiogenesis in Tissue Engineering: Breathing Life into Constructed Tissue Substitutes. *Tissue Engineering* **2006**, 12, (8), 2093-2104.
116. Vogel, V.; Baneyx, G., THE TISSUE ENGINEERING PUZZLE: A Molecular Perspective. *Annual Review of Biomedical Engineering* **2003**, 5, (1), 441-463.
117. Birgersdotter, A.; Sandberg, R.; Ernberg, I., Gene expression perturbation in vitro--A growing case for three-dimensional (3D) culture systems. *Seminars in Cancer Biology* **2005**, 15, (5), 405-412.
118. Yamada, K. M.; Pankov, R.; Cukierman, E., Dimensions and dynamics in integrin function. *Braz J Med Biol Res* **2003**, 36, (8), 959-66. Epub 2003 Jul 23.
119. Wozniak, M. A.; Modzelewska, K.; Kwong, L.; Keely, P. J., Focal adhesion regulation of cell behavior. *Biochim Biophys Acta* **2004**, 1692, (2-3), 103-19.
120. Sato, H.; Takahashi, M.; Ise, H.; Yamada, A.; Hirose, S.; Tagawa, Y.; Morimoto, H.; Izawa, A.; Ikeda, U., Collagen synthesis is required for ascorbic acid-enhanced differentiation of mouse embryonic stem cells into cardiomyocytes. *Biochem Biophys Res Commun* **2006**, 342, (1), 107-12.
121. Chang, Z.; Meyer, K.; Rapraeger, A. C.; Friedl, A., Differential ability of heparan sulfate proteoglycans to assemble the fibroblast growth factor receptor complex in situ. *Faseb J* **2000**, 14, (1), 137-44.
122. Cukierman, E.; Pankov, R.; Stevens, D. R.; Yamada, K. M., Taking cell-matrix adhesions to the third dimension. *Science* **2001**, 294, (5547), 1708-12.
123. Chen, H.-C.; Hu, Y.-C., Bioreactors for tissue engineering. *Biotechnology Letters* **2006**, 28, (18), 1415-1423.
124. Grashow, J.; Yoganathan, A.; Sacks, M., Biaxial Stress–Stretch Behavior of the Mitral Valve Anterior Leaflet at Physiologic Strain Rates. *Annals of Biomedical Engineering* **2006**, 34, (2), 315-325.
125. Gray, M. L.; Pizzanelli, A. M.; Grodzinsky, A. J.; Lee, R. C., Mechanical and physicochemical determinants of the chondrocyte biosynthetic response. *Journal of Orthopaedic Research* **1988**, 6, (6), 777-792.
126. Papadaki, M.; Eskin, S. G.; Ruef, J.; Runge, M. S.; McIntire, L. V., Fluid shear stress as a regulator of gene expression in vascular cells: possible correlations with diabetic abnormalities. *Diabetes Research and Clinical Practice* **1999**, 45, (2-3), 89-99.
127. Takahashi, M.; Berk, B. C., Mitogen-activated Protein Kinase (ERK1/2) Activation by Shear Stress and Adhesion in Endothelial Cells . Essential Role for a Herbimycin-sensitive Kinase. *J. Clin. Invest.* **1996**, 98, (11), 2623-2631.

128. Chen, K.-D.; Li, Y.-S.; Kim, M.; Li, S.; Yuan, S.; Chien, S.; Shyy, J. Y.-J., Mechanotransduction in Response to Shear Stress. ROLES OF RECEPTOR TYROSINE KINASES, INTEGRINS, AND Shc. *J. Biol. Chem.* **1999**, 274, (26), 18393-18400.
129. Burridge, K.; Chrzanowska-Wodnicka, M., Focal adhesions, contractility, and signaling. *Annual Review Of Cell And Developmental Biology* **1996**, 12, 463-518.
130. Gu, J.; Tamura, M.; Pankov, R.; Danen, E. H. J.; Takino, T.; Matsumoto, K.; Yamada, K. M., Shc and FAK Differentially Regulate Cell Motility and Directionality Modulated by PTEN. *J. Cell Biol.* **1999**, 146, (2), 389-404.
131. Ingber, D. E., Cellular mechanotransduction: putting all the pieces together again. *FASEB J.* **2006**, 20, (7), 811-827.
132. Gomes, M. E.; Sikavitsas, V. I.; Behraves, E.; Reis, R. L.; Mikos, A. G., Effect of flow perfusion on the osteogenic differentiation of bone marrow stromal cells cultured on starch-based three-dimensional scaffolds. *Journal of Biomedical Materials Research Part A* **2003**, 67A, (1), 87-95.
133. Zaleskas, J. M.; Kinner, B.; Freyman, T. M.; Yannas, I. V.; Gibson, L. J.; Spector, M., Growth factor regulation of smooth muscle actin expression and contraction of human articular chondrocytes and meniscal cells in a collagen-GAG matrix. *Exp Cell Res* **2001**, 270, (1), 21-31.
134. Lee, C. R.; Grodzinsky, A. J.; Spector, M., The effects of cross-linking of collagen-glycosaminoglycan scaffolds on compressive stiffness, chondrocyte-mediated contraction, proliferation and biosynthesis. *Biomaterials* **2001**, 22, (23), 3145-54.
135. Sieminski, A. L.; Hebbel, R. P.; Gooch, K. J., The relative magnitudes of endothelial force generation and matrix stiffness modulate capillary morphogenesis in vitro. *Exp Cell Res* **2004**, 297, (2), 574-84.
136. Lo, C. M.; Wang, H. B.; Dembo, M.; Wang, Y. L., Cell movement is guided by the rigidity of the substrate. *Biophys J* **2000**, 79, (1), 144-52.
137. Pelham, R. J., Jr.; Wang, Y., Cell locomotion and focal adhesions are regulated by substrate flexibility. *Proc Natl Acad Sci U S A* **1997**, 94, (25), 13661-5.
138. Trelstad, R. L.; Hayashi, K., Tendon collagen fibrillogenesis: intracellular subassemblies and cell surface changes associated with fibril growth. *Dev Biol* **1979**, 71, (2), 228-42.
139. Hsieh, P.; Chen, L. B., Behavior of cells seeded in isolated fibronectin matrices. *J Cell Biol* **1983**, 96, (5), 1208-17.
140. Tranquillo, R. T.; Murray, J. D., Continuum model of fibroblast-driven wound contraction: inflammation-mediation. *Journal Of Theoretical Biology* **1992**, 158, (2), 135-172.
141. Dallan, J. C.; Sherratt, J. A.; Maini, P. K., Mathematical Modelling of Extracellular Matrix Dynamics using Discrete Cells: Fiber Orientation and Tissue Regeneration. *Journal of Theoretical Biology* **1999**, 199, (4), 449-471.
142. Dunn, M. G.; Doillon, C. J.; Berg, R. A.; Olson, R. M.; Silver, F. H., Wound healing using a collagen matrix: effect of DC electrical stimulation. *J Biomed Mater Res* **1988**, 22, (A2 Suppl), 191-206.
143. Inoue, M.; Ono, I.; Tateshita, T.; Kuroyanagi, Y.; Shioya, N., Effect of a collagen matrix containing epidermal growth factor on wound contraction. *Wound Repair Regen* **1998**, 6, (3), 213-22.

144. Ono, I.; Tateshita, T.; Inoue, M., Effects of a collagen matrix containing basic fibroblast growth factor on wound contraction. *J Biomed Mater Res* **1999**, 48, (5), 621-30.
145. Doillon, C. J.; Silver, F. H.; Olson, R. M.; Kamath, C. Y.; Berg, R. A., Fibroblast and epidermal cell-type I collagen interactions: cell culture and human studies. *Scanning Microsc* **1988**, 2, (2), 985-92.
146. Doillon, C. J.; Silver, F. H., Collagen-based wound dressing: effects of hyaluronic acid and fibronectin on wound healing. *Biomaterials* **1986**, 7, (1), 3-8.
147. Smeds, K. A.; Grinstaff, M. W., Photocrosslinkable polysaccharides for <I>in situ</I> hydrogel formation. *Journal of Biomedical Materials Research* **2001**, 54, (1), 115-121.
148. Zisch, A. H.; Lutolf, M. P.; Ehrbar, M.; Raeber, G. P.; Rizzi, S. C.; Davies, N.; Schmokel, H.; Bezuidenhout, D.; Djonov, V.; Zilla, P.; Hubbell, J. A., Cell-demanded release of VEGF from synthetic, biointeractive cell-ingrowth matrices for vascularized tissue growth. *The FASEB Journal* **2003**, 02-1041fje.
149. D'Amore, P. A.; Thompson, R. W., Mechanisms of angiogenesis. *ANNU. REV. PHYSIOL.* **1987**, Vol. 49, 453-464.
150. Folkman, J.; Klagsbrun, M., Angiogenic factors. *Science* **1987**, 235, (4787), 442-7.
151. Galeano, M.; Deodato, B.; Altavilla, D.; Squadrito, G.; Seminara, P.; Marini, H.; Stagno d'Alcontres, F.; Colonna, M.; Calo, M.; Lo Cascio, P.; Torre, V.; Giacca, M.; Venuti, F. S.; Squadrito, F., Effect of recombinant adeno-associated virus vector-mediated vascular endothelial growth factor gene transfer on wound healing after burn injury. *Crit Care Med* **2003**, 31, (4), 1017-25.
152. Li, J.; Zhang, Y. P.; Kirsner, R. S., Angiogenesis in wound repair: angiogenic growth factors and the extracellular matrix. *Microsc Res Tech* **2003**, 60, (1), 107-14.
153. Nelson, A. R.; Fingleton, B.; Rothenberg, M. L.; Matrisian, L. M., Matrix Metalloproteinases: Biologic Activity and Clinical Implications. *J Clin Oncol* **2000**, 18, (5), 1135-.
154. Fosang, A. J.; Last, K.; Maciewicz, R. A., AggreCAN Is Degraded by Matrix Metalloproteinases in Human Arthritis . Evidence That Matrix Metalloproteinase and AggreCANase Activities Can Be Independent. *J. Clin. Invest.* **1996**, 98, (10), 2292-2299.
155. Makowski, G. S.; Ramsby, M. L., Identification and partial characterization of three calcium- and zinc-independent gelatinases constitutively present in human circulation. *Biochem Mol Biol Int* **1998**, 46, (5), 1043-53.
156. Schonherr, E.; Schaefer, L.; O'Connell, B. C.; Kresse, H., Matrix metalloproteinase expression by endothelial cells in collagen lattices changes during co-culture with fibroblasts and upon induction of decorin expression. *J Cell Physiol* **2001**, 187, (1), 37-47.
157. Visse, R.; Nagase, H., Matrix metalloproteinases and tissue inhibitors of metalloproteinases: structure, function, and biochemistry. *Circ Res* **2003**, 92, (8), 827-39.
158. Park, Y.; Lutolf, M. P.; Hubbell, J. A.; Hunziker, E. B.; Wong, M., Bovine primary chondrocyte culture in synthetic matrix metalloproteinase-sensitive poly(ethylene glycol)-based hydrogels as a scaffold for cartilage repair. *Tissue Eng* **2004**, 10, (3-4), 515-22.

159. Sperger, J. M.; Chen, X.; Draper, J. S.; Antosiewicz, J. E.; Chon, C. H.; Jones, S. B.; Brooks, J. D.; Andrews, P. W.; Brown, P. O.; Thomson, J. A., Gene expression patterns in human embryonic stem cells and human pluripotent germ cell tumors. *PNAS* **2003**, 100, (23), 13350-13355.
160. Malafaya, P. B.; Silva, G. A.; Reis, R. L., Natural-origin polymers as carriers and scaffolds for biomolecules and cell delivery in tissue engineering applications. *Advanced Drug Delivery Reviews* **2007**, 59, (4-5), 207-233.
161. Yang, J.; Goto, M.; Ise, H.; Cho, C.-S.; Akaike, T., Galactosylated alginate as a scaffold for hepatocytes entrapment. *Biomaterials* **2002**, 23, (2), 471-479.
162. Bouhadir, K. H.; Lee, K. Y.; Alsberg, E.; Damm, K. L.; Anderson, K. W.; Mooney, D. J., Degradation of partially oxidized alginate and its potential application for tissue engineering. *Biotechnol Prog* **2001**, 17, (5), 945-50.
163. Tan, W.; Krishnaraj, R.; Desai, T. A., Evaluation of nanostructured composite collagen--chitosan matrices for tissue engineering. *Tissue Eng* **2001**, 7, (2), 203-10.
164. Mizuno, K.; Yamamura, K.; Yano, K.; Osada, T.; Saeki, S.; Takimoto, N.; Sakurai, T.; Nimura, Y., Effect of chitosan film containing basic fibroblast growth factor on wound healing in genetically diabetic mice. *J Biomed Mater Res* **2003**, 64, (1), 177-81.
165. Zhu, H.; Ji, J.; Lin, R.; Gao, C.; Feng, L.; Shen, J., Surface engineering of poly(D,L-lactic acid) by entrapment of chitosan-based derivatives for the promotion of chondrogenesis. *J Biomed Mater Res* **2002**, 62, (4), 532-9.
166. Chung, T. W.; Yang, J.; Akaike, T.; Cho, K. Y.; Nah, J. W.; Kim, S. I.; Cho, C. S., Preparation of alginate/galactosylated chitosan scaffold for hepatocyte attachment. *Biomaterials* **2002**, 23, (14), 2827-34.
167. Cai, K.; Yao, K.; Cui, Y.; Lin, S.; Yang, Z.; Li, X.; Xie, H.; Qing, T.; Luo, J., Surface modification of poly (D,L-lactic acid) with chitosan and its effects on the culture of osteoblasts in vitro. *J Biomed Mater Res* **2002**, 60, (3), 398-404.
168. Lahiji, A.; Sohrabi, A.; Hungerford, D. S.; Frondoza, C. G., Chitosan supports the expression of extracellular matrix proteins in human osteoblasts and chondrocytes. *J Biomed Mater Res* **2000**, 51, (4), 586-95.
169. Singla, A.; Lee, C. H., Effect of elastin on the calcification rate of collagen-elastin matrix systems. *J Biomed Mater Res* **2002**, 60, (3), 368-74.
170. Dantzer, E.; Braye, F. M., Reconstructive surgery using an artificial dermis (Integra): results with 39 grafts. *Br J Plast Surg* **2001**, 54, (8), 659-64.
171. Orgill, D. P.; Straus, F. H., 2nd; Lee, R. C., The use of collagen-GAG membranes in reconstructive surgery. *Ann N Y Acad Sci* **1999**, 888, 233-48.
172. Xiao, Y.; Qian, H.; Young, W. G.; Bartold, P. M., Tissue engineering for bone regeneration using differentiated alveolar bone cells in collagen scaffolds. *Tissue Eng* **2003**, 9, (6), 1167-77.
173. Mao, J. S.; liu, H. F.; Yin, Y. J.; Yao, K. D., The properties of chitosan-gelatin membranes and scaffolds modified with hyaluronic acid by different methods. *Biomaterials* **2003**, 24, (9), 1621-9.
174. Santhosh Kumar, T. R.; Krishnan, L. K., Endothelial cell growth factor (ECGF) enmeshed with fibrin matrix enhances proliferation of EC in vitro. *Biomaterials* **2001**, 22, (20), 2769-76.

175. Bensai, d, W.; Triffitt, J. T.; Blanchat, C.; Oudina, K.; Sedel, L.; Petite, H., A biodegradable fibrin scaffold for mesenchymal stem cell transplantation. *Biomaterials* **2003**, 24, (14), 2497-2502.
176. Jockenhoevel, S.; Chalabi, K.; Sachweh, J. S.; Groesdonk, H. V.; Demircan, L.; Grossmann, M.; Zund, G.; Messmer, B. J., Tissue engineering: complete autologous valve conduit--a new moulding technique. *Thorac Cardiovasc Surg* **2001**, 49, (5), 287-90.
177. Mooney, D.; Hansen, L.; Vacanti, J.; Langer, R.; Farmer, S.; Ingber, D., Switching from differentiation to growth in hepatocytes: control by extracellular matrix. *Journal Of Cellular Physiology* **1992**, 151, (3), 497-505.
178. Lindahl, U.; Kusche-Gullberg, M.; Kjellen, L., Regulated diversity of heparan sulfate. *J Biol Chem* **1998**, 273, (39), 24979-82.
179. Babu, M.; Diegelmann, R.; Oliver, N., Fibronectin is overproduced by keloid fibroblasts during abnormal wound healing. *Mol Cell Biol* **1989**, 9, (4), 1642-50.
180. Denuziere, A.; Ferrier, D.; Damour, O.; Domard, A., Chitosan-chondroitin sulfate and chitosan-hyaluronate polyelectrolyte complexes: biological properties. *Biomaterials* **1998**, 19, (14), 1275-85.
181. Lamme, E. N.; de Vries, H. J.; van Veen, H.; Gabbiani, G.; Westerhof, W.; Middelkoop, E., Extracellular matrix characterization during healing of full-thickness wounds treated with a collagen/elastin dermal substitute shows improved skin regeneration in pigs. *J Histochem Cytochem* **1996**, 44, (11), 1311-22.
182. Garg, H. G.; Lippay, E. W.; Carter, E. A.; Donelan, M. B.; Remensnyder, J. P., Proteoglycan synthesis in human skin and burn scar explant cultures. *Burns* **1991**, 17, (6), 452-7.
183. Rothenburger, M.; Vischer, P.; Volker, W.; Glasmacher, B.; Berendes, E.; Scheld, H. H.; Deiwick, M., In vitro modelling of tissue using isolated vascular cells on a synthetic collagen matrix as a substitute for heart valves. *Thorac Cardiovasc Surg* **2001**, 49, (4), 204-9.
184. Yannas, I. V., Models of organ regeneration processes induced by templates. *Ann N Y Acad Sci* **1997**, 831, 280-93.
185. Spilker, M. H.; Asano, K.; Yannas, I. V.; Spector, M., Contraction of collagen-glycosaminoglycan matrices by peripheral nerve cells in vitro. *Biomaterials* **2001**, 22, (10), 1085-93.
186. Kessler, P. D.; Byrne, B. J., Myoblast cell grafting into heart muscle: cellular biology and potential applications. *Annu Rev Physiol* **1999**, 61, 219-42.
187. Taylor, P. M.; Allen, S. P.; Dreger, S. A.; Yacoub, M. H., Human cardiac valve interstitial cells in collagen sponge: a biological three-dimensional matrix for tissue engineering. *J Heart Valve Dis* **2002**, 11, (3), 298-306; discussion 306-7.
188. Pieper, J. S.; Hafmans, T.; van Wachem, P. B.; van Luyn, M. J.; Brouwer, L. A.; Veerkamp, J. H.; van Kuppevelt, T. H., Loading of collagen-heparan sulfate matrices with bFGF promotes angiogenesis and tissue generation in rats. *J Biomed Mater Res* **2002**, 62, (2), 185-94.
189. Suh, J. K.; Matthew, H. W., Application of chitosan-based polysaccharide biomaterials in cartilage tissue engineering: a review. *Biomaterials* **2000**, 21, (24), 2589-98.

190. Malafaya, P. B.; Pedro, A. J.; Peterbauer, A.; Gabriel, C.; Redl, H.; Reis, R. L., Chitosan particles agglomerated scaffolds for cartilage and osteochondral tissue engineering approaches with adipose tissue derived stem cells. *Journal of Materials Science: Materials in Medicine* **2005**, 16, (12), 1077 - 1085.
191. Wang, X. H.; Li, D. P.; Wang, W. J.; Feng, Q. L.; Cui, F. Z.; Xu, Y. X.; Song, X. H.; van der Werf, M., Crosslinked collagen/chitosan matrix for artificial livers. *Biomaterials* **2003**, 24, (19), 3213-20.
192. Park, I. K.; Yang, J.; Jeong, H. J.; Bom, H. S.; Harada, I.; Akaike, T.; Kim, S. I.; Cho, C. S., Galactosylated chitosan as a synthetic extracellular matrix for hepatocytes attachment. *Biomaterials* **2003**, 24, (13), 2331-7.
193. Yuan, Y.; Zhang, P.; Yang, Y.; Wang, X.; Gu, X., The interaction of Schwann cells with chitosan membranes and fibers in vitro. *Biomaterials* **2004**, 25, (18), 4273-4278.
194. Wenling, C.; Duohui, J.; Jiamou, L.; Yandao, G.; Nanming, Z.; Xiufang, Z., Effects of the degree of deacetylation on the physicochemical properties and Schwann cell affinity of chitosan films. *Journal of biomaterials applications* **2005**, 20, (2), 157-77.
195. Ehrenfreund-Kleinman, T.; A.J., D.; Golenser, J., Polysaccharide Scaffolds Prepared by Crosslinking of Polysaccharides with Chitosan or Proteins for Cell Growth. *J Bioact Compat Polym* **2003**, 18, (5), 323-338.
196. Mei, N.; Chen, G.; Zhou, P.; Chen, X.; Shao, Z. Z.; Pan, L. F.; Wu, C. G., Biocompatibility of Poly(epsilon-caprolactone) scaffold modified by chitosan--the fibroblasts proliferation in vitro. *J Biomater Appl* **2005**, 19, (4), 323-39.
197. Lee, J. Y.; Spicer, A. P., Hyaluronan: a multifunctional, megaDalton, stealth molecule. *Curr Opin Cell Biol* **2000**, 12, (5), 581-6.
198. Tadmor, R.; Chen, N.; Israelachvili, J. N., Thin film rheology and lubricity of hyaluronic acid solutions at a normal physiological concentration. *J Biomed Mater Res* **2002**, 61, (4), 514-23.
199. Seal, B. L.; Otero, T. C.; Panitch, A., Polymeric biomaterials for tissue and organ regeneration. *Materials Science and Engineering* **2001**, 34, 147-230.
200. Jyrki, H., The collagen family members as cell adhesion proteins. *BioEssays* **2007**, 29, (10), 1001-1010.
201. Xue, L.; Greisler, H. P., Biomaterials in the development and future of vascular grafts. *J Vasc Surg* **2003**, 37, (2), 472-80.
202. Tam, E. M.; Wu, Y. I.; Butler, G. S.; Stack, M. S.; Overall, C. M., Collagen binding properties of the membrane type-1 matrix metalloproteinase (MT1-MMP) hemopexin C domain. The ectodomain of the 44-kDa autocatalytic product of MT1-MMP inhibits cell invasion by disrupting native type I collagen cleavage. *J Biol Chem* **2002**, 277, (41), 39005-14. Epub 2002 Jul 26.
203. Almarza, A. J.; Athanasiou, K. A., Design Characteristics for the Tissue Engineering of Cartilaginous Tissues. *Annals of Biomedical Engineering* **2004**, 32, (1), 2-17.
204. Bryant, S. J.; Anseth, K. S., Controlling the spatial distribution of ECM components in degradable PEG hydrogels for tissue engineering cartilage. *Journal of Biomedical Materials Research Part A* **2003**, 64A, (1), 70-79.
205. Mao, J.; Zhao, L.; De Yao, K.; Shang, Q.; Yang, G.; Cao, Y., Study of novel chitosan-gelatin artificial skin in vitro. *J Biomed Mater Res* **2003**, 64A, (2), 301-8.

206. Young, S.; Wong, M.; Tabata, Y.; Mikos, A. G., Gelatin as a delivery vehicle for the controlled release of bioactive molecules. *Journal of Controlled Release* **2005**, 109, (1-3), 256-274.
207. Tabata, Y.; Ikada, Y., Vascularization effect of basic fibroblast growth factor released from gelatin hydrogels with different biodegradabilities. *Biomaterials* **1999**, 20, (22), 2169-2175.
208. Yang, L.-J.; Ou, Y.-C., The micro patterning of glutaraldehyde (GA)-crosslinked gelatin and its application to cell-culture. *Lab on a Chip* **2005**, 5, (9), 979-984.
209. Chang, M.; Douglas, W., Cross-linkage of hydroxyapatite/gelatin nanocomposite using imide-based zero-length cross-linker. *Journal of Materials Science: Materials in Medicine* **2007**, 18, (10), 2045-2051.
210. Westreich, R.; Kaufman, M.; Gannon, P.; Lawson, W., Validating the subcutaneous model of injectable autologous cartilage using a fibrin glue scaffold. *Laryngoscope* **2004**, 114, (12), 2154-60.
211. Ting, V.; Sims, C. D.; Brecht, L. E.; McCarthy, J. G.; Kasabian, A. K.; Connelly, P. R.; Elisseff, J.; Gittes, G. K.; Longaker, M. T., In vitro prefabrication of human cartilage shapes using fibrin glue and human chondrocytes. *Ann Plast Surg* **1998**, 40, (4), 413-20; discussion 420-1.
212. Hutmacher, D. W.; Schantz, T.; Zein, I.; Ng, K. W.; Teoh, S. H.; Tan, K. C., Mechanical properties and cell cultural response of polycaprolactone scaffolds designed and fabricated via fused deposition modeling. *J Biomed Mater Res* **2001**, 55, (2), 203-16.
213. Lowry, K. J.; Hamson, K. R.; Bear, L.; Peng, Y. B.; Calaluce, R.; Evans, M. L.; Anglen, J. O.; Allen, W. C., Polycaprolactone/glass bioabsorbable implant in a rabbit humerus fracture model. *J Biomed Mater Res* **1997**, 36, (4), 536-41.
214. Saito, N.; Okada, T.; Toba, S.; Miyamoto, S.; Takaoka, K., New synthetic absorbable polymers as BMP carriers: plastic properties of poly-D,L-lactic acid-polyethylene glycol block copolymers. *J Biomed Mater Res* **1999**, 47, (1), 104-10.
215. Ho, K. L.; Witte, M. N.; Bird, E. T., 8-ply small intestinal submucosa tension-free sling: spectrum of postoperative inflammation. *J Urol* **2004**, 171, (1), 268-71.
216. Pistner, H.; Bendix, D. R.; Muhling, J.; Reuther, J. F., Poly(L-lactide): a long-term degradation study in vivo. Part III. Analytical characterization. *Biomaterials* **1993**, 14, (4), 291-8.
217. Kranz, H.; Ubrich, N.; Maincent, P.; Bodmeier, R., Physicomechanical properties of biodegradable poly(D,L-lactide) and poly(D,L-lactide-co-glycolide) films in the dry and wet states. *J Pharm Sci* **2000**, 89, (12), 1558-66.
218. Yoon, J. J.; Park, T. G., Degradation behaviors of biodegradable macroporous scaffolds prepared by gas foaming of effervescent salts. *J Biomed Mater Res* **2001**, 55, (3), 401-8.
219. Lu, L.; Peter, S. J.; Lyman, M. D.; Lai, H. L.; Leite, S. M.; Tamada, J. A.; Uyama, S.; Vacanti, J. P.; Langer, R.; Mikos, A. G., In vitro and in vivo degradation of porous poly(DL-lactic-co-glycolic acid) foams. *Biomaterials* **2000**, 21, (18), 1837-45.
220. Sokolsky-Papkov, M.; Agashi, K.; Olaye, A.; Shakesheff, K. M.; Domb, A. J., Polymer carriers for drug delivery in tissue engineering. *Advanced Drug Delivery Reviews* **2007**, 59, (4-5), 187-206.

221. Sarasam, A.; Brown, P.; Khajotia, S.; Dmytryk, J.; Madihally, S., Antibacterial activity of chitosan-based matrices on oral pathogens. *Journal of Materials Science: Materials in Medicine* **2008**, 19, (3), 1083-1090.
222. Middleton, J. C.; Tipton, A. J., Synthetic biodegradable polymers as orthopedic devices. *Biomaterials* **2000**, 21, (23), 2335-46.
223. Averous, L.; Moro, L.; Dole, P.; Fringant, C., Properties of thermoplastic blends: starch-polycaprolactone. *POLYMER* **2000**, 41, (11), 4157-4167.
224. Tessmar, J. K.; Göpferich, A. M., Customized PEG-Derived Copolymers for Tissue-Engineering Applications. *Macromolecular Bioscience* **2007**, 7, (1), 23-39.
225. Davis, K. A.; Burdick, J. A.; Anseth, K. S., Photoinitiated crosslinked degradable copolymer networks for tissue engineering applications. *Biomaterials* **2003**, 24, (14), 2485-2495.
226. Weber, L. M.; Cheung, C. Y.; Anseth, K. S., Multifunctional Pancreatic Islet Encapsulation Barriers Achieved Via Multilayer PEG Hydrogels. *Cell Transplantation* **2008**, 16, 1049-1057.
227. Massia, S. P.; Hubbell, J. A., Covalently attached GRGD on polymer surfaces promotes biospecific adhesion of mammalian cells. *Ann N Y Acad Sci* **1990**, 589, 261-70.
228. Agrawal, C. M.; Athanasiou, K. A., Technique to control pH in vicinity of biodegrading PLA-PGA implants. *J Biomed Mater Res* **1997**, 38, (2), 105-14.
229. Park, A.; Wu, B.; Griffith, L. G., Integration of surface modification and 3D fabrication techniques to prepare patterned poly(L-lactide) substrates allowing regionally selective cell adhesion. *J Biomater Sci Polym Ed* **1998**, 9, (2), 89-110.
230. Eid, K.; Chen, E.; Griffith, L.; Glowacki, J., Effect of RGD coating on osteocompatibility of PLGA-polymer disks in a rat tibial wound. *J Biomed Mater Res* **2001**, 57, (2), 224-31.
231. Moshfegian, A.; Tillman, J.; Madihally, S., Characterization of Emulsified Chitosan-PLGA Matrices Formed Using Controlled Rate Freezing and Lyophilization Technique. *J. Biomedical Materials Research-Part A* **2006**, 79A, (2), 418-430.
232. Mooney, D. J.; Mazzoni, C. L.; Breuer, C.; McNamara, K.; Hern, D.; Vacanti, J. P.; Langer, R., Stabilized polyglycolic acid fibre-based tubes for tissue engineering. *Biomaterials* **1996**, 17, (2), 115-124.
233. Douglas, T.; Haugen, H., Coating of polyurethane scaffolds with collagen: comparison of coating and cross-linking techniques. *Journal of Materials Science: Materials in Medicine*.
234. Spasova, M.; Paneva, D.; Manolova, N.; Radenkov, P.; Rashkov, I., Electrospun Chitosan-Coated Fibers of Poly(L-lactide) and Poly(L-lactide)/Poly(ethylene glycol): Preparation and Characterization. *Macromolecular Bioscience* **2008**, 8, (2), 153-162.
235. Greene, A.; Bumgardner, J.; Yang, Y.; Moseley, J.; Haggard, W., Chitosan-coated Stainless Steel Screws for Fixation in Contaminated Fractures. *Clinical Orthopaedics and Related Research*.
236. No, H. K.; Meyers, S. P.; Prinyawiwatukul, W.; Xu, Z., Applications of Chitosan for Improvement of Quality and Shelf Life of Foods: A Review. *Journal of Food Science* **2007**, 72, (5), R87-R100.
237. Chi-Hsiung Jou; Shang-Ming Lin; Ling Yun; Mou-Chuan Hwang; Da-Guang Yu; Wen-Li Chou; Jui-Sheng Lee; Yang, M.-C., Biofunctional properties of polyester fibers

- grafted with chitosan and collagen. *Polymers for Advanced Technologies* **2007**, 18, (3), 235-239.
238. van Hest, J. C. M., Biosynthetic-Synthetic Polymer Conjugates. *Polymer Reviews* **2007**, 47, (1), 63 - 92.
239. Huaping Tan; Lihong Lao; Jindan Wu; Yihong Gong; Gao, C., Biomimetic modification of chitosan with covalently grafted lactose and blended heparin for improvement of in vitro cellular interaction. *Polymers for Advanced Technologies* **2007**.
240. Martens, P. J.; Bryant, S. J.; Anseth, K. S., Tailoring the Degradation of Hydrogels Formed from Multivinyl Poly(ethylene glycol) and Poly(vinyl alcohol) Macromers for Cartilage Tissue Engineering. *Biomacromolecules* **2003**, 4, (2), 283-292.
241. Xipeng Guan; Daping Quan; Xintao Shuai; Kairong Liao; Mai, K., Chitosan-graft-poly(ϵ -caprolactone)s: An optimized chemical approach leading to a controllable structure and enhanced properties. *Journal of Polymer Science Part A: Polymer Chemistry* **2007**, 45, (12), 2556-2568.
242. Ying Wan; Xiaoying Cao; Quan Wu; Shengmin Zhang; Wang, S., Preparation and mechanical properties of poly(chitosan-g-DL-lactic acid) fibrous mesh scaffolds. *Polymers for Advanced Technologies* **2007**, 9999, (9999), n/a.
243. Hanna Bramfeldt; Pierre Sarazin; Vermette, P., Characterization, degradation, and mechanical strength of poly(D,L-lactide-co- ϵ -caprolactone)-poly(ethylene glycol)-poly(D,L-lactide-co- ϵ -caprolactone). *Journal of Biomedical Materials Research Part A* **2007**, 83A, (2), 503-511.
244. Kang, H.-M.; Cai, Y.-L.; Liu, P.-S., Synthesis, characterization and thermal sensitivity of chitosan-based graft copolymers. *Carbohydrate Research* **2006**, 341, (17), 2851-2857.
245. Bhattarai, N.; Ramay, H. R.; Gunn, J.; Matsen, F. A.; Zhang, M., PEG-grafted chitosan as an injectable thermosensitive hydrogel for sustained protein release. *Journal of Controlled Release* **2005**, 103, (3), 609-624.
246. Chen, J.-P.; Cheng, T.-H., Functionalized temperature-sensitive copolymer for tissue engineering of articular cartilage and meniscus. *Colloids and Surfaces A: Physicochemical and Engineering Aspects* In Press, Corrected Proof.
247. Toshihiko Senda; Yong He; Inoue, Y., Biodegradable blends of poly(ϵ -caprolactone) with chitin and chitosan: specific interactions, thermal properties and crystallization behavior. *Polymer International* **2002**, 51, (1), 33-39.
248. Sarasam, A.; Madhally, S. V., Characterization of chitosan-polycaprolactone blends for tissue engineering applications. *Biomaterials* **2005**, 26, (27), 5500-5508.
249. She, H.; Xiao, X.; Liu, R., Preparation and characterization of polycaprolactone-chitosan composites for tissue engineering applications. *Journal of Materials Science: Materials in Medicine* **2007**, 42, (19), 8113-8119.
250. Wang, Y.-C.; Lin, M.-C.; Wang, D.-M.; Hsieh, H.-J., Fabrication of a novel porous PGA-chitosan hybrid matrix for tissue engineering. *Biomaterials* **2003**, 24, (6), 1047-1057.
251. In Kyung Shim; Sang Young Lee; YoonJeong Park; Myung Chul Lee; Sang Hoon Lee; Jue Yeon Lee; Lee, S. J., Homogeneous chitosan-PLGA composite fibrous scaffolds for tissue regeneration. *Journal of Biomedical Materials Research Part A* **2007**, (online in advance of print).

252. Correlo, V. M.; Boesel, L. F.; Bhattacharya, M.; Mano, J. F.; Neves, N. M.; Reis, R. L., Properties of melt processed chitosan and aliphatic polyester blends. *Materials Science and Engineering: A* **2005**, 403, (1-2), 57-68.
253. Wan, Y.; Fang, Y.; Wu, H.; Cao, X., Porous polylactide/chitosan scaffolds for tissue engineering. *Journal of Biomedical Materials Research Part A* **2007**, 80A, (4), 776-789.
254. Chen, G.; Ushida, T.; Tateishi, T., A biodegradable hybrid sponge nested with collagen microsponges. *Journal of Biomedical Materials Research* **2000**, 51, (2), 273-279.
255. Gong, Y.; He, L.; Li, J.; Zhou, Q.; Ma, Z.; Gao, C.; Shen, J., Hydrogel-filled polylactide porous scaffolds for cartilage tissue engineering. *Journal of Biomedical Materials Research Part B: Applied Biomaterials* **2007**, 82B, (1), 192-204.
256. Shi, Y.; Ma, L.; Zhao, J.; Mao, Z.; Gao, C., Collagen/chitosan-silicone membrane bilayer scaffold as a dermal equivalent. *Polymers for advanced technologies* **2005**, 16, (11-12), 789-794.
257. Lawrence, B. J., Composite Scaffolds of Natural and Synthetic Polymers for Bladder Tissue Engineering. *MS Thesis* **2006**.
258. Tillman, J.; Ullm, A.; Madhally, S. V., Three-dimensional cell colonization in a sulfate rich environment. *Biomaterials* **2006**, 27, (32), 5618-26.
259. Nilsson, U.; Garvin, S.; Dabrosin, C., MMP-2 and MMP-9 activity is regulated by estradiol and tamoxifen in cultured human breast cancer cells. *Breast Cancer Research and Treatment* **2007**, 102, (3), 253-261(9).
260. Larson, E. M.; Doughman, D. J.; Gregerson, D. S.; Obritsch, W. F., A new, simple, nonradioactive, nontoxic in vitro assay to monitor corneal endothelial cell viability. *Invest. Ophthalmol. Vis. Sci.* **1997**, 38, (10), 1929-1933.
261. Kranz, H.; Ubrich, N.; Maincent, P.; Bodmeier, R., Physicomechanical properties of biodegradable poly(D,L-lactide) and poly(D,L-lactide-co-glycolide) films in the dry and wet states. *Journal of Pharmaceutical Sciences* **2000**, 89, (12), 1558-1566.
262. Aukunuru, J. V.; Ayalasomayajula, S. P.; Kompella, U. B., Nanoparticle formulation enhances the delivery and activity of a vascular endothelial growth factor antisense oligonucleotide in human retinal pigment epithelial cells. *J Pharm Pharmacol* **2003**, 55, (9), 1199-206.
263. Bhatia, S. N.; Balis, U. J.; Yarmush, M. L.; Toner, M., Effect of cell-cell interactions in preservation of cellular phenotype: cocultivation of hepatocytes and nonparenchymal cells. *Faseb J* **1999**, 13, (14), 1883-900.
264. Lazarous, D. F.; Unger, E. F.; Epstein, S. E.; Stine, A.; Arevalo, J. L.; Chew, E. Y.; Quyyumi, A. A., Basic fibroblast growth factor in patients with intermittent claudication: results of a phase I trial. *Journal of the American College of Cardiology* **2000**, 36, (4), 1239-1244.
265. Kawai, K.; Suzuki, S.; Tabata, Y.; Ikada, Y.; Nishimura, Y., Accelerated tissue regeneration through incorporation of basic fibroblast growth factor-impregnated gelatin microspheres into artificial dermis. *Biomaterials* **2000**, 21, (5), 489-499.
266. Putnam, D., Polymers for gene delivery across length scales. *Nat Mater* **2006**, 5, (6), 439-451.
267. Hamidi, M.; Zarrin, A.; Foroozesh, M., Novel Delivery Systems for Interferons. *Critical Reviews in Biotechnology* **2007**, 27, (3), 111 - 127.

268. Vasir, J. K.; Labhasetwar, V., Biodegradable nanoparticles for cytosolic delivery of therapeutics. *Advanced Drug Delivery Reviews* **2007**, 59, (8), 718-728.
269. Goldberg, M.; Langer, R.; Jia, X., Nanostructured materials for applications in drug delivery and tissue engineering. *Journal of Biomaterials Science, Polymer Edition* **2007**, 18, 241-268.
270. Silva, G. A.; Ducheyne, P.; Reis, R. L., Materials in particulate form for tissue engineering. 1. Basic concepts. *Journal of Tissue Engineering and Regenerative Medicine* **2007**, 1, (1), 4-24.
271. Kawashima, Y.; Yamamoto, H.; Takeuchi, H.; Hino, T.; Niwa, T., Properties of a peptide containing dl-lactide/glycolide copolymer nanospheres prepared by novel emulsion solvent diffusion methods. *European Journal of Pharmaceutics and Biopharmaceutics* **1998**, 45, (1), 41-48.
272. Sunkara, H. B.; Jethmalani, J. M.; Ford, W. T., Synthesis of crosslinked poly(styrene-co-sodium styrenesulfonate) latexes. *Journal of Polymer Science Part A: Polymer Chemistry* **1994**, 32, (8), 1431-1435.
273. Berkland, C.; Kim, K.; Pack, D. W., Fabrication of PLG microspheres with precisely controlled and monodisperse size distributions. *Journal of Controlled Release* **2001**, 73, (1), 59-74.
274. Vila, A.; Sanchez, A.; Tobio, M.; Calvo, P.; Alonso, M. J., Design of biodegradable particles for protein delivery. *J Control Release* **2002**, 78, (1-3), 15-24.
275. Qi, L.; Xu, Z.; Jiang, X.; Hu, C.; Zou, X., Preparation and antibacterial activity of chitosan nanoparticles. *Carbohydr Res* **2004**, 339, (16), 2693-700.
276. Cetin, M.; Aktas, Y.; Vural, I.; Capan, Y.; Dogan, L. A.; Duman, M.; Dalkara, T., Preparation and In Vitro Evaluation of bFGF-Loaded Chitosan Nanoparticles. *Drug Delivery* **2007**, 14, (8), 525 - 529.
277. Mondalek, F. G.; Lawrence, B. J.; Kropp, B. P.; Grady, B. P.; Fung, K.-M.; Madihally, S. V.; Lin, H.-K., The Incorporation of Poly (Lactic-co-glycolic) Acid Nanoparticles into Porcine Small Intestinal Submucosa Biomaterials. *Biomaterial* **2007**, (In Press).
278. Azarmi, S.; Huang, Y.; Chen, H.; McQuarrie, S.; Abrams, D.; Roa, W.; Finlay, W. H.; Miller, G. G.; Löbenberg, R., Optimization of a two-step desolvation method for preparing gelatin nanoparticles and cell uptake studies in 143B osteosarcoma cancer cells. *J Pharm Pharmaceut Sci* **2006**, 9, (1), 124-132.
279. Yi, F.; Wu, H.; Jia, G. L., Formulation and characterization of poly (D,L-lactide-co-glycolide) nanoparticle containing vascular endothelial growth factor for gene delivery. *Journal of Clinical Pharmacy and Therapeutics* **2006**, 31, (1), 43-48.
280. Shakweh, M.; Fattal, E., Design and characterisation of poly(lactide-co-glycolide) small particulate systems for the delivery of immunostimulant CpG oligonucleotide. *Journal of Nanoscience and Nanotechnology* **2006**, 6, (9-10), 2811-2820.
281. Hillaireau, H.; Le Doan, T.; Couvreur, P., Polymer-based nanoparticles for the delivery of nucleoside analogues. *Journal of Nanoscience and Nanotechnology* **2006**, 6, (9-10), 2608-2617.
282. Zweers, M. L. T.; Engbers, G. H. M.; Grijpma, D. W.; Feijen, J., Release of anti-restenosis drugs from poly(ethylene oxide)-poly (DL-lactic-co-glycolic acid) nanoparticles. *Journal of Controlled Release* **2006**, 114, (3), 317-324.

283. Musumeci, T.; Ventura, C. A.; Giannone, I.; Ruozzi, B.; Montenegro, L.; Pignatello, R.; Puglisi, G., PLA/PLGA nanoparticles for sustained release of docetaxel. *International Journal of Pharmaceutics* **2006**, 325, (1-2), 172-179.
284. Leo, E.; Scatturin, A.; Vighi, E.; Dalpiaz, A., Polymeric nanoparticles as drug controlled release systems: A new formulation strategy for drugs with small or large molecular weight. *Journal of Nanoscience and Nanotechnology* **2006**, 6, (9-10), 3070-3079.
285. Wendorf, J.; Singh, M.; Chesko, J.; Kazzaz, J.; Soewanan, E.; Ugozzoli, M.; O'Hagan, D., A practical approach to the use of nanoparticles for vaccine delivery. *Journal of Pharmaceutical Sciences* **2006**, 95, (12), 2738-2750.
286. Lamprecht, A.; Koenig, P.; Ubrich, N.; Maincent, P.; Neumann, D., Low molecular weight heparin nanoparticles: mucoadhesion and behaviour in Caco-2 cells. *Nanotechnology* **2006**, 17, (15), 3673-3680.
287. Farokhzad, O. C.; Cheng, J. J.; Teply, B. A.; Sherifi, I.; Jon, S.; Kantoff, P. W.; Richie, J. P.; Langer, R., Targeted nanoparticle-aptamer bioconjugates for cancer chemotherapy in vivo. *Proceedings of the National Academy of Sciences of the United States of America* **2006**, 103, (16), 6315-6320.
288. Tessmar, J. K.; Gopferich, A. M., Matrices and scaffolds for protein delivery in tissue engineering. *Advanced Drug Delivery Reviews* **2007**, 59, (4-5), 274-291.
289. Moioli, E. K.; Clark, P. A.; Xin, X.; Lal, S.; Mao, J. J., Matrices and scaffolds for drug delivery in dental, oral and craniofacial tissue engineering. *Advanced Drug Delivery Reviews* **2007**, 59, (4-5), 308-324.
290. Piyakulawat, P.; Praphairaksit, N.; Chantarasiri, N.; Muangsin, N., Preparation and evaluation of chitosan/carrageenan beads for controlled release of sodium diclofenac. *AAPS PharmSciTech* **2007**, 8, (4), 120-130.
291. Huang, G.; Gao, J.; Hu, Z.; St. John, J. V.; Ponder, B. C.; Moro, D., Controlled drug release from hydrogel nanoparticle networks. *Journal of Controlled Release* **2004**, 94, (2-3), 303-311.
292. Paasonen, L.; Laaksonen, T.; Johans, C.; Yliperttula, M.; Kontturi, K.; Urtti, A., Gold nanoparticles enable selective light-induced contents release from liposomes. *Journal of Controlled Release* **2007**, 122, (1), 86-93.
293. Quick, D. J.; Macdonald, K. K.; Anseth, K. S., Delivering DNA from photocrosslinked, surface eroding polyanhydrides. *Journal of Controlled Release* **2004**, 97, (2), 333-343.
294. Brunner, A.; Mäder, K.; Göpferich, A., pH and Osmotic Pressure Inside Biodegradable Microspheres During Erosion1. *Pharmaceutical Research* **1999**, 16, (6), 847-853.
295. Klose, D.; Siepmann, F.; Elkharraz, K.; Krenzlin, S.; Siepmann, J., How porosity and size affect the drug release mechanisms from PLGA-based microparticles. *International Journal of Pharmaceutics* **2006**, 314, (2), 198-206.
296. Kim, H.-W., Biomedical nanocomposites of hydroxyapatite/polycaprolactone obtained by surfactant mediation. *Journal of Biomedical Materials Research Part A* **2007**, 83A, (1), 169-177.
297. Abarrategi, A.; Gutierrez, M. C.; Moreno-Vicente, C.; Hortiguera, M. J.; Ramos, V.; Lopez-Lacomba, J. L.; Ferrer, M. L.; del Monte, F., Multiwall carbon nanotube scaffolds for tissue engineering purposes. *Biomaterials* **2008**, 29, (1), 94-102.

298. Montet, X.; Funovics, M.; Montet-Abou, K.; Weissleder, R.; Josephson, L., Multivalent Effects of RGD Peptides Obtained by Nanoparticle Display. *J. Med. Chem.* **2006**, 49, (20), 6087-6093.
299. Gupta, A. K.; Gupta, M., Synthesis and surface engineering of iron oxide nanoparticles for biomedical applications. *Biomaterials* **2005**, 26, (18), 3995-4021.
300. Ito, A.; Akiyama, H.; Kawabe, Y.; Kamihira, M., Magnetic force-based cell patterning using Arg-Gly-Asp (RGD) peptide-conjugated magnetite cationic liposomes. *Journal of Bioscience and Bioengineering* **2007**, 104, (4), 288-293.
301. Pissuwan, D.; Valenzuela, S. M.; Cortie, M. B., Therapeutic possibilities of plasmonically heated gold nanoparticles. *Trends in Biotechnology* **2006**, 24, (2), 62-67.
302. Kogan, M. J.; Bastus, N. G.; Amigo, R.; Grillo-Bosch, D.; Araya, E.; Turiel, A.; Labarta, A.; Giralt, E.; Puentes, V. F., Nanoparticle-Mediated Local and Remote Manipulation of Protein Aggregation. *Nano Lett.* **2006**, 6, (1), 110-115.
303. Letfullin, R. R.; Joenathan, C.; George, T. F.; Zharov, V. P., Laser-induced explosion of gold nanoparticles: potential role for nanophotothermolysis of cancer. *Nanomedicine* **2006**, 1, (4), 473-480.
304. Cedervall, T.; Lynch, I.; Lindman, S.; Berggard, T.; Thulin, E.; Nilsson, H.; Dawson, K. A.; Linse, S., From the Cover: Understanding the nanoparticle-protein corona using methods to quantify exchange rates and affinities of proteins for nanoparticles. *Proceedings of the National Academy of Sciences* **2007**, 104, (7), 2050-2055.
305. Ades, E. W.; Candal, F. J.; Swerlick, R. A.; George, V. G.; Summers, S.; Bosse, D. C.; Lawley, T. J., HMEC-1: Establishment of an immortalized human microvascular endothelial cell line. *Journal of Investigative Dermatology* **1992**, 99, (6), 683-690.
306. Astete, C. E.; Sabliov, C. M., Synthesis and characterization of PLGA nanoparticles. *Journal of Biomaterials Science-Polymer Edition* **2006**, 17, (3), 247-289.
307. Calvo, P.; Remuñán-López, C.; Vila-Jato, J. L.; Alonso, M. J., Novel hydrophilic chitosan-polyethylene oxide nanoparticles as protein carriers. *Journal of Applied Polymer Science* **1997**, 63, (1), 125-132.
308. Raghavan, D.; Kropp, B. P.; Lin, H. K.; Zhang, Y.; Cowan, R.; Madhally, S. V., Physical characteristics of small intestinal submucosa scaffolds are location-dependent. *J Biomed Mater Res A* **2005**, 73, (1), 90-6.
309. Cheng, E. Y.; Kropp, B. P., Urologic tissue engineering with small-intestinal submucosa: potential clinical applications. *World J Urol* **2000**, 18, (1), 26-30.
310. Kropp, B. P.; Cheng, E. Y.; Pope, J. C. t.; Brock, J. W., 3rd; Koyle, M. A.; Furness, P. D., 3rd; Weigel, N. D.; Keck, R. W.; Kropp, K. A., Use of small intestinal submucosa for corporal body grafting in cases of severe penile curvature. *J Urol* **2002**, 168, (4 Pt 2), 1742-5; discussion 1745.
311. Zhang, Y.; Kropp, B. P.; Lin, H. K.; Cowan, R.; Cheng, E. Y., Bladder regeneration with cell-seeded small intestinal submucosa. *Tissue Eng* **2004**, 10, (1-2), 181-7.
312. Colvert, J. R., 3rd; Kropp, B. P.; Cheng, E. Y.; Pope, J. C. t.; Brock, J. W., 3rd; Adams, M. C.; Austin, P.; Furness, P. D., 3rd; Koyle, M. A., The use of small intestinal submucosa as an off-the-shelf urethral sling material for pediatric urinary incontinence. *J Urol* **2002**, 168, (4 Pt 2), 1872-5; discussion 1875-6.

313. Martin, I.; Wendt, D.; Heberer, M., The role of bioreactors in tissue engineering. *Trends in Biotechnology* **2004**, 22, (2), 80-86.
314. Niklason, L. E.; Gao, J.; Abbott, W. M.; Hirschi, K. K.; Houser, S.; Marini, R.; Langer, R., Functional Arteries Grown in Vitro. *Science* **1999**, 284, (5413), 489-493.
315. Heydarkhan-Hagvall, S.; Esguerra, M.; Helenius, G.; Sapperberg, R.; Johansson, B. R.; Risberg, B., Production of Extracellular Matrix Components in Tissue-Engineered Blood Vessels. *Tissue Engineering* **2006**, 12, (4), 831-842.
316. Gooch, K. J.; Kwon, J. H.; Blunk, T.; Langer, R.; Freed, L.; Vunjak-Novakovic, E. G., Effects of mixing intensity on tissue-engineered cartilage. *Biotechnology and Bioengineering* **2001**, 72, (4), 402-407.
317. Stephens, J. S.; Cooper, J. A.; Phelan, F. R., Jr.; Dunkers, J. P., Perfusion flow bioreactor for 3D in situ imaging: investigating cell/biomaterials interactions. *Biotechnol Bioeng* **2007**, 97, (4), 952-61.
318. Lawrence, B. J.; Devarapalli, M.; Madhally, S. V., Flow Dynamics in Bioreactors Containing Tissue Engineering Scaffolds. *Biotechnology and Bioengineering* **2008**, Accepted Pending Revision.
319. Billiar, K. L.; Sacks, M. S., Biaxial mechanical properties of the native and glutaraldehyde-treated aortic valve cusp: Part II--A structural constitutive model. *J Biomech Eng* **2000**, 122, (4), 327-35.
320. Martin, Y.; Vermette, P., Bioreactors for tissue mass culture: Design, characterization, and recent advances. *Biomaterials* **2005**, 26, (35), 7481-7503.
321. Sucosky, P.; Osorio, D. F.; Brown, J. B.; Neitzel, G. P., Fluid mechanics of a spinner-flask bioreactor. *Biotechnology and Bioengineering* **2004**, 85, (1), 34-46.
322. Bilgen, B.; Barabino, G. A., Location of scaffolds in bioreactors modulates the hydrodynamic environment experienced by engineered tissues. *Biotechnology and Bioengineering* **2007**, 98, (1), 282-294.
323. Bilgen, B.; Sucosky, P.; Neitzel, G. P.; Barabino, G. A., Flow characterization of a wavy-walled bioreactor for cartilage tissue engineering. *Biotechnology and Bioengineering* **2006**, 95, (6), 1009-1022.
324. Walther, I., Space bioreactors and their applications. *Advances in space biology and medicine* **2002**, 8, 197-213.
325. Williams, K. A.; Saini, S.; Wick, T. M., Computational Fluid Dynamics Modeling of Steady-State Momentum and Mass Transport in a Bioreactor for Cartilage Tissue Engineering. *Biotechnol. Prog.* **2002**, 18, (5), 951-963.
326. Chung, C. A.; Chen, C. W.; Chen, C. P.; Tseng, C. S., Enhancement of cell growth in tissue-engineering constructs under direct perfusion: Modeling and simulation. *Biotechnology and Bioengineering* **2007**, 97, (6), 1603-1616.
327. Williams, C.; Wick, T. M., Endothelial Cell-Smooth Muscle Cell Co-Culture in a Perfusion Bioreactor System. *Annals of Biomedical Engineering* **2005**, 33, (7), 920-928.
328. Kitagawa, T.; Yamaoka, T.; Iwase, R.; Murakami, A., Three-dimensional cell seeding and growth in radial-flow perfusion bioreactor for in vitro tissue reconstruction. *Biotechnology and Bioengineering* **2006**, 93, (5), 947-954.
329. Singh, H.; Ang, E. S.; Lim, T. T.; Huttmacher, D. W., Flow modeling in a novel non-perfusion conical bioreactor. *Biotechnology and Bioengineering* **2007**, 97, (5), 1291-1299.

330. Hutmacher, D. W.; Singh, H., Computational fluid dynamics for improved bioreactor design and 3D culture. *Trends Biotechnol* **2008**, 26, (4), 166-72.
331. Brown, A.; Meenan, B. J., Investigating the effects of fluid shear forces on cellular responses to profiled surfaces in-vitro: a computational and experimental investigation. *Conf Proc IEEE Eng Med Biol Soc* **2007**, 2007, 5387-90.
332. Cioffi, M.; Boschetti, F.; Raimondi, M. T.; Dubini, G., Modeling evaluation of the fluid-dynamic microenvironment in tissue-engineered constructs: A micro-CT based model. *Biotechnology and Bioengineering* **2006**, 93, (3), 500-510.
333. Porter, B.; Zauel, R.; Stockman, H.; Guldberg, R.; Fyhrie, D., 3-D computational modeling of media flow through scaffolds in a perfusion bioreactor. *Journal of Biomechanics* **2005**, 38, (3), 543-549.
334. Sander, E. A.; Nauman, E. A., Permeability of musculoskeletal tissues and scaffolding materials: experimental results and theoretical predictions. *Critical Reviews in Biomedical Engineering* **2003**, 31, (1), 1-26.
335. Bilgen, B.; Barabino, G. A., Location of scaffolds in bioreactors modulates the hydrodynamic environment experienced by engineered tissues. *Biotechnol Bioeng* **2007**, 98, (1), 282-94.
336. Timmins, N. E.; Scherberich, A.; Fruh, J.-A.; Heberer, M.; Martin, I.; Jakob, M., Three-Dimensional Cell Culture and Tissue Engineering in a T-CUP (Tissue Culture Under Perfusion). *Tissue Engineering* **2007**, 13, (8), 2021-2028.
337. Boschetti, F.; Raimondi, M. T.; Migliavacca, F.; Dubini, G., Prediction of the micro-fluid dynamic environment imposed to three-dimensional engineered cell systems in bioreactors. *Journal of Biomechanics* **2006**, 39, (3), 418-425.
338. Chung, C. A.; Chen, C. W.; Chen, C. P.; Tseng, C. S., Enhancement of cell growth in tissue-engineering constructs under direct perfusion: Modeling and simulation. *Biotechnol Bioeng* **2007**, 97, (6), 1603-16.
339. Capuani, F.; Frenkel, D.; Lowe, C. P., Velocity fluctuations and dispersion in a simple porous medium. *Phys Rev E Stat Nonlin Soft Matter Phys* **2003**, 67, (5 Pt 2), 056306.
340. Fogler, H. S., *Elements of Chemical Reactor Engineering*. 4th ed.; Prentice Hall: Upper Saddle River, NJ, 2006.
341. Lawrence, B.; Beene, J.; Madhally, S.; Lewis, R., Incorporating Nonideal Reactors in a Junior-Level Course using Computational Fluid Dynamics (CFD). *Chemical Engineering Education* **2004**, 38, (2), 136-141.
342. Macario, D. K.; Entersz, I.; Paul Abboud, J.; Nackman, G. B., Inhibition of Apoptosis Prevents Shear-Induced Detachment of Endothelial Cells. *J Surg Res* **2007**.
343. Tilles, A. W.; Baskaran, H.; Roy, P.; Yarmush, M. L.; Toner, M., Effects of oxygenation and flow on the viability and function of rat hepatocytes cocultured in a microchannel flat-plate bioreactor. *Biotechnol Bioeng* **2001**, 73, (5), 379-89.
344. Truskey, G. A.; Yuan, F.; Katz, D. F., Transport Phenomena in Biological Systems. In Pearson Prentice Hall: Upper Saddle River, NJ, 2004; pp 317-321.
345. Koller, M. R.; Emerson, S. G.; Palsson, B. O., Large-scale expansion of human stem and progenitor cells from bone marrow mononuclear cells in continuous perfusion cultures. *Blood* **1993**, 82, (2), 378-84.

346. Kim, S. S.; Sundback, C. A.; Kaihara, S.; Benvenuto, M. S.; Kim, B. S.; Mooney, D. J.; Vacanti, J. P., Dynamic seeding and in vitro culture of hepatocytes in a flow perfusion system. *Tissue Eng* **2000**, 6, (1), 39-44.
347. Shito, M.; Kim, N. H.; Baskaran, H.; Tilles, A. W.; Tompkins, R. G.; Yarmush, M. L.; Toner, M., In vitro and in vivo evaluation of albumin synthesis rate of porcine hepatocytes in a flat-plate bioreactor. *Artif Organs* **2001**, 25, (7), 571-8.
348. Marolt, D.; Augst, A.; Freed, L. E.; Vepari, C.; Fajardo, R.; Patel, N.; Gray, M.; Farley, M.; Kaplan, D.; Vunjak-Novakovic, G., Bone and cartilage tissue constructs grown using human bone marrow stromal cells, silk scaffolds and rotating bioreactors. *Biomaterials* **2006**, 27, (36), 6138-49.
349. Sodian, R.; Hoerstrup, S. P.; Sperling, J. S.; Daebritz, S. H.; Martin, D. P.; Schoen, F. J.; Vacanti, J. P.; Mayer, J. E., Tissue engineering of heart valves: in vitro experiences. *The Annals of Thoracic Surgery* **2000**, 70, (1), 140-144.
350. Gutierrez, R. A.; Crumpler, E. T., Potential effect of geometry on wall shear stress distribution across scaffold surfaces. *Ann Biomed Eng* **2008**, 36, (1), 77-85.
351. Kim, B. S.; Nikolovski, J.; Bonadio, J.; Mooney, D. J., Cyclic mechanical strain regulates the development of engineered smooth muscle tissue. *Nat Biotechnol* **1999**, 17, (10), 979-83.
352. Altman, G. H.; Lu, H. H.; Horan, R. L.; Calabro, T.; Ryder, D.; Kaplan, D. L.; Stark, P.; Martin, I.; Richmond, J. C.; Vunjak-Novakovic, G., Advanced Bioreactor with Controlled Application of Multi-Dimensional Strain For Tissue Engineering. *Journal of Biomechanical Engineering* **2002**, 124, (6), 742-749.
353. Arrigoni, C.; Chitto, A.; Mantero, S.; Remuzzi, A., Rotating versus perfusion bioreactor for the culture of engineered vascular constructs based on hyaluronic acid. *Biotechnol Bioeng* **2008**.
354. Wheeler, M. L.; Pi-Sunyer, F. X., Carbohydrate Issues: Type and Amount. *Journal of the American Dietetic Association* **2008**, 108, (4, Supplement 1), S34-S39.
355. Mehta, G.; Mehta, K.; Sud, D.; Song, J.; Bersano-Begey, T.; Futai, N.; Heo, Y. S.; Mycek, M.-A.; Linderman, J.; Takayama, S., Quantitative measurement and control of oxygen levels in microfluidic poly(dimethylsiloxane) bioreactors during cell culture. *Biomedical Microdevices* **2007**, 9, (2), 123-134.
356. Gao, F. G.; Fay, J. M.; Mathew, G.; Jeevarajan, A. S.; Anderson, M. M., Optical sensor based on fluorescent quenching and pulsed blue LED excitation for long-term monitoring of dissolved oxygen in NASA space bioreactors. *Journal of Biomedical Optics* **2005**, 10, (5), 054005-6.
357. Pouvreau, L. A. M.; Strampraad, M. J. F.; Berloo, S. V.; Kattenberg, J. H.; de Vries, S.; Robert, K. P., NO, N₂O, and O₂ Reaction Kinetics: Scope and Limitations of the Clark Electrode. In *Methods in Enzymology*, Academic Press: 2008; Vol. Volume 436, pp 97-112.
358. Theegala, C. S.; Small, D. D.; Monroe, W. T., Oxygen electrode-based single antibody amperometric biosensor for qualitative detection of E. coli and bacteria in water. *Journal of Environmental Science and Health, Part A* **2008**, 43, (5), 478 - 487.
359. Kelly, W. J., Using computational fluid dynamics to characterize and improve bioreactor performance. *Biotechnology and Applied Biochemistry* **2008**, 049, (4), 225-238.

360. Brown, A.; Meenan, B. J. In *Investigating the Effects of Fluid Shear Forces on Cellular Responses to Profiled Surfaces in-Vitro: A Computational and Experimental Investigation*, Engineering in Medicine and Biology Society, 2007. EMBS 2007. 29th Annual International Conference of the IEEE, 2007; 2007; pp 5387-5390.
361. Pierre, J.; Oddou, C., Engineered bone culture in a perfusion bioreactor: a 2D computational study of stationary mass and momentum transport. *Computer Methods in Biomechanics and Biomedical Engineering* **2007**, 10, (6), 429 - 438.
362. Kwon, O.; Devarakonda, S. B.; Sankovic, J. M.; Banerjee, R. K., Oxygen transport and consumption by suspended cells in microgravity: A multiphase analysis. *Biotechnology and Bioengineering* **2008**, 99, (1), 99-107.
363. Cheng, G.; Youssef, B. B.; Markenscoff, P.; Zygourakis, K., Cell Population Dynamics Modulate the Rates of Tissue Growth Processes. *Biophys. J.* **2006**, 90, (3), 713-724.
364. Galbusera, F.; Cioffi, M.; Raimondi, M. T.; Pietrabissa, R., Computational modeling of combined cell population dynamics and oxygen transport in engineered tissue subject to interstitial perfusion. *Computer Methods in Biomechanics and Biomedical Engineering* **2007**, 10, (4), 279 - 287.
365. Sengers, B. G.; Heywood, H. K.; Lee, D. A.; Oomens, C. W. J.; Bader, D. L., Nutrient Utilization by Bovine Articular Chondrocytes: A Combined Experimental and Theoretical Approach. *Journal of Biomechanical Engineering* **2005**, 127, (5), 758-766.
366. Motterlini, R.; Kerger, H.; Green, C. J.; Winslow, R. M.; Intaglietta, M., Depression of endothelial and smooth muscle cell oxygen consumption by endotoxin. *Am J Physiol Heart Circ Physiol* **1998**, 275, (3), H776-782.
367. Alpert, E.; Gruzman, A.; Totary, H.; Kaiser, N.; Reich, R.; Sasson, S., A natural protective mechanism against hyperglycaemia in vascular endothelial and smooth-muscle cells: role of glucose and 12-hydroxyeicosatetraenoic acid. *Biochem. J.* **2002**, 362, (2), 413-422.
368. Ocean Optics Inc Fiber Optic Oxygen Sensors: Theory of Operation, <http://www.oceanoptics.com/products/sensorththeory.asp>, accessed June 4, 2008. <http://www.oceanoptics.com/products/sensorththeory.asp> (June 4),
369. Estey, R. S., *The Use of the AO Spencer Spectrometer*. American Optical Company, Instrument Division: Buffalo, NY, 1938.

VITA

Benjamin J. Lawrence

Candidate for the Degree of

Doctor of Philosophy

Thesis: MASS TRANSFER IN POROUS TISSUE ENGINEERING SCAFFOLDS

Major Field: Chemical Engineering

Biographical:

Personal Data:

Born on March 16, 1980 in Tulsa OK. Son of Larry and Sharon Lawrence.

Education:

Graduated from Union High School, Tulsa OK in May 1999. Obtained a Bachelor of Science in Chemical Engineering at Oklahoma State University, Stillwater, Oklahoma in July, 2008. Obtained a Master of Science in Chemical Engineering at Oklahoma State University, Stillwater, Oklahoma in July, 2008. Completed the requirements for the Doctor of Philosophy in Chemical Engineering at Oklahoma State University, Stillwater, Oklahoma in July, 2008.

Experience:

Employed as a summer research assistant at the University of Colorado, Boulder as part of the National Science Foundation Research Experience for Undergraduates program in 2003. Participated in undergraduate research at Oklahoma State University 2002 – 2004, and has been employed as a Graduate Research Assistant for Oklahoma State University since 2005.

Professional Memberships: American Institute of Chemical Engineers,
American Society of Engineering Education

Name: Benjamin J Lawrence

Date of Degree: July 2008

Institution: Oklahoma State University

Location: Stillwater, Oklahoma

Title of Study: MASS TRANSFER IN POROUS TISSUE ENGINEERING
SCAFFOLDS

Pages in Study: 182

Candidate for the Degree of Doctor of Philosophy

Major Field: Chemical Engineering

Scope and Method of Study: This study evaluated the effects of both local and global scale mass transport phenomena through degradable porous polymer matrices typically used in tissue engineering. Analytical, computational and experimental methods were used to explore changes in matrix permeability as well as flow distribution, pressure drop, shear stress, and nutrient consumption when maturing matrices *in vitro*.

Findings and Conclusions: Nanoparticles fabricated from a variety of materials (Latex, PLGA, PLGA-HA, and chitosan) were successfully integrated into the porous matrices. Additionally, it was found that the permeability of the porous matrix could be modified based on both the size and number of embedded particles. The flow dynamics in bioreactor systems containing porous polymer matrices were also evaluated. The residence time distribution for reactors with and without porous structures was evaluated computationally and validated experimentally. The shear stress and pressure drop profiles for the reactors were simulated to explore the effect of changes within the porous structure. Finally, the effects of cellular respiration were added into the simulation and attempts were made to visualize the oxygen profile experimentally. These results provide insight into the inner working of tissue regeneration and should lead to both improved scaffold designs and better clinical outcomes.

ADVISER'S APPROVAL: Dr. Sundar Madihally
